University of Potsdam, Faculty of Science

Leibniz Institute for Astrophysics Potsdam (AIP)

Dissertation

Propagation of Energetic Electrons in the Solar Corona Observed with LOFAR

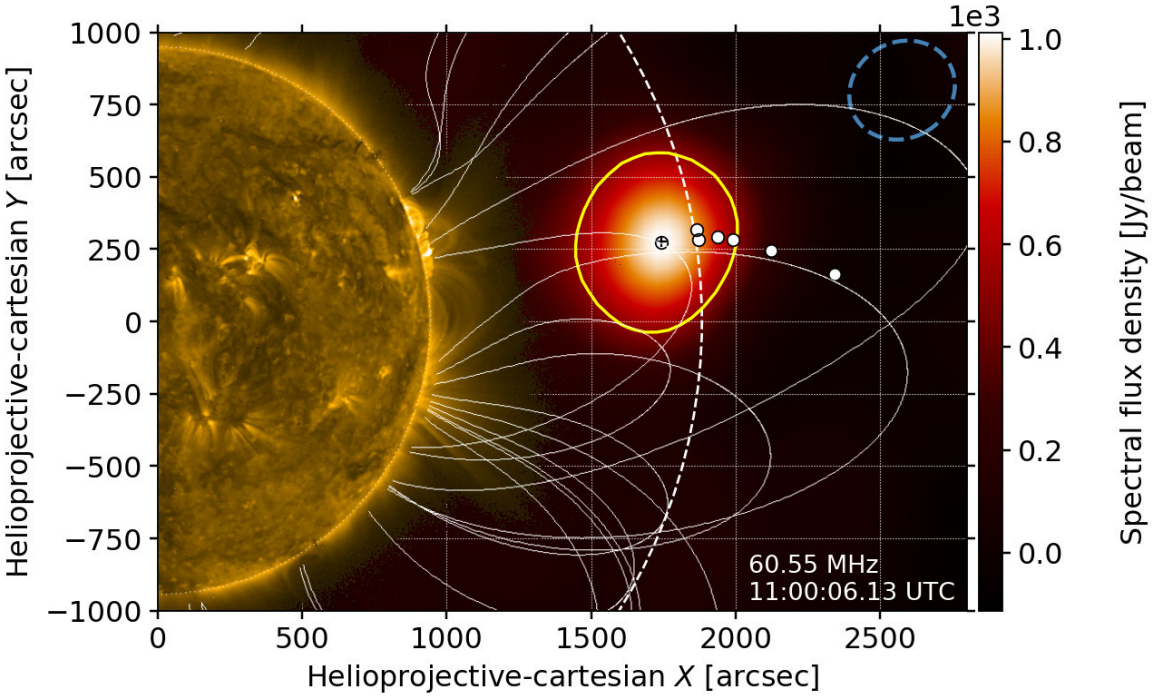

Frank Breitling

orcid.org/0000-0002-0904-8022

Cover figure: LOFAR image of a solar type III radio burst on June 23, 2012 at 60.55 MHz, solar magnetic field lines and the extreme ultraviolet (174 Å) image from the SWAP instrument (Halain et al., 2013) of the PROBA2 satellite. The white dots indicate the propagation path of the radio source as observed at different radio frequencies. Further information is given in Chapter 6.

Leibniz-Institut für Astrophysik Potsdam

Solar Radio Physics

Propagation of Energetic Electrons in the Solar Corona Observed with LOFAR

Dissertation
zur Erlangung des akademischen Grades
"doktor rerum naturalium"
(Dr. rer. nat.)
in der Wissenschaftsdisziplin Astrophysik

eingereicht an der
Mathematisch-Naturwissenschaftlichen Fakultät
der Universität Potsdam

von

Frank Breitling

Potsdam, den 9. Juni 2017

Published online at the
Institutional Repository of the University of Potsdam:
URN urn:nbn:de:kobv:517-opus4-396893
http://nbn-resolving.de/urn:nbn:de:kobv:517-opus4-396893

To my parents, who — besides me — likely have anticipated the completion of this work the most.

Abstract

This work reports about new high-resolution imaging and spectroscopic observations of solar type III radio bursts at low radio frequencies in the range from 30 to 80 MHz. Solar type III radio bursts are understood as result of the beam-plasma interaction of electron beams in the corona. The Sun provides a unique opportunity to study these plasma processes of an active star. Its activity appears in eruptive events like flares, coronal mass ejections and radio bursts which are all accompanied by enhanced radio emission. Therefore solar radio emission carries important information about plasma processes associated with the Sun's activity. Moreover, the Sun's atmosphere is a unique plasma laboratory with plasma processes under conditions not found in terrestrial laboratories. Because of the Sun's proximity to Earth, it can be studied in greater detail than any other star but new knowledge about the Sun can be transfer to them. This "solar stellar connection" is important for the understanding of processes on other stars.

The novel radio interferometer LOFAR provides imaging and spectroscopic capabilities to study these processes at low frequencies. Here it was used for solar observations.

LOFAR, the characteristics of its solar data and the processing and analysis of the latter with the Solar Imaging Pipeline and Solar Data Center are described. The Solar Imaging Pipeline is the central software that allows using LOFAR for solar observations. So its development was necessary for the analysis of solar LOFAR data and realized here. Moreover a new density model with heat conduction and Alfvén waves was developed that provides the distance of radio bursts to the Sun from dynamic radio spectra.

Its application to the dynamic spectrum of a type III burst observed on March 16, 2016 by LOFAR shows a nonuniform radial propagation velocity of the radio emission. The analysis of an imaging observation of type III bursts on June 23, 2012 resolves a burst as bright, compact region localized in the corona propagating in radial direction along magnetic field lines with an average velocity of $0.23c$. A nonuniform propagation velocity is revealed. A new beam model is presented that explains the nonuniform motion of the radio source as a propagation effect of an electron ensemble with a spread velocity distribution and rules out a monoenergetic electron distribution. The coronal electron number density is derived in the region from 1.5 to 2.5 $R_\odot$ and fitted with the newly developed density model. It determines the plasma density for the interplanetary space between Sun and Earth. The values correspond to a 1.25- and 5-fold Newkirk model for harmonic and fundamental emission, respectively. In comparison to data from other radio instruments the LOFAR data shows a high sensitivity and resolution in space, time and frequency.

The new results from LOFAR's high resolution imaging spectroscopy are consistent with current theories of solar type III radio bursts and demonstrate its capability to track fast moving radio sources in the corona. LOFAR solar data is found to be a valuable source for solar radio physics and opens a new window for studying plasma processes associated with highly energetic electrons in the solar corona.

Zusammenfassung

Diese Arbeit befasst sich mit neuen hochaufgelösten abbildenden und spektroskopischen Beobachtungen von solaren Typ III Radiobursts bei niedrigen Frequenzen im Bereich von 30 bis 80 MHz. Solare Typ III Radiobursts werden auf die Beam-Plasmawechselwirkung von Elektronenstrahlen in der Korona zurückgeführt. Die Sonne stellt eine einzigartige Möglichkeit dar, diese Plasmaprozesse eines aktiven Sterns zu untersuchen. Die Aktivität zeigt sich in eruptiven Ereignissen wie Flares, koronalen Massenauswürfen und Radiobursts, die jeweils von erhöhter Radiostrahlung begleitet werden. Daher trägt solare Radioemission wichtige Informationen über Plasmaprozesse, die mit Sonnenaktivität in Verbindung stehen. Darüber hinaus ist die Sonne auch ein einzigartiges Plasmalabor mit Plasmaprozessen unter Bedingungen die man nicht in irdischen Laboren findet. Aufgrund ihres vergleichsweise geringen Abstands kann man die Sonne wesentlich genauer beobachten als andere Sterne, aber neue Erkenntnisse von ihr auf andere Sterne übertragen. Diese "Solare-Stellare Verbindung" ist wichtig um Prozesse auf anderen Sternen zu verstehen.

Das neue Radiointerferometer LOFAR bietet abbildende und spektroskopische Möglichkeiten, um diese Prozesse bei niedrigen Frequenzen zu untersuchen und wurde hier für Sonnenbeobachtungen genutzt.

LOFAR, die Besonderheiten seiner Sonnendaten sowie das Verarbeiten und Analysieren dieser Daten mit der Solar Imaging Pipeline und dem Solar Data Center werden beschrieben. Die Solar Imaging Pipeline ist die zentrale Software, die die Nutzung von LOFAR für Sonnenbeobachtungen ermöglicht. Daher war deren Entwicklung für die Analyse von Sonnendaten notwendig und ist im Rahmen dieser Arbeit erfolgt. Außerdem wurde ein neues Dichtemodell mit Wärmeleitung und Alfvén-Wellen entwickelt, welches die Bestimmung der Entfernung von Radiobursts zur Sonne mittels dynamischer Spektren ermöglicht.

Die Anwendung auf dynamische Spektren eines LOFAR Typ III Bursts am 16. März 2016 zeigt eine radiale, ungleichförmige Ausbreitungsgeschwindigkeit der Radioemission. Die Analyse einer abbildenden Beobachtung von Typ III Bursts am 23. Juni 2012 zeigt den Burst als helle, kompakte Region in der Korona die sich in radiale Richtung entlang magnetischer Feldlinien mit einer durchschnittlichen Geschwindigkeit von $0.23c$ (c, Lichtgeschwindigkeit) bewegt. Die Geschwindigkeit ist nicht gleichförmig. Ein neues Beammodell wird vorgestellt, dass diese ungleichförmige Geschwindigkeit als Ausbreitungseffekt eines Elektronenensemble mit einer ausgedehnten Geschwindigkeitsverteilung erklärt und eine monoenergetische Elektronenverteilung ausschließt. Die koronale Elektronenzahldichte wird in der Region von 1.5 bis 2.5 $R_\odot$ ermittelt und ein Fit mit dem neuen Dichtemodell durchgeführt. Dadurch ist die Plasmadichte im ganzen interplanetaren Raum zwischen Sonne und Erde bestimmt. Die Werte entsprechen jeweils einem 1.25- und 5-fachen Newkirk Modell im Fall von fundamentaler und harmonischer Emission. Im Vergleich zu Daten von anderen Radioinstrumenten haben LOFAR-Daten eine hohe Empfindlichkeit und Auflösung in Raum, Zeit und Frequenz.

Die neuen Ergebnisse von LOFARs hochauflösender, abbildender Spektroskopie stimmen mit derzeitigen Theorien von solaren Typ III Radiobursts überein und zeigen die Möglichkeit, schnell bewegliche Radioquellen in der Korona zu verfolgen. LOFAR Sonnendaten wurden als wertvolle Quelle für solare Radiophysik erkannt und öffnen eine neues Fenster zur Untersuchung von Plasmaprozessen hochenergetischer Elektronen in der Korona.

Contents

List of Figures

List of Tables

Chapter

1

Introduction

The Sun is clearly the closest star to Earth. With a distance of one astronomical unit ($1\,\mathrm{AU} = 1.4960 \times 10^8\,\mathrm{km}$) it is approximately 270,000 times closer than the next closest star Proxima Centauri. This proximity of the Sun provides a unique opportunity to study a star in detail and to learn about other stars from observations of the Sun. The Sun is also a vast plasma environment that shows different plasma phenomena at different conditions as it extends from the very dense and hot solar interior to the very thin and much colder solar wind in interplanetary space. It also generates space weather through solar flares and coronal mass ejections (CMEs) which can disturb communication or GPS signals and even harm technical equipment on Earth and in space. Therefore an understanding of these phenomena is also of practical importance to minimize disturbances. Unfortunately the understanding of the Sun and its phenomena is still incomplete and open questions remain.

Some of these questions regard solar radio bursts and their associated plasma processes in the corona. Solar radio bursts are bright localized transient radio sources in the corona which often appear during times of an increased solar activity. They can exceed the flux density of the quiet Sun by orders of magnitude and so appear as the brightest radio sources in the sky. Since some radio bursts have no counterpart at other wavelengths, radio observations are crucial for their full exploration. Although significant progress has been made since their discovery solar radio bursts are still an active field of research. They are classified in five different types (Wild and McCready, 1950; Boischot, 1957; Wild, Sheridan, and Trent, 1959). This work will focus on solar radio burst of type III. Solar type III burst are associated with beams of electrons propagating through the corona, sometimes over long distances far into interplanetary space and even beyond Earth. Apart from the acceleration mechanism of the electrons, current research addresses the interaction of the beam with the coronal plasma and the resulting emission mechanism of electromagnetic radiation. While plasma emission via Langmuir waves is generally accepted as the main production mechanism for the observed fundamental and harmonic radio emission it is still an ongoing effort to explain the observations with proper models and simulations. Therefore high quality data is necessary to aid the model development and permit their comparison with observations as discussed for example by (Reid and Ratcliffe, 2014).

The Low Frequency Array (LOFAR, van Haarlem et al., 2013) is presently the most advanced radio interferometer for the low frequency range from 10–90 and 110–250 MHz and is capable of high resolution dynamic imaging spectroscopy of the Sun. This means that LOFAR observations can image and resolve the propagation of solar type III bursts through the corona with a time resolution of less than a second at multiple frequencies simultaneously. In addition it can provide dynamic radio spectra at significantly higher time resolution. These capabilities make LOFAR a unique instrument for studying solar type III bursts. It can provide new observations with a resolution, sensitivity and frequency coverage that could not be achieved in previous type III burst observation for instance by the interferometers at Culgoora (Wild, 1970), Nançay (Bougeret et al., 1970) and Clark Lake (Kundu et al., 1983).

Here, new dynamic spectra and images of LOFAR solar type III burst observations are analyzed and their interpretations are discussed. Chapter 2 and 3 give an introduction to the Sun and to solar radio bursts. Chapter 4 describes the LOFAR interferometer as well as the Solar Imaging Pipeline and the Solar Data Center which were developed by the author during the doctoral work in order to obtain the first interferometric images of the Sun. The Solar Imaging Pipeline was an essential development and without it, solar imaging with LOFAR and the results presented here would not have been achieved. Many details described in this chapter have also been published in articles (see below) with significant contribution by the author of this thesis. This chapter provides the latest update.

> G. Mann, C. Vocks, and F. Breitling (2011). "Solar Observations with LOFAR". in: *Planetary, Solar and Heliospheric Radio Emissions (PRE VII)*, pp. 507–512. Bibcode: 2011pre7.conf..507M
>
> M. P. van Haarlem, ..., F. Breitling, ... et al. (2013). "LOFAR: The LOw-Frequency ARray". In: A&A 556, A2, A2. arXiv: 1305.3550 [astro-ph.IM][1]
>
> F. Breitling et al. (2015). "The LOFAR Solar Imaging Pipeline and the LOFAR Solar Data Center". In: *Astronomy and Computing* 13, pp. 99–107. DOI: 10.1016/j.ascom.2015.08.001. arXiv: 1603.05990 [astro-ph.IM]. Bibcode: 2015A%26C....13...99B[1]

Chapter 5 discusses the LOFAR dynamic radio spectrum of a solar type III burst propagating into interplanetary space and its interpretation based on density models. A new density model was developed for this purpose. It includes important physics of the coronal plasma and the solar wind such as heat conduction and Alfvén waves and is consistent with parameters observed at the Sun and near Earth. This new model was already presented earlier (see below), but more details regarding the solution of the system of differential equations are given here.

> F. Breitling, G. Mann, and C. Vocks (2011). "Propagation of Energetic Electrons from the Corona into Interplanetary Space and Type III Radio Emission". In: *Planetary, Solar and Heliospheric Radio Emissions (PRE VII)*, pp. 373–380. arXiv: 1511.03123 [astro-ph.SR]. Bibcode: 2011pre7.conf..373B[1]

[1]Online at http://arxiv.org/abs/ + arXiv

Chapter 6 presents the first interferometric LOFAR images of a Type III burst and discusses the various information that can be derived from them. These information include the propagation of electron beam and the density of the coronal plasma. The results of this chapter have also been summarized in an article which has been submitted to A&A for publication (currently under minor revision).

> G. Mann, F. Breitling et al. "Tracking of an electron beam through the solar corona with LOFAR". Submitted to A&A

The scientific results presented in Chapter 5 and 6 were only possible through the availability of the Solar Imaging Pipeline (Chapter 4). About 40 other LOFAR publications with 1000 citations have appeared in refereed journals by the author as part of the LOFAR builders list and the Solar Key Science Project. However, since they are not directly related to the doctoral project they are not listed. The following publication of the first LOFAR images of the Sun is related, because it used the Solar Imaging Pipeline for LOFAR data of a type I burst.

> C. Vocks, G. Mann, and F. Breitling (2016). "Self-calibration strategy for a LOFAR solar radio burst observation". In: *Astronomische Nachrichten* 337, pp. 1099–1104. DOI: 10.1002/asna.201612443

Chapter

2

The Sun

The Sun is an active star. As such it exhibits a variety of phenomena in addition to those related to the quiet Sun like thermal radiation and the solar wind. They range from sunspots to flares and coronal mass ejections (CMEs) with far reaching effects on interplanetary space and space weather. Increased radio emission and radio bursts are another example of its activity which are often observed with eruptive events such as flares and CMEs. The Sun's activity varies with an 11-year cycle in which the number of active regions closely related to the number of sunspots increases and decreases periodically. Its activity is caused by the solar dynamo process which is generated through the Sun's differential rotation. Many details about the Sun are already known and can explain many of its phenomena. Good introductions are Priest (1982) and Aschwanden (2004) where the many details and numbers of this chapter can be found.

2.1 Overall Properties

The Sun's basic properties are known from observations (Table 2.1). It is a star of spectral type G2V. G2 means that it is a G-type stars of hotness two. G-type stars have prominent H and K lines of Calcium and a yellow appearance. V denotes the luminosity class. V is a class of main-sequence stars. The Sun is brighter than 85% of the stars in our Galaxy.

Parameter	Value
Spectral classification	G2V
Radius ($R_\odot$)	$695,700\,\mathrm{km}$
Distance from Earth	$0.983 - 1.017\,\mathrm{AU}$
Angular size	$31.6 - 32.7\,\mathrm{arcmin}$
Mass ($M_\odot$)	$1.99 \times 10^{30}\,\mathrm{kg}$
Mass loss rate	$\sim 10^9\,\mathrm{kg/s}$
Radiance ($I_\odot$)	$2.01 \times 10^7\,\mathrm{W/m^2/sr}$
Equatorial rotation period	$26\,\mathrm{d}$
Age	$4.6 \times 10^9\,\mathrm{a}$

Table 2.1: Basic parameters of the Sun mainly according to Mamajek et al. (2015) and Zombeck (1990). The mean distance form Earth is defined as astronomical unit ($1\,\mathrm{AU} = 149,597,870.7\,\mathrm{km}$).

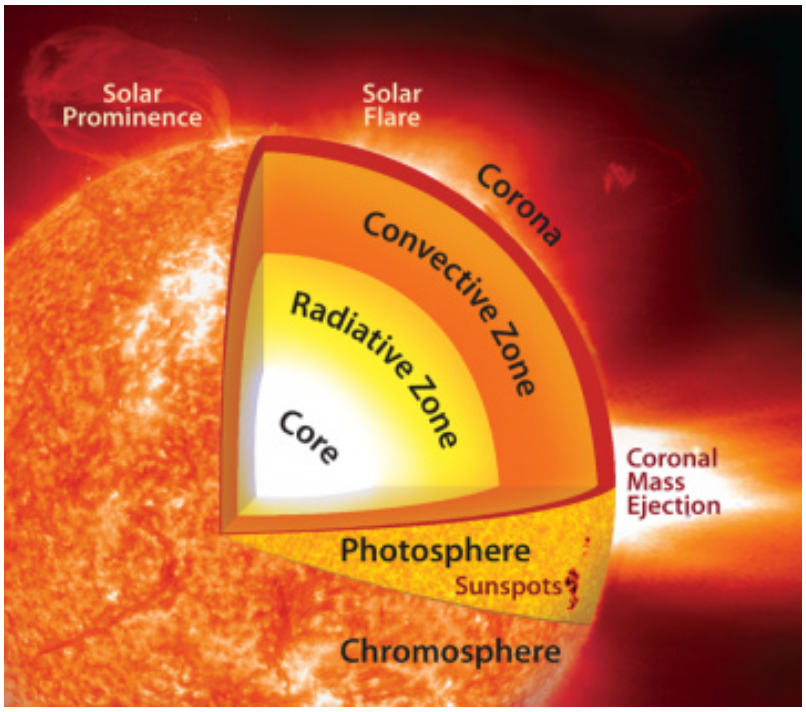

Figure 2.1: Structure of the Sun. (Figure from Thompson and Cantner, 2012).

2.2 Structure of the Sun

Because of the energy generation in its core by fusion the solar structure has a certain complexity shown in Fig. 2.1. One distinguishes between the solar interior and a solar atmosphere where the optical depth is greater and less than one, respectively.

2.2.1 Solar Interior

Although the solar interior is not directly observable its structure is known from theoretical considerations and helioseismology. In the solar interior the temperature and density decreases outwards as shown in Fig. 2.2 and is composed of the following regions.

Core

The core has a radius of approximately $0.25 R_\odot$ and its center reaches a temperature of 16×10^6 K and a density of $0.16\,\mathrm{kg/cm^3}$ (10 times the density of gold). It contains half of the mass of the Sun and with the high temperatures 99% of the Sun's fusion takes place inside the core.

Radiative Zone

The next layer surrounding the core is the radiative zone. This zone is characterized by transport of energy from the core outwards by radiation. Because of scattering the photons take about a million years to pass this layer and reach the tachocline, a thin boundary layer of $0.04\,R_\odot$ to the convective zone. The tachocline is the transition region from the solid-body rotation of the radiative zone to the differential rotation of the convective zone. It has a high shear profile that is important for the solar dynamo.

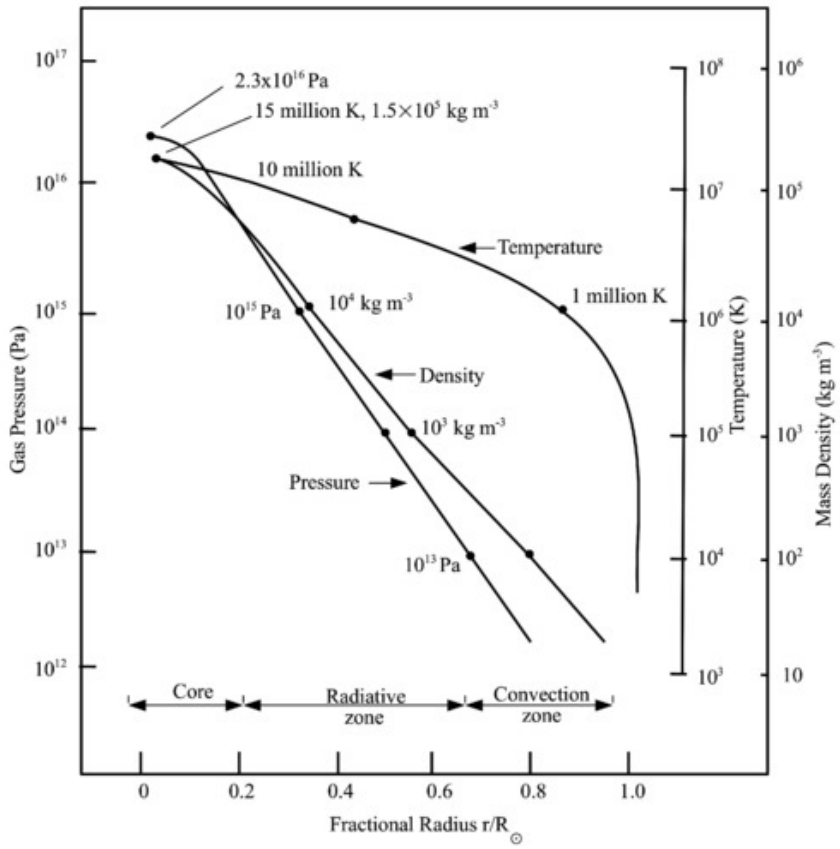

Figure 2.2: Temperature, density and pressure of the solar interior. (Figure from Lang, 2010).

Convective Zone

The convective zone is the outer layer of the solar interior. In contrast to the others layers it shows convection. Convection occurs where the adiabatic gradient is less than the temperature gradient. The adiabatic gradient is the temperature gradient due to relocation of a volume element without a transfer of heat. This condition is fulfilled in the convective zone since its temperature is low enough not to completely ionize heavier elements such as carbon, nitrogen and oxygen. This leads to increased opacity, heat capacity and convection. Convection in the Sun leads to differential rotation, where the equatorial region rotates fastest and the rotation velocity decrease towards the poles. The differential rotation eventually leads to a magnetic dynamo and the amplification and decay of the solar magnetic field during a solar cycle.

2.2.2 Solar Atmosphere

The Sun's atmosphere consists of different layers described below. Because of their tremendous temperature differences the different layers emit radiation of different wavelength. Therefore multi-wavelength observations provide a view on different parts and processes in the solar atmosphere. An example is Fig. 2.3. It shows observations by the Atmospheric Imaging Assembly (AIA, Lemen et al., 2012) and the Helioseismic and Magnetic Imager (HMI, Wachter et al., 2012) of the Solar Dynamics Observatory (SDO) satellite by NASA of radiation at wavelength of 304, 171 and 6173 Å. It is emitted by plasma at temperatures of 50,000, 0.6 million and 5,800 K usually found in the transition region, the corona and photosphere respectively. The Sun's density and temperature

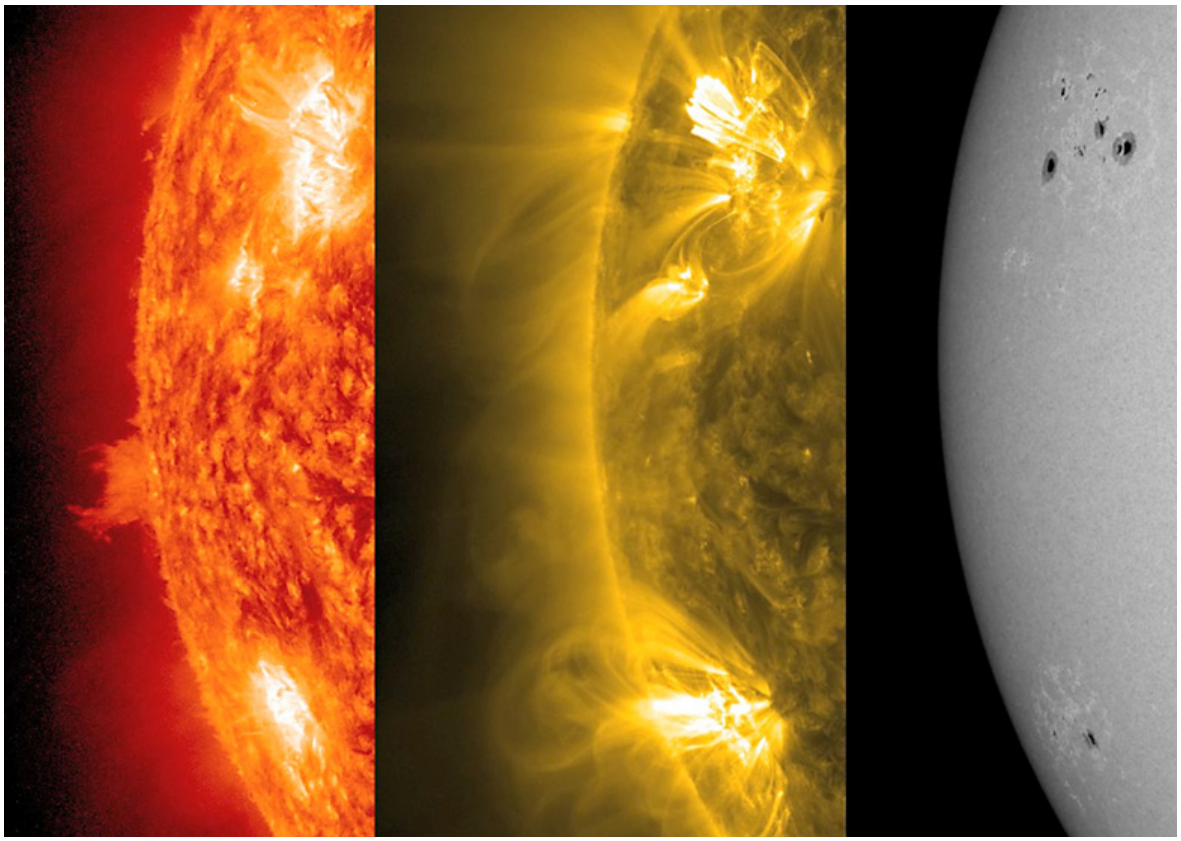

Figure 2.3: The solar atmosphere as observed from Aug. 15 to 17, 2011 by AIA/SDO at wavelength of 304, 171 and 6173 Å from left to right. The light emitting plasma has temperatures of 50,000, 0.6 million and 5,800 K and is found in the transition region / chromosphere, the upper transition region / corona and the photosphere, respectively. A pair of active regions appears as bright areas at 171 and 304 Å close to the location of dark sunspots seen at 6173 Å. Additional features of solar activity are visible, such as a quiescent prominence rising up between the active regions in the 171 Å image and many looping arcs in the 304 Å. This configuration has been the source of solar storms. (Figure from `http://sdo.gsfc.nasa.gov/gallery/main/item/96`).

are decreasing in outward direction. But the transition region at the bottom of the corona show a temperature jump from a few thousand to more than a million Kelvin (Fig. 2.4).

Photosphere

The photosphere is a thin layer of a few 100 km above the convection zone in which the Sun becomes transparent. Therefore most sunlight is emitted in this layer as black body radiation of a sphere with radius $R_\odot$ and the effective temperature of the photosphere of 5,800 K. The temperature falls from 6600 to 4300 K. Because of its little radial extension it appears as the surface of the Sun. The convective motion in the convective zone appears as granules and supergranules in the photosphere. Their typical diameters are 700 to 1,500 km and 20,000 to 54,000 km with lifespans of 8 to 15 min and 1 to 2 days, respectively.

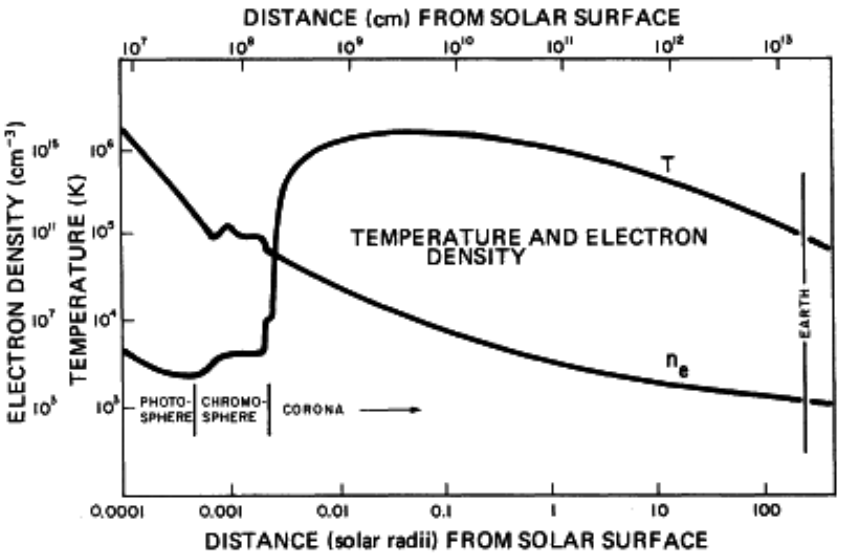

Figure 2.4: Temperature and density of the solar atmosphere. (Figure from Zombeck, 1990, p. 27).

Chromosphere

The chromosphere is a about 2,000 km deep and covers the region form the temperature minimum in the solar atmosphere at about 4,300 K to about 20,000 K at the bottom of the corona. So the inversion of the temperature trend starts in this layer. The chromosphere also shows emission lines. One of its strongest is the H_α line at 656.3 nm giving the chromosphere its red appearance. Is shows many phenomena such as filaments, spicules and the chromospheric network.

Corona

The corona is the outermost layer of the solar atmosphere. It starts with a transition region of about 1700±800 km where the temperature rise from about 20,000 K to about 1 to 2 million K. At these coronal temperatures hydrogen and helium are fully ionized. Only heavier elements like iron or calcium can keep a few electrons and produce the spectral emission lines observable in coronagraphs. Several mechanism are responsible for the coronal heating. The most important once are heating through waves and through magnetic reconnection of magnetic loops, so called nanoflares.

At a distance of a few $R_\odot$ the gravitational force is too low to bind the hot coronal plasma and it starts streaming away as solar wind (Chapter 5) to interplanetary space forming the heliosphere. Since the ions follow the magnetic field lines, this happens faster and slower in regions of open and closed magnetic field lines and leads to the fast and slow solar wind with velocities of 400 to 900 km/s and 200 to 400 km/s at a distance of 1 AU, respectively. Therefore large areas of open magnetic field lines often show a reduced plasma density and appear as coronal holes. They are often found near the polar regions. Since the magnetic field is transported by the plasma its flow and the rotation of the Sun create the Parker spiral. It consists of solar magnetic field lines centered at the Sun and spiraling outwards. Coronal loops are frequently observed features extending from the photosphere by a few percent of $R_\odot$ into the corona. Fig. 2.3 shows some nice examples near the two active regions at the 171 Å image in the middle. They are magnetic loops filled with plasma from the chromosphere and a consequence of twisted solar magnetic field lines within the solar interior.

2.3 The Solar Magnetic Field and the PFSS Method

The solar magnetic field is generated through magneto-hydrodynamical dynamo mechanisms in the convective zone. An important part of this is the Sun's differential rotation. This shows highest rotation velocities at the equator which decrease towards the poles. This azimuthal plasma flow drags field lines with it and winds them up resulting in an amplification of the solar magnetic field during one solar cycle. At its minimum the effectively dipolar solar magnetic field reverses its polarity leading to a solar magnetic cycle of 22 years (Babcock, 1961; Leighton, 1964; Leighton, 1969). At its maximum the field strengths is so high that the configuration becomes unstable and field lines start moving outwards. Where they concentrate and penetrate the photosphere they cause sunspots, magnetic loops and active regions.

As the solar wind streams away from the Sun it carries away magnetic flux. This effect is negligible close to the photosphere where the solar wind velocity is low. But at a radial distance of about 2 to 3 $R_\odot$ the velocity is so high that most field lines obtain a radial direction. In even greater distance they follow the Parker spiral because of the Sun's rotation as shown in Fig. 2.5.

The potential-field source-surface (PFSS) method by Schatten, Wilcox, and Ness (1969) is a mathematical approach to calculate the solar magnetic field according to the overall configuration described above. It calculates the field between the photosphere with a radius $R_\odot$ and a so called source surface with a radius r_s of about 2 to 4 $R_\odot$. At the photosphere the solar magnetic field can be measured with magnetographs. They use Zeeman splitting to obtain the field strength and orientation. At the source surface the magnetic field lines are assumed to be orthogonal to the source surface. The magnetic field in between can then be determined by extrapolation form the photosphere. The mathematical description according to Schrijver and De Rosa (2003) is given in appendix A.

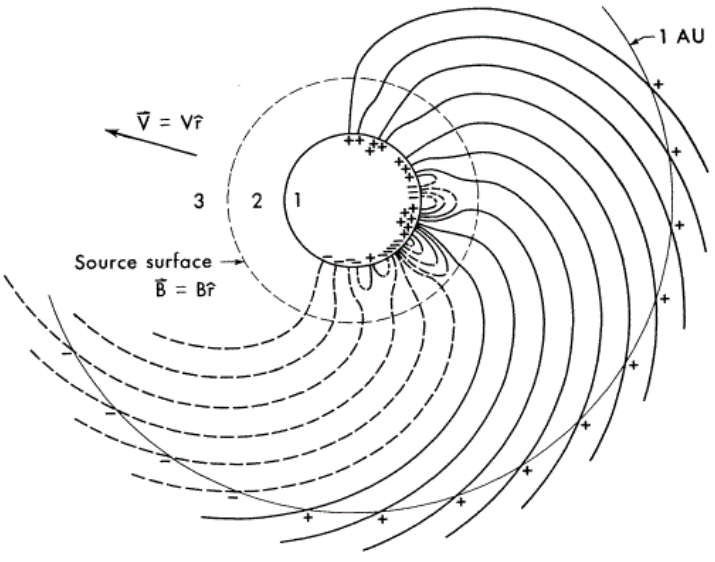

Figure 2.5: The potential-field source-surface (PFSS) method describes the solar magnetic field in region 2 between the photosphere and the source surface separating region 1 and 3 respectively. Inside the source surface field lines can be closed. Outside the field lines are assumed orthogonal to the source surface since they are carried away by the solar wind forming the Parker spiral. Field lines of both polarities (solid and dashed lines) are shown. (Figure from Schatten, Wilcox, and Ness, 1969).

2.3.1 The PFSS SolarSoft Package

The PFSS method is implemented to the PFSS package of SolarSoft (Bentely and Freeland, 1998). Solarsoft is an Interactive Data Language (IDL) library for solar data analysis. The PFSS package uses magnetograms from the Helioseismic and Magnetic Imager (HMI) (Wachter et al., 2012) of the SDO satellite. It obtains the photospheric magnetic field on the backside of the Sun with a model of solar surface activity (Schrijver, 2001; Schrijver and Title, 2001) that is based on a surface-diffusion model. Fig. 2.6 to 2.9 show the computed solar magnetic field on June 23, 2012 at 12:04 UTC from four different viewing angles. The source surface had a radius of $r_s = 4R_\odot$ and the starting points of the field lines were chosen uniform at $r = 2R_\odot$. They were then drawn following the gradient of Φ in both direction. Alternative drawing options are available, such as a field line density proportional to the magnetic flux and starting points at a sphere of any radius between $R_\odot$ and r_s. It is also possible to increase or decrease the average field line density and to restrict the rendered field lines to a limited longitude and latitude range.

2.4 Solar Activity and Space Weather

The Sun emits most but not all of its energy via thermal radiation. Because of its magneto-hydrodynamical dynamo mechanisms in the convective zone energy is also transformed into magnetic fields and sporadically released (Section 2.3). The sudden additional release of mainly nonthermal energy is called solar activity and shows a wide variety of phenomena. Most of them are found in active regions. The effects of solar activity on interplanetary space and on the Earth are referred to as space weather.

2.4.1 Active Regions

Active regions appear in regions where magnetic field strengths exceed about 100 G. They show increased temperatures and X-ray fluxes and can develop a complex structure. For higher field strength they often become the site of sunspots, coronal loops, prominences, radio bursts, flares, coronal mass ejections and solar energetic particles. The corona above an active region can exceed 10 times the density and 2 times the temperatures of the surrounding. Fig. 2.3 shows two active regions, one in the upper and one in the lower half of the region, that is shown at different wavelength. Their increased emission is visible at 304 and 171 Å. A quiescent prominience in the middle is best resolved at 304 Å. Coronal loops with typical length of 10^4 to 10^5 km and temperatures of 2.5×10^6 K are resolved at 171 Å. Sunspots are seen at the 6173 Å image.

2.4.2 Sunspots

Sunspots are regions in the photosphere where magnetic field lines leave the Sun and emerge into the corona. Since the magnetic field reduces convection hot plasma rises slower from inside so that these regions are cooler than their surrounding. For that reason they emit less thermal radiation and appear dark. They usually occur in pairs with opposite magnetic polarity within an area of ± 30 degrees from the equator. They consist of a central dark region called umbra with a typical diameter of 10,000 to 20,000 km surrounded by a brighter region called penumbra with a typical width of

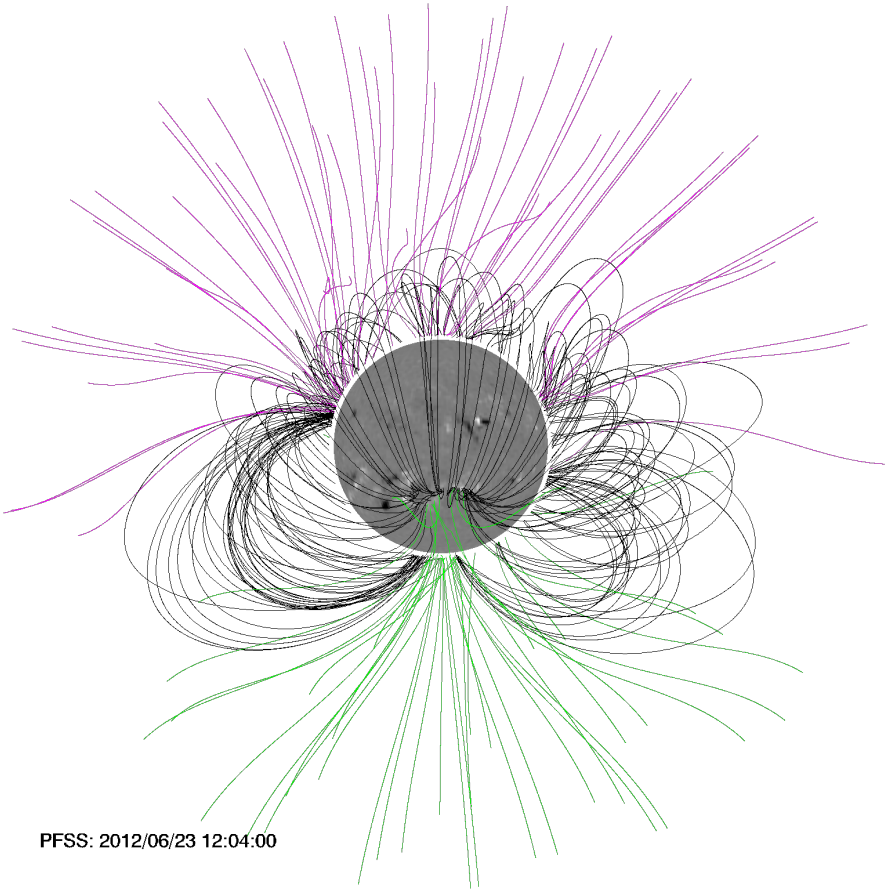

Figure 2.6: Solar magnetic field on June 23, 2012 (11:00 UTC) as obtained with the PFSS package of SolarSoft based on HMI magnetograms of the photosphere (grey scaled surface) as observed from the direction of Earth. Open field lines of opposite polarity are shown in red and green. Closed field lines are black.

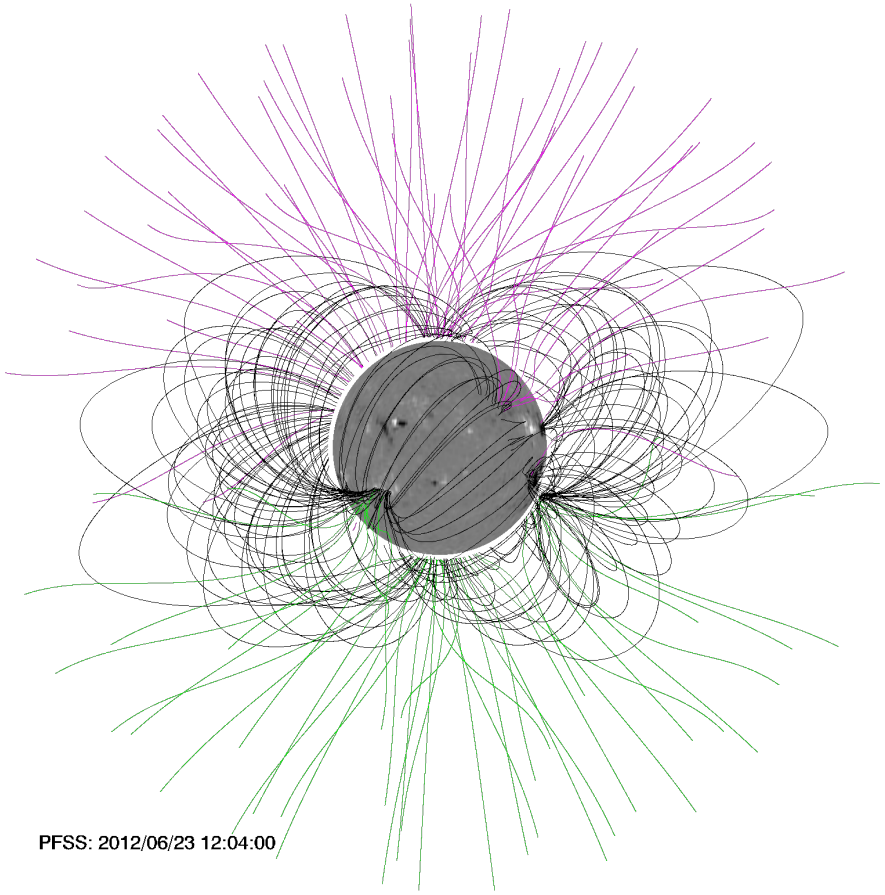

Figure 2.7: The same as Fig. 2.6 but rotated by 45 degrees around the solar rotation axis.

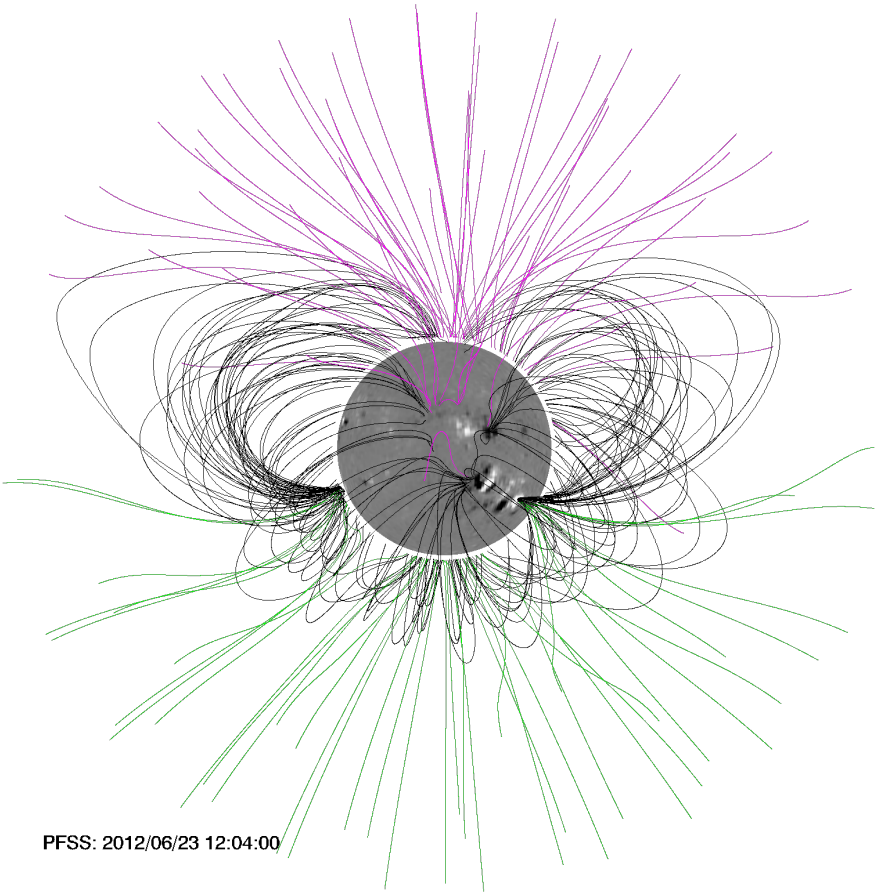

Figure 2.8: The sane as Fig. 2.6 but rotated by 90 degrees around the solar rotation axis.

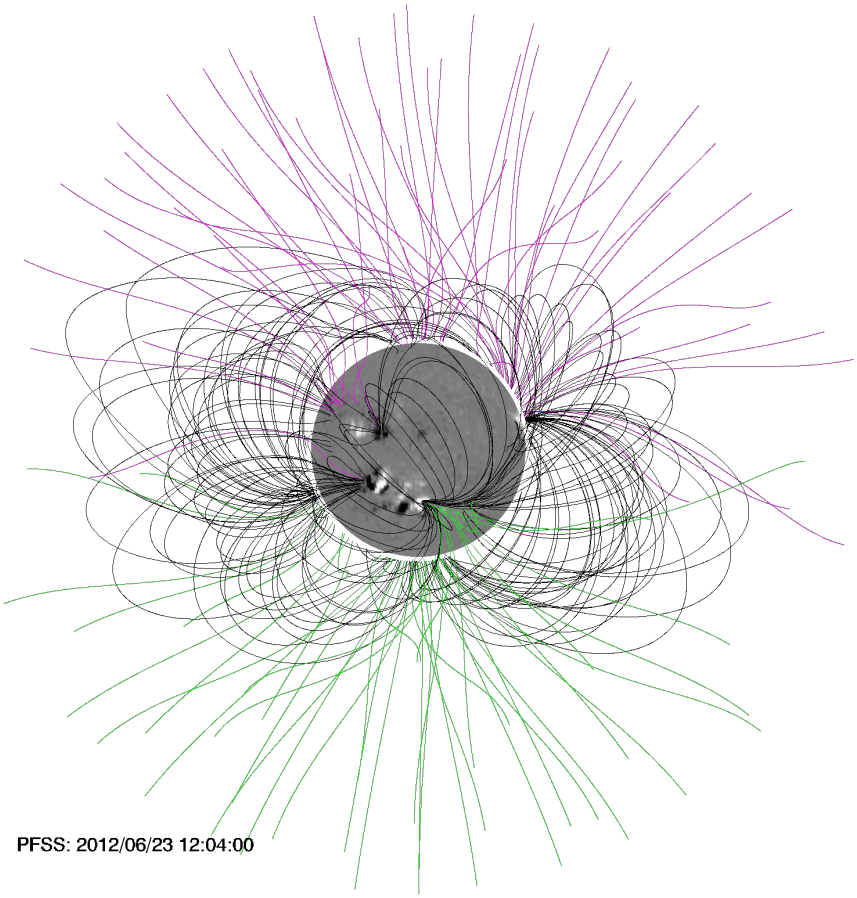

Figure 2.9: The same as Fig. 2.6 but rotated by 135 degrees around the solar rotation axis.

5,000 to 7,000 km. The umbra has a typical temperature of only 3,700 K, which is a about 40% less than the photosphere. Typical field strengths are 2,000 to 3,000 G, although values up to 4,000 G can be reached. Their typical lifetime is a few day but can range to a few month. The right image of Fig. 2.3 shows sunspots at the top and bottom of the photosphere.

2.4.3 Prominences

Prominences are large scale structures of cool and dense plasma created at active regions and extending into the corona with a length and height of 200,000 and 50,000 km respectively. One distinguishes between quiescent and active prominences. The former are long lasting with lifetimes of many month. The later are associated with solar flares and dynamic structures with lifetimes of minutes to hours. They can also eject material as an eruptive prominence. An example of an eruptive prominence is shown in Fig. 2.10. It originates from a flare region at the top of the figure. When viewed at 656 nm (the Hα line of hydrogen) and when they are located in front of the solar disk prominences appear as dark ribbons called filaments.

2.4.4 Solar Flares

Solar flares are sudden brightenings in an active region as seen at the top of Fig. 2.10. They are well visible at wavelength of 656 nm (Hα line of hydrogen) but also throughout the whole electromagnetic spectrum from radio to hard X-rays emission as shown by Fig. 2.11. The total energy release varies from about 10^{22} to 3×10^{25} J. Flares are categorized according to their peak X-ray flux. The categories are A, B, C, M and X

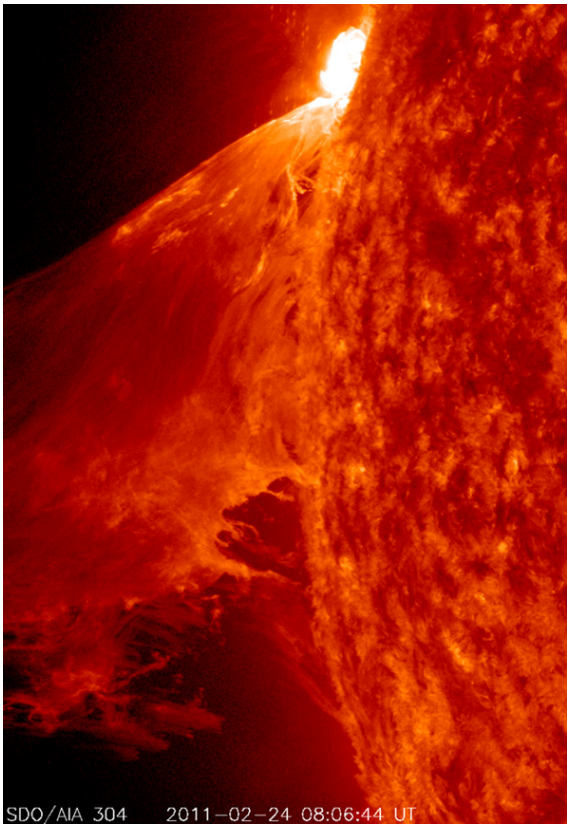

Figure 2.10: M 3.6 class flare near the limb of the Sun with an erupting prominence that twisted over a period of 90 minutes on Feb. 24, 2011. This event was captured by the SDO satellite in extreme ultraviolet light at 304 Å corresponding to temperatures of 50,000 K found in the transition region of the lower corona. Some of the plasma fell back to the Sun and other portions were ejected into space as coronal mass ejections. (Figure from `http://sdo.gsfc.nasa.gov/gallery/main/item/60`).

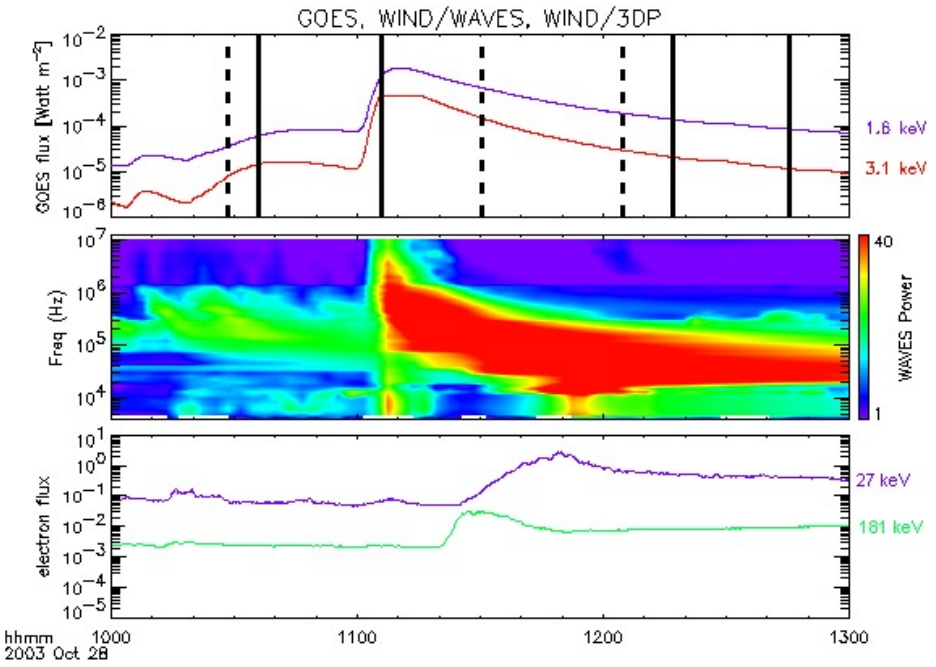

Figure 2.11: X-ray, radio and electron flux during a solar flare. The the sudden increase at 11:15 UT and the slow decrease in the following hours is apparent for all fluxes. (Figure from Miteva, 2007).

with X being the brightest. Each category has a linear energy scale expressed from 1 to 9.9. Energy released in solar flares is primarily put into acceleration of particles and direct plasma heating. The majority of the released energy is finally converted into EM radiation and into a CME, in case one is associated (Warmuth and Mann, 2016). The energy is originally stored in coronal magnetic fields and the energy release is triggered by magnetic reconnection. Flares rise to maximum intensity within a few minutes to hours and disappear within a few hours to days. They occur predominantly in active regions with a complex and dynamic magnetic field structure and the magnetic energy seems to be the only energy source that can explain them. Different types of radio bursts, solar energetic particle events and CMEs are also often observed with flares (Svestka, 1981; Heyvaerts, 1981; Benz, 1993). Flares are besides CMEs the main sources of space weather. Their energetic particle events sometimes observed as aurora on Earth are radiation hazards for satellites and astronauts. Their X-ray flux can disturb high frequency radio transmission by ionization of the upper atmosphere. This can also severely reduce the positioning accuracy from navigation satellite systems. The X-ray flux can also accelerate the orbital decay of low orbit satellites by expanding the upper atmosphere through heating. Fig. 2.12 shows the radiance of flares and its associated phenomena in comparison to the emission of the quiet Sun.

2.4.5 Coronal Mass Ejections (CMEs)

Coronal mass ejections are sudden ejections of 10^{11} to 10^{13} kg of magnetized coronal plasma usually from active regions into interplanetary space with velocities of 100 to a few 1000 km/s. They are associated with solar flares and eruptive prominences as shown in Fig. 2.10. Fast CMEs can drive shock fronts on which solar energetic particles (SEP) are accelerate. CME's contribute significantly to space weather. When a CME reaches the Earth's magnetosphere it can cause geomagnetic storms usually accompanied by aurorae and lead to the disruption of radio transmissions (including signals from navigation satellites) and cause damage to satellites and electric transmission facilities.

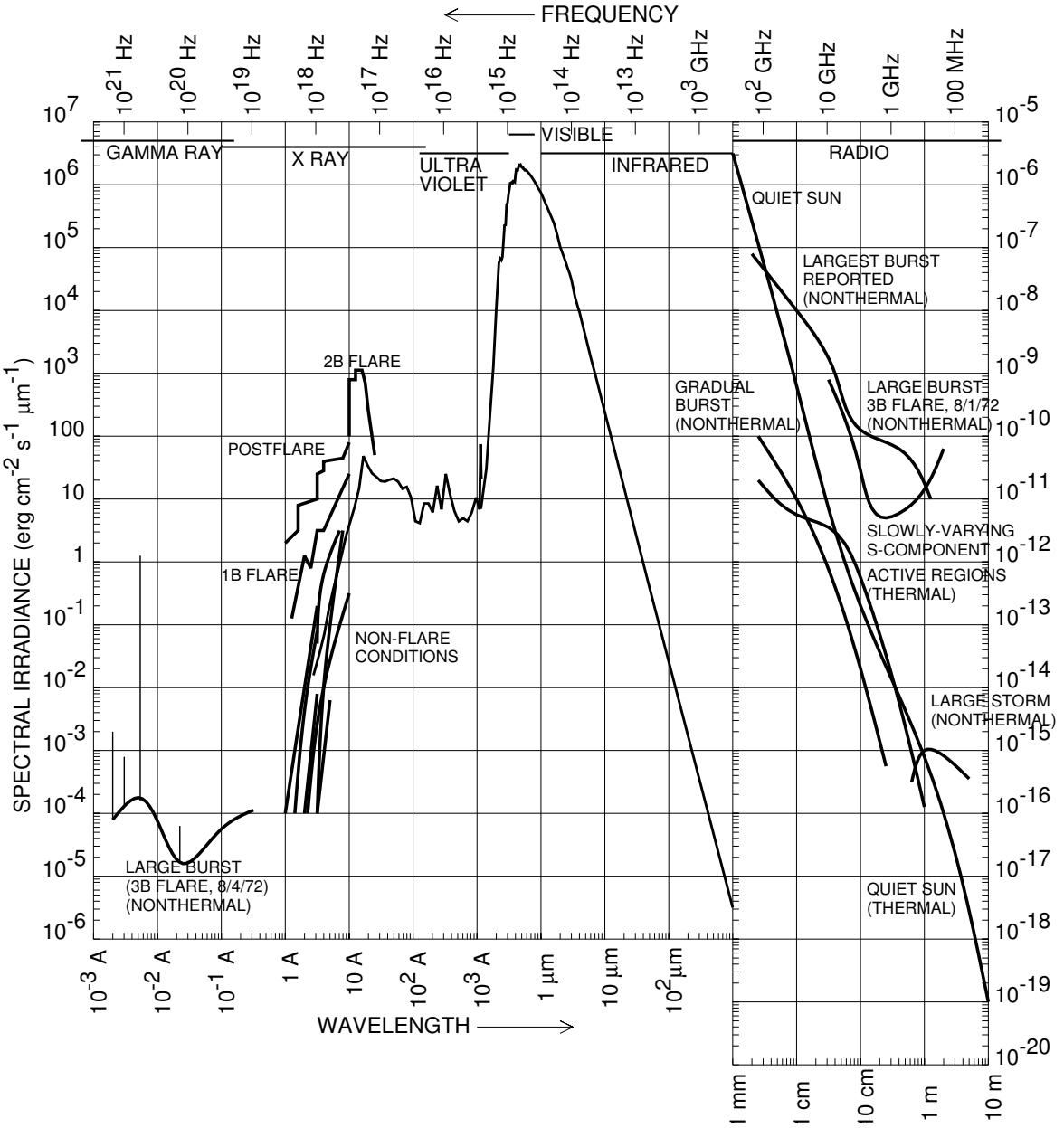

Figure 2.12: Solar flux density (irradiance) spectrum from γ-rays to radio waves. The spectrum is shifted by 12 orders of magnitude in the vertical axis at $\lambda = 1\,\mathrm{mm}$ to accommodate for the large dynamic range in spectral irradiance (Figure from Aschwanden (2004) after Zombeck (1990)).

2.4.6 Solar Energetic Particles (SEP)

Solar energetic particles refers to particles that have been accelerated in significant amount for example on a CME shock front or by a flare. In the first case, a gradual SEP event is generated which lasts for several days and occurs with a rate of 10 per year. In the second case an impulsive SEP event is generated which only lasts for hours and occurs with a rate of 100 per year. SEPs also contribute as space weather and can be a hazard to astronauts, since a typical spacecraft shielding does not provide sufficient protection.

Chapter

3

Solar Radio Emission

Solar radio radiation mainly originates from three different emission processes: thermal free-free (or Bremsstrahlung), gyro and plasma emission. While the thermal radiation is continuously emitted from the corona as a uniform background radiation the nonthermal plasma emission is triggered by events of solar activity and appears in solar radio bursts which can exceed the thermal background radiation by orders of magnitude. The study of solar radio burst is interesting since its different types reveal various information about the associated processes (Warmuth and Mann, 2005b; Mann, 2010).

The different events cause radio emissions of different spectral flux density (Fig. 3.1) and they occur at different coronal heights (Fig. 3.2). Units of spectral flux density (or spectral irradiance) are the Jansky ($1\,\mathrm{Jy} = 10^{-26}\ \mathrm{Wm^{-2}Hz^{-1}}$) and the solar flux unit ($1\,\mathrm{SFU} = 10^4\,\mathrm{Jy}$) in radio astronomy and solar radio astronomy, respectively.

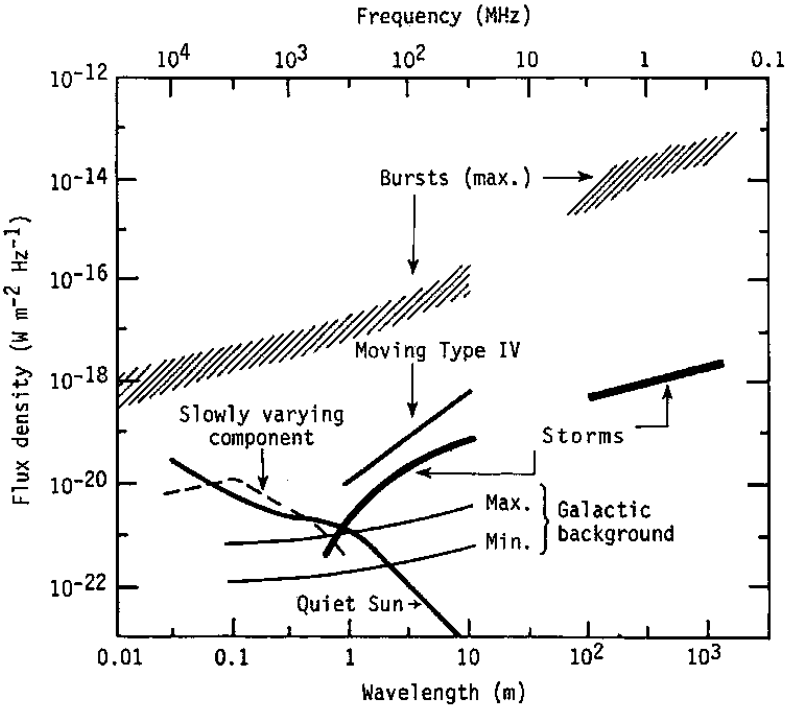

Figure 3.1: Spectral flux density of different radio sources from the Sun in comparison to the galactic background flux. The Sun is the strongest radio source on the sky at wavelength of less than 3 m i.e. frequencies greater 100 MHz. (Figure from Nelson, Sheridan, and Suzuki, 1985).

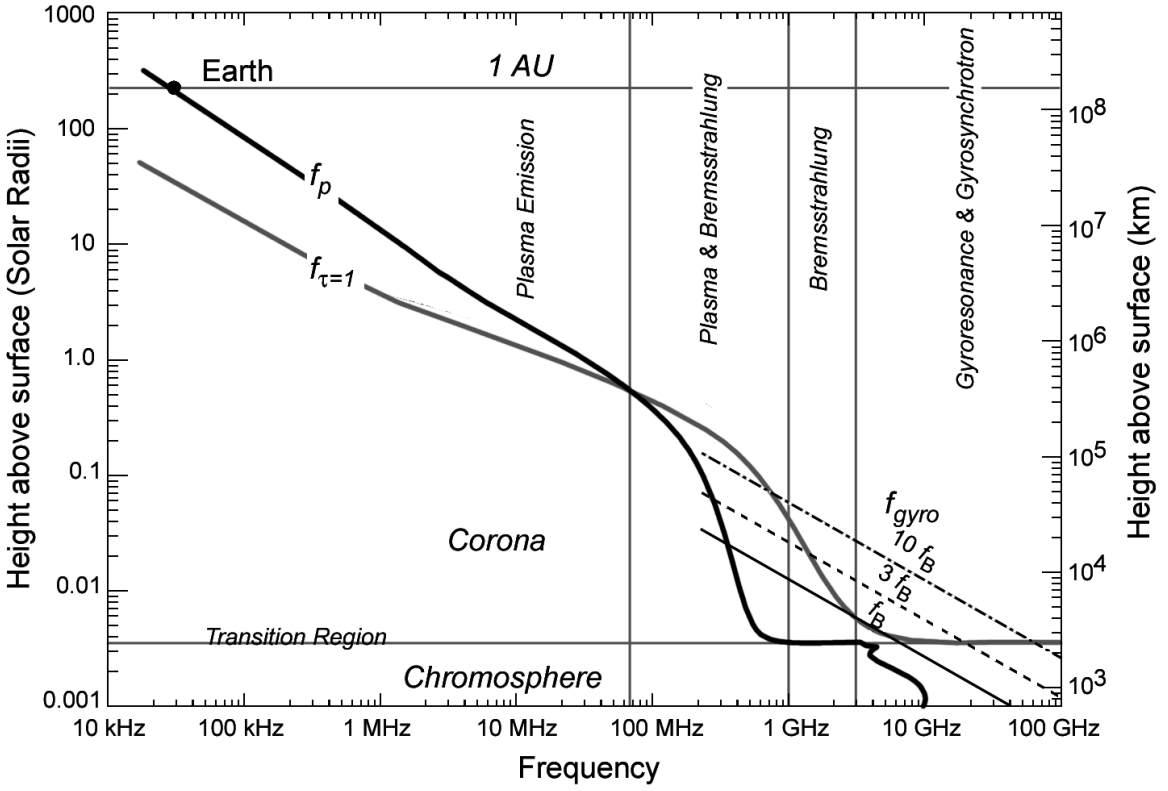

Figure 3.2: Height of emission region in the solar atmosphere vs. emission frequency. f_p, f_{gyro} and $f_{\tau=1}$ refer to the plasma frequency, gyro frequency and the frequency at which free-free emission reaches optical depth unity. The different emissions types dominate at different frequency ranges. (Figure from Krueger, 1979).

3.1 Thermal Free-Free Emission / Bremsstrahlung

The coronal gas of the quiet Sun has an effective temperature of about 1×10^6 K so that it is fully ionized and the electrons and protons move freely. By collision mainly the electrons lose energy through Bremsstrahlung which in this case is also called free-free emission since the particles remain free after their interaction. Because of this thermal emission mechanism the corona behaves like a black body at low radio frequencies (Fig. 3.3). The emission can be calculated as follows (see Klose, 1995). The spectral radiance emitted from a black body is given by Planck's law

$$I_\Omega(\nu, T) = \frac{2h\nu^3}{c^2} \frac{1}{e^{h\nu/kT} - 1} \tag{3.1}$$

with the following parameters:

I_Ω - spectral radiance ($[I_\Omega] = \mathrm{Wm^{-2}\,Hz^{-1}\,sr^{-1}}$),
ν - frequency,
T - effective temperature of the black body,
h - Planck constant (6.62×10^{-34} Js),
k - Boltzmann constant (1.38×10^{-23} J/K),
c - speed of light in the medium (3.00×10^8 m/s $\times$ index of refraction).

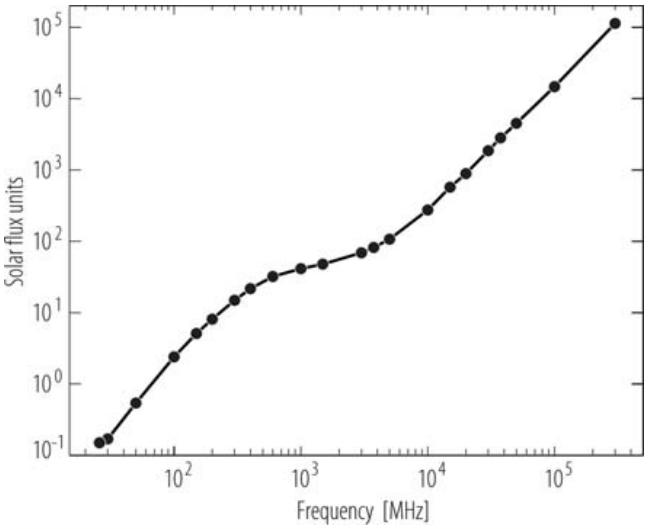

Figure 3.3: Spectral flux density of radio emission from the quiet Sun observed during a minimum of solar activity. At 0.5 and 5 GHz the transition from coronal to photospheric black body radiation with effective temperatures of 1×10^6 K and 5800 K respectively is visible. (Figure from Benz, 2009).

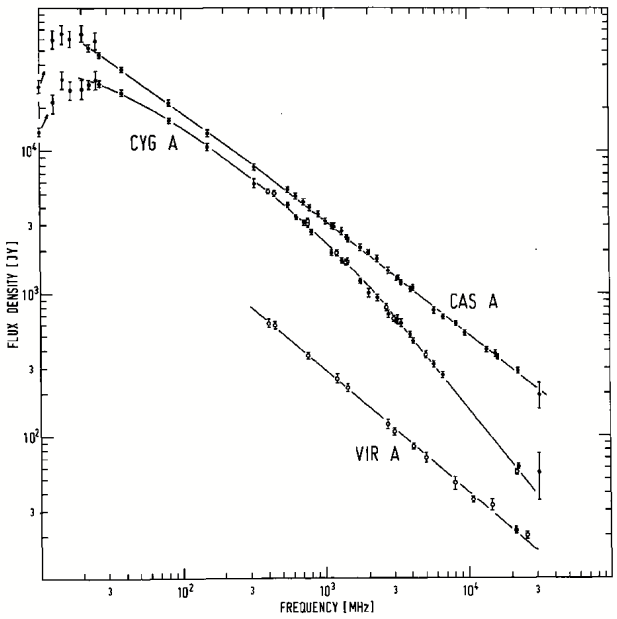

Figure 3.4: Spectral flux density of the three strongest radio sources besides the Sun: Cassiopeia A, Cygnus A and Virgo A. In comparison with Fig. 3.3 one finds that these sources have higher flux densities (1 SFU=10^4 Jy) than the Sun at frequencies less than 100 MHz. (Figure from Baars et al., 1977).

In the case of solar radiation $h\nu \ll kT$ and so the approximation by Rayleigh-Jeans law can be used:

$$I_\Omega(\nu, T) = \frac{2\nu^2}{c^2} kT. \tag{3.2}$$

The spectral flux density of a black body is obtained by the integral over all emission directions, i.e. the corresponding half-space Ω, as

$$E(\nu, T) = \int I_\Omega(\nu, T) \cos\theta \, d\Omega = I_\Omega(\nu, T) \int_{\phi=0}^{2\pi} \int_{\theta=0}^{\pi/2} \cos\theta \sin\theta \, d\theta \, d\phi = \pi I_\Omega(\nu, T). \tag{3.3}$$

So the spectral flux density of the thermal radiation from a 10^6 K hot corona at a frequency of $\nu = 100$ MHz (wavelength of 3.00 m) near the Sun is

$$E_c(100\,\mathrm{MHz}) = \pi I_\Omega(100\,\mathrm{MHz}, 10^6\,\mathrm{K}) = 9.7 \times 10^{-18} \frac{\mathrm{W}}{\mathrm{m^2 Hz}}. \tag{3.4}$$

The spectral flux density received on Earth E_E in a distance of r_E=1 AU scales

inversely with the surface area the radiation passes, so that

$$E_E(100\,\mathrm{MHz}) = \frac{R_\odot^2}{r_E^2} E_c(100\,\mathrm{MHz}) = 2.1 \times 10^{-22} \frac{\mathrm{W}}{\mathrm{m^2 Hz}} = 2.1 \times 10^4\,\mathrm{Jy} = 2.1\,\mathrm{SFU}. \quad (3.5)$$

This calculated value is approximately the value observed (Fig. 3.3). In the range from 0.5-5 GHz the spectral flux density shows a transition from the black body radiation of the corona to that of the photosphere with effective temperatures of 5800 K. This transition occurs because the corona becomes optically thin at this frequency range and so loses its black body characteristic.

Fig. 3.4 shows a comparison of the spectral flux of the quiet Sun with that of Cassiopeia A, Cygnus A and Virgo A. One can see that for frequencies grater than 100 MHz the Sun exceeds the spectral flux from these strongest radio sources of the night sky.

The spectral flux from the total corona at 100 MHz is provided by the integral over the total surface area ($4\pi 1\mathrm{AU}^2$) as

$$\Phi_\odot(100\,\mathrm{MHz}) = 4\pi(1\mathrm{AU})^2 E_E(100\,\mathrm{MHz}) = 59\,\mathrm{W/Hz}. \quad (3.6)$$

Now one can estimate the power of thermal radio emission by the Sun. Since the spectral flux increases rapidly with frequency (Fig. 3.4) $\Phi_\odot(100\,\mathrm{MHz})$ can serve as a lower limit. In the frequency range from 100 to 200 MHz one finds:

$$\int_{100\,MHz}^{200\,MHz} \Phi_\odot(\nu) d\nu > \Phi_\odot(100MHz) \cdot (200 - 100)\,\mathrm{MHz} = 5.9 \times 10^9\,\mathrm{W}. \quad (3.7)$$

This is just a crude estimate. The actual radio power emitted by the Sun is higher.

3.2 Gyro Emission

Gyro emission is caused through solar magnetic fields which force energetic electrons to spiral or gyrate around the field lines because of the Lorentz force. This acceleration of charge results in an electromagnetic wave. Its frequency is given by the gyrofrequency of the particle

$$f_g = \frac{1}{2\pi} \frac{eB}{m_\mathrm{e}} \quad (3.8)$$

with the magnetic field B and the charge e and mass m_e of the electron. One distinguishes between cyclotron, gyrosynchrotron and synchrotron emission depending on whether non-, mildly or highly relativistic electrons are involved. The cyclotron emission causes bright coronal emission near sunspots with strong magnetic fields. The gyrosynchrotron emission is observed with high frequency bursts of solar flares.

A special form of gyro emission is the electron-cyclotron maser (ECM) emission as for example suggested by Wu and Lee (1979). For a review see Dulk (1985). It has been proposed as possible mechanisms to explain some of more complex short timescale bursts such as zebra patterns, radio spikes and solar S bursts (Morosan et al., 2016). The condition for ECM radio emission is a plasma frequency f_pe less than f_g. (Vocks and Mann, 2004; Morosan et al., 2016) have shown, that this condition can be satisfied in active regions in the corona with high magnetic fields. These conditions also constrain the emission frequencies to at least a few hundred megahertz.

3.3 Plasma Emission and Radio Bursts

Plasma emission is nonthermal radiation generated by solar activity through plasma oscillation also known as Langmuir waves which is a high frequency plasma wave. Its frequency

$$f_{\rm pe}(N_{\rm e}) = \frac{1}{2\pi}\left(\frac{e^2}{\epsilon_0 m_{\rm e}} N_{\rm e}\right)^{1/2} = 9.00 \times (N_{\rm e}{\rm m}^3)^{1/2}{\rm Hz} \tag{3.9}$$

which is only a function of the electron number density $N_{\rm e}$ of the plasma.

$f_{\rm pe}$ is the frequency of a collective oscillation between the electrons and ions because of their electrostatic force if the thermal velocity is neglected. For higher thermal velocities that cannot be neglected and an additional term appears in this equation which shifts the Langmuir frequency to higher frequencies. In the corona this shift is only small. Via scattering on ion density fluctuations or coalescence with ion acoustic waves a Langmuir wave can transform into an electromagnetic wave of same frequency. This leads to fundamental plasma emission which can leave the corona as radio wave in the direction of decreasing plasma density. In the other direction the radio wave is absorbed and so the corona is opaque to the radio waves of frequency $f_{\rm pe}$. Similarly harmonic plasma emission can be produced via coalescence of two high-frequency electrostatic waves. Details about these nonlinear processes that occur in the corona and lead to the appearance of solar radio bursts are described by Melrose (1985). The radio emission from solar radio bursts can exceed the thermal radio emission by 8 orders of magnitude (see e.g. Dulk, 2000).

Eq. 3.9 provides the relation between the frequency of the plasma emission and the plasma density at the emission region. Because of gravity the coronal density decreases with radial distance. So Eq. 3.9 leads to a frequency–height relation. The frequency–height relation is useful for studying the propagation of solar radio bursts through the corona. It is recorded in dynamic radio spectra. They display the flux density in an observed frequency range versus time. Fig. 3.5 sketches the signatures of

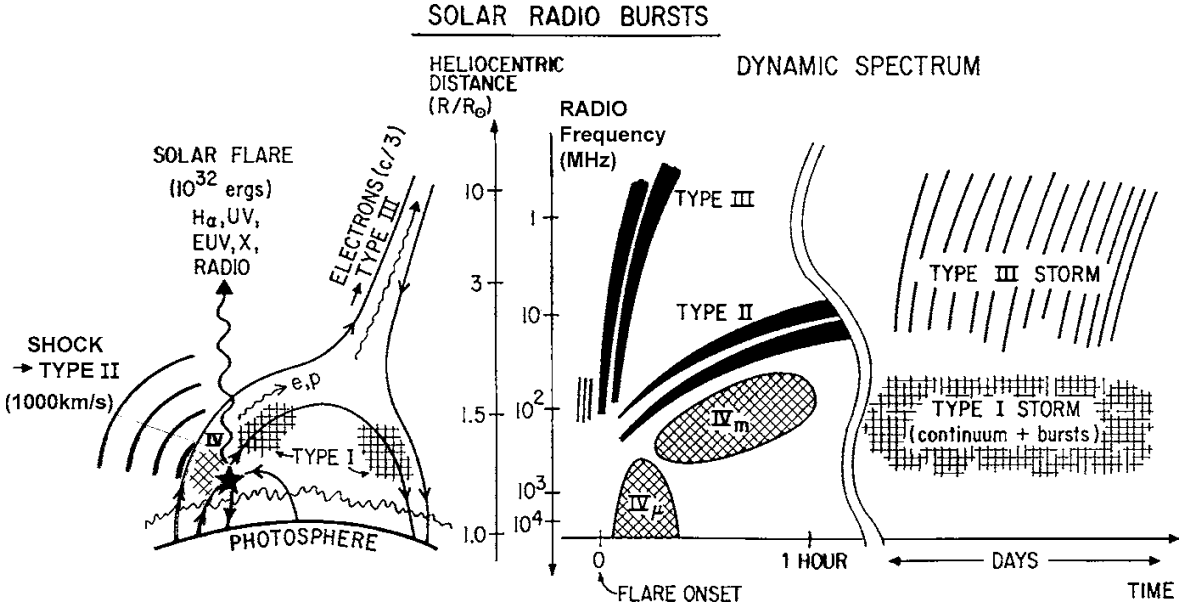

Figure 3.5: Processes of solar activity (left) and their associated types of solar radio bursts and signatures in dynamic radio spectra (right). (Figure from Kundu, 1965).

Solar Radio Burst Classifications

TYPE	CHARACTERISTICS	DURATION	FREQUENCY RANGE	ASSOCIATED PHENOMENA
I	Short, narrow-bandwidth bursts. Usually occur in large numbers with underlying continuum.	Single burst: ~ 1 second Storm: hours - days	80 – 200 MHz	Active regions, flares, eruptive prominences.
II	Slow frequency drift bursts. Usually accompanied by a (usually stronger intensity) second harmonic.	3- 30 minutes	Fundamental: 20 – 150 MHz	Flares, proton emission, magnetohydrodynamic shockwaves.
III	Fast frequency drift bursts. Can occur singularly, in groups, or storms (often with underlying continuum). Can be accompanied by a second harmonic	Single burst: 1 - 3 seconds Group: 1 -5 minutes Storm: minutes - hours	10 kHz – 1 GHz	Active regions, flares.
IV	Stationary Type IV: Broadband continuum with fine structure	Hours - days	20 MHz – 2 GHz	Flares, proton emission.
	Moving Type IV: Broadband, slow frequency drift, smooth continuum.	30 – 2 hours	20 – 400 MHz	Eruptive prominences, magnetohydrodynamic shockwaves.
	Flare Continua: Broadband, smooth continuum.	3 – 45 minutes	25 – 200 MHz	Flares, proton emission.
V	Smooth, short-lived continuum. Follows some type III bursts. Never occur in isolation.	1-3 minutes	10 - 200 MHz	Same as type III bursts.

NOTES: In nearly all cases, drifting bursts drift from high to low frequencies.
The Frequency Range is the typical range in which the bursts appear – not their bandwidth.
The sub-types of type IV are not universally agreed upon and are thus open to debate.

Table 3.1: Solar radio burst classifications as provided by the Commonwealth of Australia 2015, bureau of meteorology, space weather services, `http://www.ips.gov.au/World_Data_Centre/1/9/4`).

the different types of solar radio bursts that are observed in dynamic radio spectra of the Sun. It also illustrates different processes of a flare which can generate the different radio bursts. The two axes in the middle show the relation between height and frequency. One can see that some bursts like the type III have a narrow structure and represent the fast propagation of a compact radio source through the corona. Other burst like a type I storm cover a wide frequency range and indicate the repeated occurrence of radio bursts in a large region of the corona for several days.

The classification of solar radio bursts was established by the pioneers of solar radio astronomy. One distinguishes five types of solar radio bursts. Burst of type I-III, IV and V are named according to Wild and McCready (1950), Boischot (1957) and Wild, Sheridan, and Trent (1959) respectively. The characteristics of the different types of radio bursts are summarized in Table 3.1.

A detailed description is given (Warmuth and Mann, 2005a) and is summarized below. The following examples of dynamic radio spectra of different solar radio burst were observed with the radio spectrometer of the observatory of the Leibniz-Institut für Astrophysik Potsdam in Tremsdorf, Germany (OSRA, Mann et al., 1992).

3.3.1 Type I Burst

Type I bursts are short in duration ($\leq$1 s) and narrow in bandwidth ($\leq$10 MHz) but often appear in large numbers as noise storms (Fig. 3.6).

They are explained by energy release in closed coronal structures which leads to the acceleration of electrons to a few thermal energies which then excite the plasma. Because noise storms last from hours to days they are generally not associated with

flares.

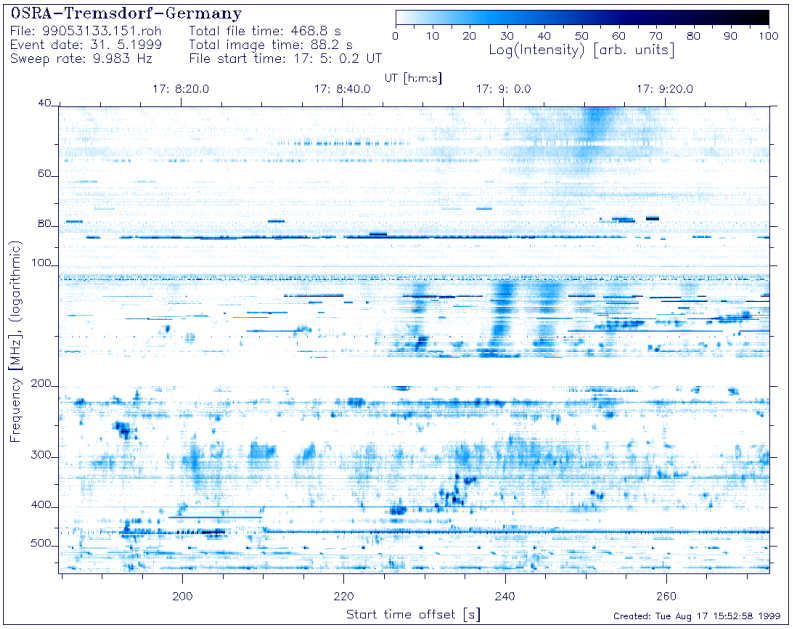

Figure 3.6: Solar type I bursts observed by the OSRA spectrometer. They are visible as compact spots covering a few MHz and a few seconds in the frequency range between 200 and 400 MHz.

3.3.2 Type II Burst

Type II bursts have longer lifetimes and broader bandwidth than type I burst and are slowly drifting (0.1−1 MHz/s) to lower frequencies. Fundamental and harmonic emission is observable. Fig. 3.7 shows an example.

Type II bursts are generated through shock waves which are propagating through the corona and interplanetary space and which excite Langmuir waves and electrons. Therefore they are associated with flares and CMEs and potentially space weather. Type II bursts sometimes show a herringbone fine structure. Herringbone radio bursts are a result of many short type III bursts and an indication of shock accelerated electron beams.

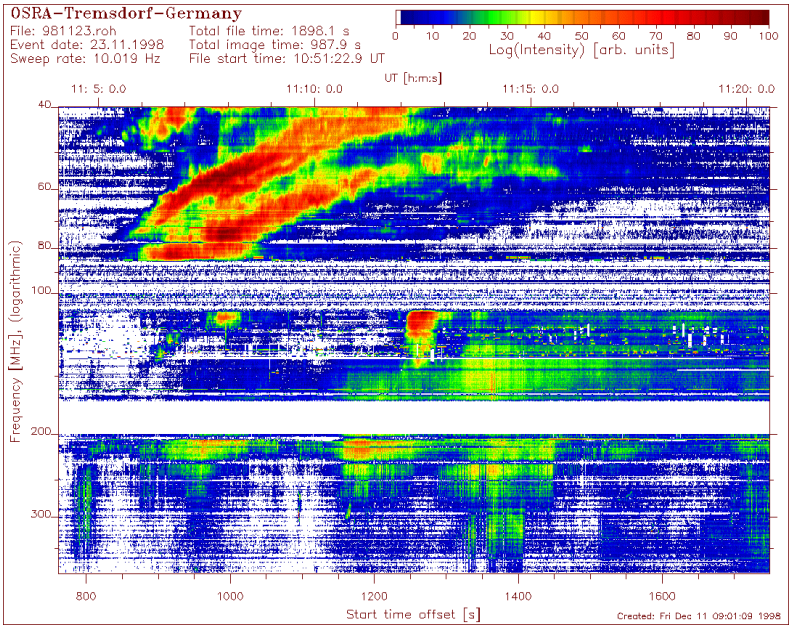

Figure 3.7: Solar type II (upper left) and type IV burst (lower area) in the frequency range from 40 to 80 and 100 to 380 MHz observed by the OSRA spectrometer.

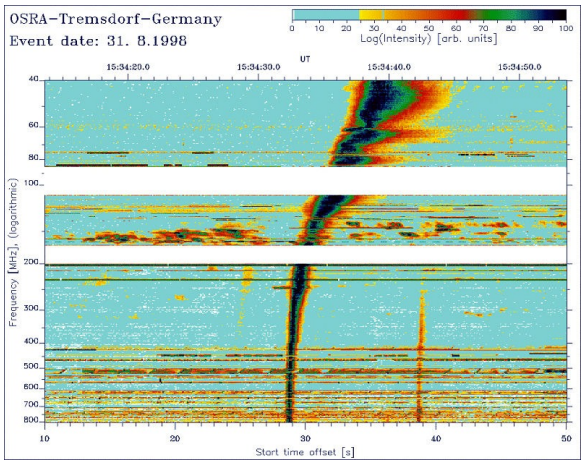

Figure 3.8: Solar type III burst with a broad frequency range observed by the OSRA spectrometer.

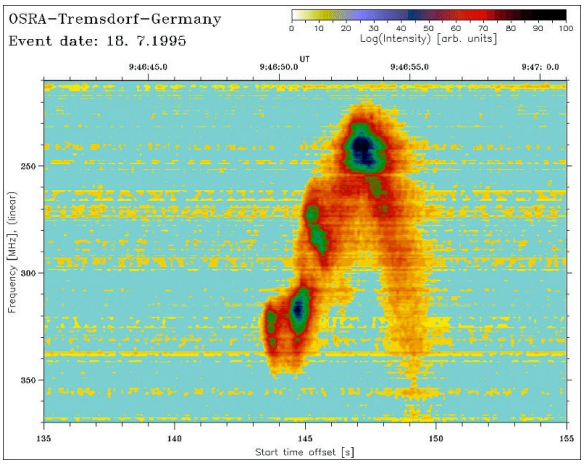

Figure 3.9: Solar U burst, a rare variation of a type III burst with the shape of an inverted U, observed by the OSRA spectrometer.

3.3.3 Type III Burst

Type III bursts are broadband events with lifetimes of seconds occurring at a wide frequency range. They are fast drifting (∼100 MHz/s) usually from high to low frequencies and usually appear in groups.

They are explained as plasma emission excited by electron beams propagating through the corona along magnetic field lines (Gopalswamy, Kundu, and Szabo, 1987). Typical velocities range from 0.15 to more than 0.5c (Reid and Ratcliffe, 2014). If the electrons follow open magnetic field lines the plasma density and hence the emitted frequency decreases steadily as shown in Fig. 3.8. If the electrons are trapped on closed field lines they can change their propagation direction towards the Sun leading to an increasing plasma frequencies and an inverted J or U bursts as shown in Fig. 3.9. In case of the J burst, the emission stops when the beam reverses direction. Other rare variations of type III bursts are revers and bi-directional type III bursts where the electron beam is accelerated towards the Sun or simultaneously in the in- and outward direction. There are also type IIIb burst, which show fine structure of fragmented or clumpy emission. The cause is seen in density fluctuation of the coronal plasma. And there are type III-l burst which start at low frequencies (as indicated by the letter l) of 10 MHz. They are associated with CMEs. Type III storms are periods of hours or days where type III bursts occur in quick succession. They are associated with type I noise storms which occur at higher frequencies. In any case the solar type III bursts are valuable probes of the structure of the coronal plasma. Table 3.2 summarizes some of the observed properties of solar type III bursts.

The theory explaining type III burst radio emission is complex and had to be revised several times since it was introduced by Ginzburg and Zhelezniakov (1958) to be consistent with observations. Melrose (2009) and Reid and Ratcliffe (2014) describe this development in detail. The stages leading to fundamental and harmonic plasma emission are summarized in Fig. 3.10. The principle idea is that a beam of accelerated electrons creates a so called bump-in-tail instability in the coronal plasma which results in the emission by nonlinear interaction with another plasma wave. Sturrock (1964) pointed out that the energy loss of the electrons would only allow a propagation distance

Table 3.2: Properties of solar type III bursts according to Reid and Ratcliffe (2014).

Property	Observed value
Spectral index	≈1.7. This is the same value found for X-ray flares.
Source size	$\propto f^{-1}$, f [MHz] | 432 | 150 | 80 | 43 | 1 ; half width to e^{-1} brightness ['] | 2 | 4.5 | 11 | 20 | 300
Scattering	2' at 80 MHz broadening of a point source
Ratio f_H/f_F	1.6:1 to 2:1. $f_H/f_F < 2$ results from delayed emission near the plasma frequency and hence a refractive index of 1.
Polarization	average 0.35 (F), 0.11 (H), maximum 0.6 (F)

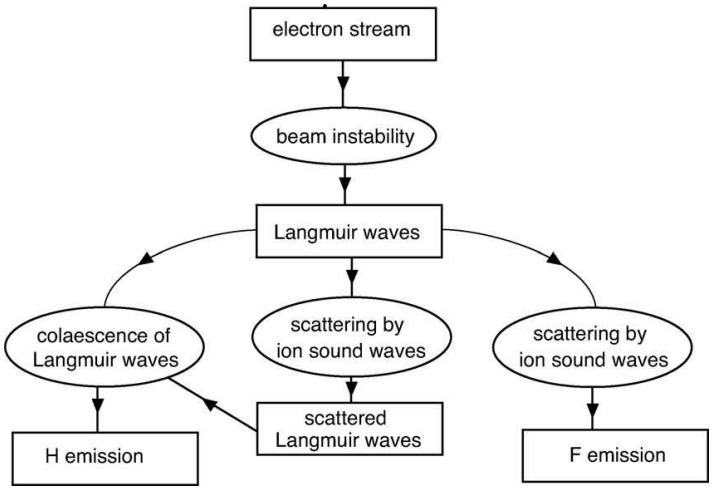

Figure 3.10: Production mechanisms of fundamental (F) and harmonic (H) plasma emission of solar type III bursts by electron beams in the corona. (Figure from Melrose, 2009).

of a few kilometers without additional processes. To resolve Sturrock's dilemma two modifications have been added to the theory. The first is the development of a beam-plasma structure of fast and slow electrons where the slower electrons absorb energy lost by the faster ones. The second is an inhomogeneous plasma density, that allows the plasma waves only in highly localized regions. Similarly other problems were discovered and often resolved (Melrose, 2009; Reid and Ratcliffe, 2014). They regard the source size with the presence of refraction, modeling the propagation with the known coronal densities, radio temperatures, etc.

3.3.4 Type IV Burst

Type IV bursts are flare related broadband continua (Fig. 3.7). One distinguishes between stationary and moving type IV bursts. The stationary type IV bursts follow major flares, show a variety of fine structure such as zebra patterns, pulsation and fiber bursts and can develop into type I storms. The moving type IV bursts are similar but show an additional frequency drift comparable to that of type III bursts (∼100 MHz/s) and similar source velocities of $0.3c$.

In addition to plasma emission also gyrosynchrotron emission can be responsible for their occurrence. In either case are the generating electrons confined by stationary or expanding coronal loops which can explain the long lifetimes.

3.3.5 Type V Burst

Type V bursts are continuum bursts of short duration (1-3 min) which are only observed with or after type III bursts and therefore are closely associated. Consequently they show many similar properties such as source height, polarization, peak fluxes.

They can be explained by plasma emission from electrons which left the electron beam of the type III burst for example because of pitch angel scattering.

3.4 Propagation of Radio Waves through the Corona

The propagation of a radio wave with the frequency f in a fully ionized plasma, as in the corona, is described by the index of refraction

$$n = \sqrt{1 - \frac{\omega_{\mathrm{pe}}^2}{\omega^2}} \tag{3.10}$$

with the angular plasma frequency ω_{pe} and $\omega = 2\pi f$ (Treumann and Baumjohann, 1997) leading to the dispersion relation

$$\omega = \sqrt{\omega_{\mathrm{pe}}^2 + h^2 c^2}. \tag{3.11}$$

The inspection of Eq. 3.10 and Eq. 3.11 provides that a radio wave can freely leave the corona if $f > \omega_{\mathrm{pe}}/2\pi$. The group velocity

$$v_g = \frac{\partial \omega}{\partial k} = c\sqrt{1 - \frac{\omega_{\mathrm{pe}}^2}{\omega^2}} \tag{3.12}$$

shows, that a radio wave propagates in a plasma with a velocity smaller than the velocity of light.

In the case of plasma emission, Langmuir waves are scattered at ion density fluctuations and/or coalesence with low frequency plasma waves. Both leads to escaping radio waves. Thus the frequency of the radio wave is given by $\omega = \omega_{\mathrm{pe}} + \omega_{\mathrm{LF}}$ where ω_{LF} is the frequency of the low frequency plasma wave. In a plasma with $\omega_{\mathrm{pe}}/\omega_{\mathrm{ce}} \gg 1$, the whistler waves with the frequency ω_{w} are the low frequency waves with the highest frequency, i.e. $\omega_w < \omega_{\mathrm{pe}}$. Whistler's resonance frequency is ω_{ce}, i.e. $\omega_w < \omega_{\mathrm{ce}} \ll \omega_{\mathrm{pe}}$ in the case of the corona.

Then in the case of fundamental emission, the group velocity is given by

$$v_{\mathrm{g}} < c\sqrt{1 - \frac{\omega_{\mathrm{pe}}^2}{\omega_{\mathrm{pe}}^2 + \omega_{\mathrm{ce}}^2}} \tag{3.13}$$

in the vicinity of the emission site. For $\omega_{\mathrm{pe}}/\omega_{\mathrm{ce}} \approx 15$ as a typical value in the corona, on gets $v_{\mathrm{g}} < 0.35c$. In the other case of harmonic emission, i.e. $\omega \approx \omega_{\mathrm{pe}}$, one has $v_{\mathrm{g}} < 0.87c$. The result shows that a radio wave of harmonic emission leaves the emission site faster than that of the fundamental emission. Hence, it is generally assumed that the radio wave of the harmonic emission is received first.

Chapter

4

Solar Observations with LOFAR

As discussed in the previous chapters, the Sun is an active star that exposes a wide variety of phenomena. Because of its proximity to Earth it provides a unique opportunity to study these phenomena of stellar activity in great detail. To observe its radio emission and in particular its nonthermal radio bursts radio telescopes have been developed. The first successful observations have been reported by Wild and McCready (1950) with a single antenna and dynamic radio spectra. Later first spatially resolved images of radio burst as localized radio sources in the corona were provided by early interferometers at Culgoora (Wild, 1970), Nancay (Bougeret et al., 1970) and Clark Lake (Kundu et al., 1983). However, their spatial, time and frequency resolution was limited.

With LOFAR (van Haarlem et al., 2013) a sensitive high resolution radio interferometer became available in June 2010 for radio observations at the low frequency end of the atmosphere's radio window. Its frequency range from 10 to 250 MHz can record radio emission from radio sources at a height between 0 and 2 solar radii in the corona. Its capability for high resolution dynamic imaging spectroscopy makes it particularly useful for spatial and time resolved observations of solar radio burst. The LOFAR Key Science Project "Solar Physics and Space Weather with LOFAR" (Solar KSP, Mann, Vocks, and Breitling, 2011) was founded to use LOFAR for solar observations and to address open questions. Its goals are the coordination of solar observations, the solar data processing and analysis and the provision of the resulting data products to the scientific community. These goals led to the development of the LOFAR Solar Imaging Pipeline and the LOFAR Solar Data Center (Breitling et al., 2015) described here.

4.1 LOFAR - The Low Frequency Array

The Low Frequency Array (LOFAR, van Haarlem et al., 2013) is a modern digital radio interferometer developed under the leadership of the Netherlands Institute for Radio Astronomy ASTRON. It consists of a total of 50 antenna stations distributed over Europe (Fig. 4.1) with 24 core and 14 remote stations in the Netherlands (Fig. 4.2) and 12 international stations in Germany (6), United Kingdom (1), France (1) and Sweden (1) and Poland (3). The longest baselines from Chilbolton to Baldy and Onsala to Nacay have a length of approximately 1700 km.

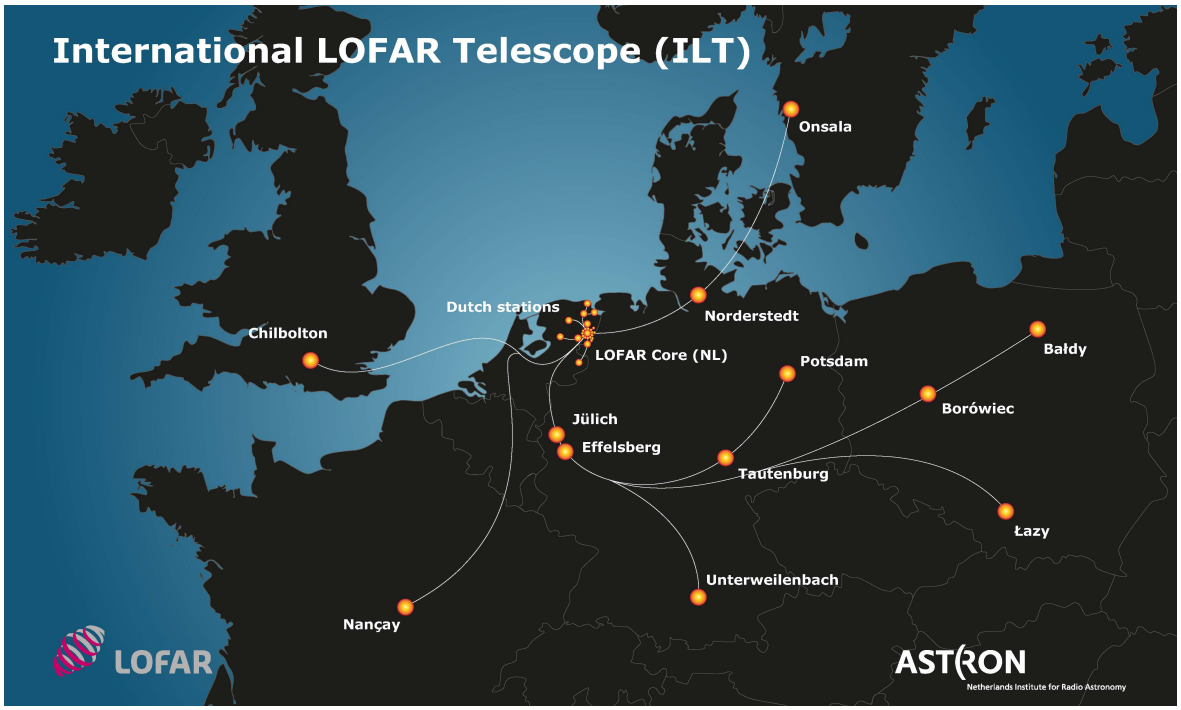

Figure 4.1: Map of all operational antenna stations forming LOFAR as of 2016.

An international LOFAR station consists of a high- and low-band antenna field and an electronics container for the receiver and computer hardware as shown in Fig. 4.3. One of these station (DE604) is located in Potsdam-Bornim and maintained by the Leibniz-Institut für Astrophysik Potsdam. There are also core and remote LOFAR stations, which differ in the antenna field configuration and their distance to the center of the array.

An antenna field is composed of identical antennas, whose signals are added up to a station beam (or pointing) to receive the signal from a specific sky direction. A low-band and high-band antenna is shown in Fig. 4.4 and 4.5 respectively. The data of the station pointings is sent to the correlator in Groningen which forms the array or sub-array pointings.

LOFAR operates in the low frequency range from $10 - 90$ (low-band) and $110 - 250$ MHz (high-band) in full polarization with high sensitivity and resolution for imaging spectroscopy. LOFAR's beam forming allows for the simultaneous observation of several different sky regions, which is important for the calibration of highly variable radio sources like the Sun. It also allows the simultaneous recording of dynamic radio spectra and images at different frequencies. These capabilities make LOFAR a very powerful instrument for imaging spectroscopy of celestial radio sources and to a radio heliograph if applied to the Sun.

4.2 Characteristics of solar observations

There are certain differences between solar and standard observations which have consequences for the data processing. They are summarized in Table 4.1 and 4.2 and explained below.

Figure 4.2: The most central LOFAR core stations in the Netherlands which are used for solar imaging observations. Each core station consists of one low- and two high-band antenna fields. The six stations on the island are called the Superterp.

4.2.1 High variability of solar radio emission

The radio emission from most radio sources that LOFAR observes such as galaxies is constant and ranges from 0.1 to 100 Jy. However, the emission from the Sun at 100 MHz is about 10^4 Jy (1 solar flux unit, sfu) during quiet periods but it can rise to 10^{12} Jy (10^8 sfu) within a few seconds in case of solar radio bursts (Dulk, 2000; Mann, 2010) which can occur anywhere near the Sun. So solar radio observations need to be able to record a dynamic range in brightness of 8 orders of magnitude with a time resolution of seconds. Consequences are:

Figure 4.3: International LOFAR station (DE604) in Potsdam-Bornim with the low- and high-band antenna fields to the left and right respectively. The container in the front right houses the receiver and computer electronics and the connection to the Internet.

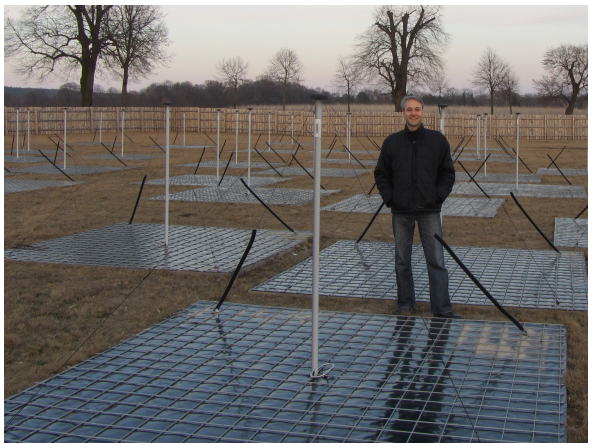

Figure 4.4: Low-band antenna.

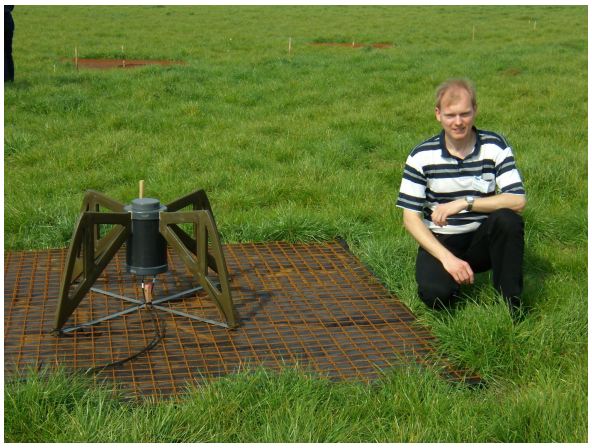

Figure 4.5: High-band antenna.

Table 4.1: Differences between observations of the Sun and standard radio sources.

	Standard radio source	Sun
Temporal resolution [s]	$\geq 10^4$	≤ 1
Spatial resolution [arcsec]	~ 1	$\sim 10^1$
No. of stations	≥ 48	≤ 30
No. of baselines	$> 10^3$	$< 5 \times 10^2$
Field of view [deg]	$> 10^1$	~ 1
Typical flux density [Jy]	$\ll 10^3$	$10^4 - 10^{12}$
Typical noise level [Jy]	10^{-1}	10^2
Dynamic range of flux density [orders of magnitude]	0	8
Ionospheric scintillation	low	high
High res. dynamic spectroscopy	no	yes

Table 4.2: Differences between standard and solar data processing resulting from the differences in the observations of Table 4.1.

	Standard Imaging	Solar Imaging
Aperture synthesis	yes	no
Flagging	in frequency & time	in frequency only
uv-range [wavelengths]	$0 - 10^6$	$0 - 10^3$
Sky model source threshold	≤ 50 Jy	$\sim 10^3$ Jy
Distance calibrator - target	≤ 1 deg	≥ 5 deg
Demixing	yes	no
Imager	AWImager	CASA imager
CLEAN algorithms	Clark for point sources	multi-scale for ext. sources
Self-calibration	yes	limited to selected events
Data analysis	from images	Solar Data Center

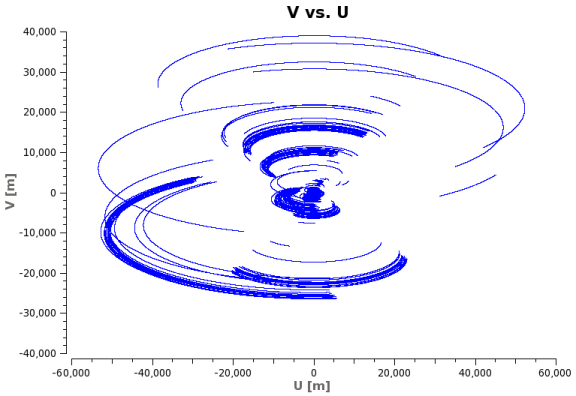

Figure 4.6: uv-coverage (baselines) for 12 hours of data. Because of the Earth's rotation each point in the uv-plane multiplies into an arc like point set.

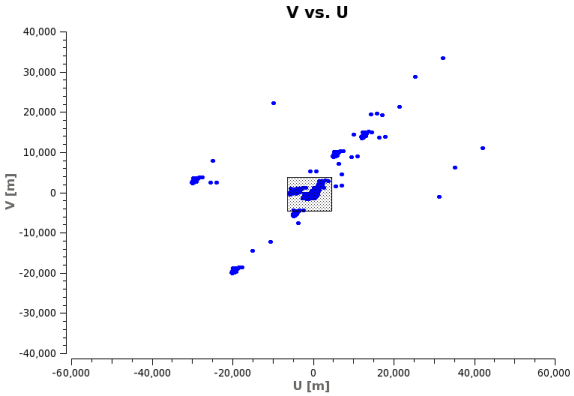

Figure 4.7: uv-coverage for 1 second of data. The box indicates the approximate region of points (baselines) that remain if the uv-range is limited to ≤ 1000 wavelengths.

- A time resolution of seconds prevents the typical aperture synthesis which uses the Earth's rotation and observation times of hours for increasing the uv-coverage and image quality. Fig. 4.6 and 4.7 show the uv-coverage with and without aperture synthesis for comparison. Each point in the uv-plane represent a baseline.

- The short duration of some bursts prevents temporal radio frequency interference (RFI) removal also called flagging, since flagging of radio peaks could also remove the signals of solar bursts.

- Dynamic radio spectra are recorded simultaneously with the imaging data, since they can provide a higher time and frequency resolution at a lower data rate. They also support the identification of solar bursts in LOFAR data.

4.2.2 Limited resolution in the corona

While standard targets can be resolved with sub-arcsec resolution, the spatial resolution of solar observations is limited to a few ten arcsec by turbulence in the corona (Bastian, 2004). This turbulence causes inhomogenities in coronal plasma and electron number density N_e and consequently in the plasma frequency $f_{pe}(N_\mathrm{e})$ (Eq. 3.9) and the index of refraction $n = (1 - f_{pe}^2/f^2)^{1/2}$ at an observation frequency f. Consequences are:

- Since the angular resolution is proportional to the inverse of the baseline length, the uv-range can be limited to a maximum baseline length of 1000 wavelengths. The box in Fig. 4.7 marks the approximate subset of stations that remains with this limitation.

- International stations and some remote stations are not needed for imaging since they provide only baselines with a length of more than 1000 wavelengths. This reduces the number of baselines $n_b = n_s \times (n_s - 1)/2$ (where n_s is the number of stations) and therefore limits the image resolution.

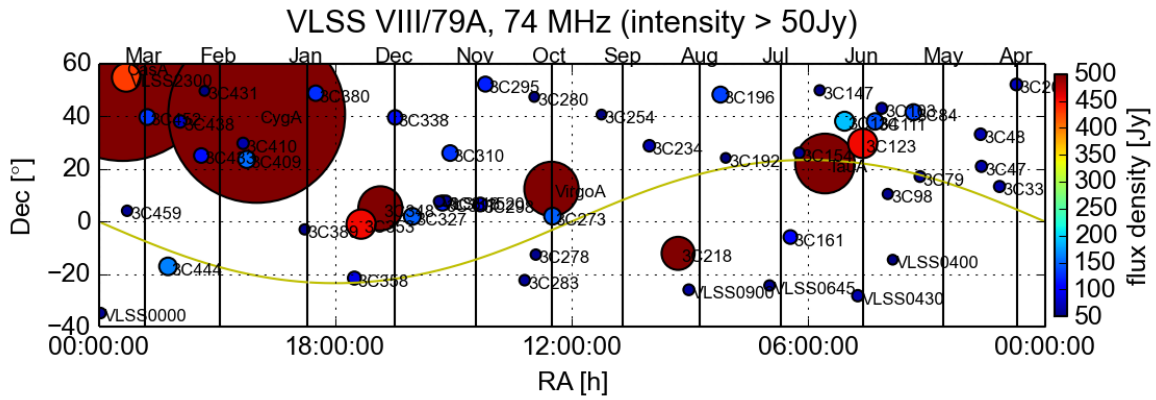

Figure 4.8: Sky map of intense radio sources and their location with respect to the Sun. The yellow line shows the path of the Sun during one year. The area of each source represents its flux density. A compact source with a high flux density and a distance of a few 10 degrees is best suited for the calibration of solar data.

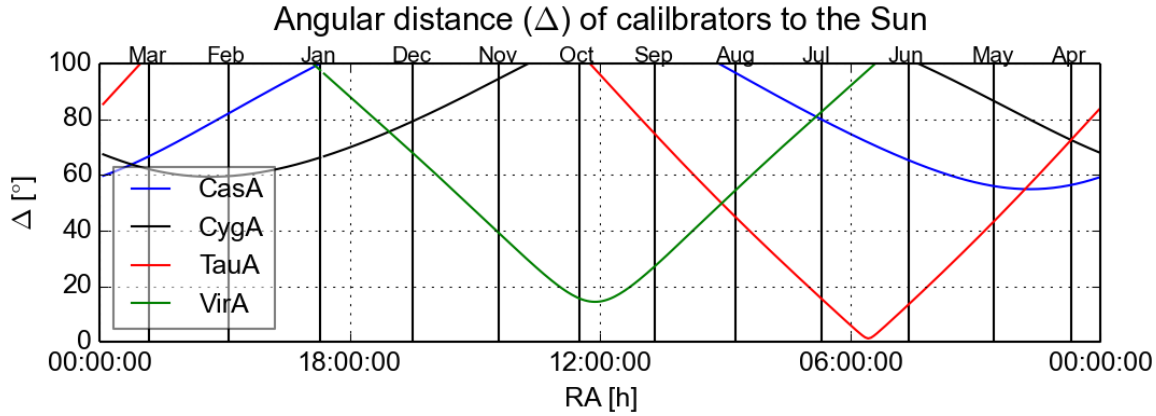

Figure 4.9: Angular distance (Δ) of calibrator sources for solar LOFAR data to the Sun within one year.

4.2.3 Sufficient field of view

Since solar radio emission is a result of plasma emission determined by the plasma density of the corona, radio emission in the frequency range from 10 to 240 MHz is limited to a region within about $3R_\odot$. This region is well contained with the LOFAR field of view of approximately 5 degrees. The consequence is:

- A field of view of $3R_\odot$ does not require the corrections provided by the AWImager (Tasse et al., 2013) and so the CASA imager can be used as well. This was an advantage during LOFAR's commissioning phase when the AWImager was not available and it is necessary for functionality that is not available through AWImager.

4.2.4 High flux density of solar radio emission

Another difference exists with the radio sources that can be used for calibration. For many sky regions detailed sky models exist with a resolution of a few Jy which the

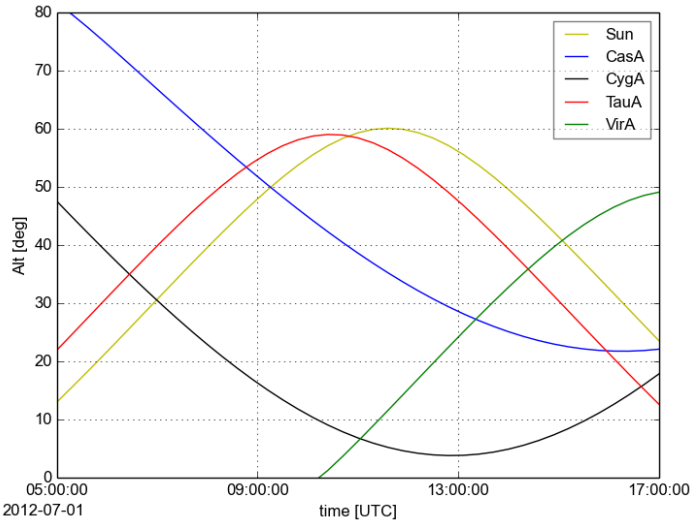

Figure 4.10: Daily variation of the altitude of solar calibrators. Low altitude observations provide data of lower quality which are also harder to calibrate. The LSDC (Section 4.4) provides these plots for every day of the year to support the scheduling of observations.

Sun passes during a year. But since the Sun emits a flux density of 10^4 Jy or orders of magnitudes more its radiation dominates the signal from these sky regions and it is picked up through LOFAR's side lobes. Consequences are:

- Generally radio sources in the field of view are not sufficient for the calibration of solar observations. Additionally strong radio sources are needed. These sources are Cassiopeia A, Cygnus A, Taurus A and Virgo A. Fig. 4.8 shows the position of the Sun during each year and the strongest radio sources at 74 MHz. The intensity of the radio sources is represented by their area. Fig. 4.8 helps to see which calibrators are close to the Sun during what time of the year. Then solar observations are always done with two sub-array pointings. One is directed at the Sun and the other at a suitable calibrator source. This way the calibration coefficients can be obtained from the calibrator data and then applied to the data from the Sun. However, this adds additional constraints for the observation. First the angular distance between the Sun and the calibrator may neither be too small (< 5 deg) nor too large (> 50 deg), since otherwise the calibrator will be perturbed by the Sun or the calibration will be perturbed by an imperfect beam model, respectively. Fig. 4.9 shows the distance (Δ) of the calibrators to the Sun versus time. Second the Sun and the calibrator need to be observed at sufficiently high altitude angles (> 20 deg) since otherwise their radio emission is too much perturbed by the ionosphere. This condition also excludes observations during winter months from November to February. Fig. 4.10 shows the altitudes which have to be taken into account for an observation on July 1 for example.

- Similar to the emission from the Sun also the emission from the calibrators effects the solar data. Therefore its influence should be removed by demixing. Demixing is a method in which the contribution from certain radio sources is modeled and subtracted from the data. Unfortunately, demixing often does not work well without a model for the radio emission from the Sun which is not available at pre-processing, when demixing is applied for standard imaging. So demixing is not yet part of solar imaging and therefore artifacts from strong radio sources are not yet removed. A simulation of these artifacts for March 9 is shown in Fig. 4.13.

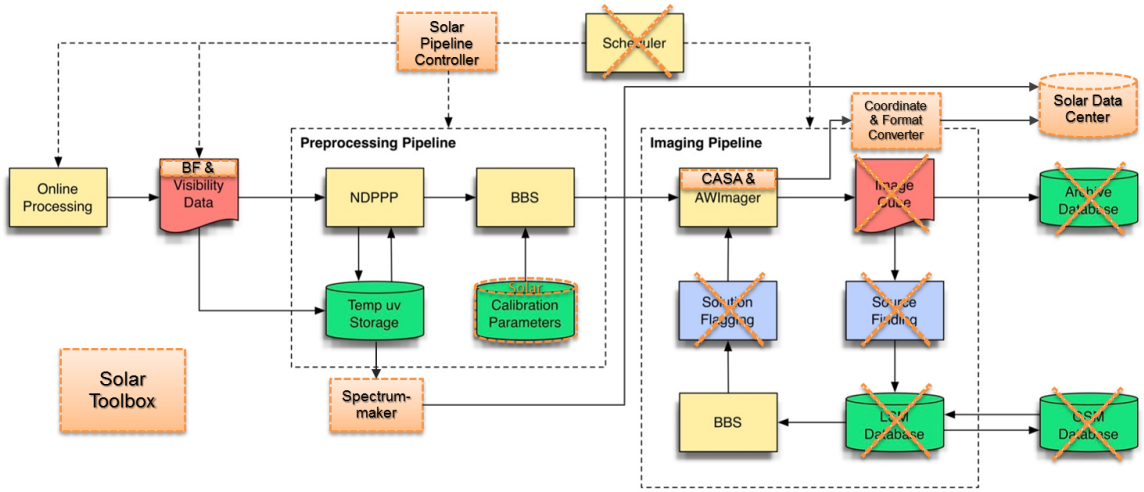

Figure 4.11: Flowchart of the Standard Imaging Pipeline and the modifications (orange) that lead to the Solar Imaging Pipeline. The data flow starts with the online processing and ends at the Solar Data Center. The crossed out components are not needed for solar imaging. Details of the individual components are described in the text.

4.2.5 Observations during day time

LOFAR solar observations have to be done during daytime, preferably at noon. At noon ionospheric scintillation also reach their maximum. The consequence is:

- Ionospheric scintillation causes different phase delays for different atmospheric regions the radio signals pass on their way to different LOFAR stations. This leads to calibration and imaging errors, more severely during day time than during night time. This is also another reason for a lower image quality of solar observations than of other observations which are usually taken during night time.

4.3 The Solar Imaging Pipeline

The Solar Imaging Pipeline is a software package for processing and analyzing LOFAR observations of the Sun. It was developed by the Solar KSP at the Leibniz-Institut für Astrophysik Potsdam (AIP) as an extension of the LOFAR Standard Imaging Pipeline (Heald et al., 2011) to accomplish a proper data processing according to the above criteria. The outline is shown in Fig. 4.11. It shows the data flow and in orange color the modifications from the Standard Imaging Pipeline. The individual steps and components are discussed below.

4.3.1 Online processing

The LOFAR data from all stations is correlated at a computer cluster in Groningen. This correlates the data in real-time and stores it at a temporary storage for a later processing. Currently either low or high-band antenna data is recorded at several equidistant frequencies. Each of these frequency subbands has a bandwidth of 195 kHz and a subdivision into 64 channels. During solar observations also beam-formed data

for dynamic spectroscopy is recorded in addition to visibility data which is used for standard imaging.

4.3.2 Temporary storage and data formats

The immediate processing of the data as shown in Fig. 4.11 is not yet realized but a planned processing option for the future. Instead the data is currently sent to a temporary storage. The imaging and spectroscopic data is recorded in CASA Measurement Sets (MS, McMullin et al. (2007)) and LOFAR's beam-formed format (Stappers et al., 2011) with an HDF5 container (The HDF Group, 1997–2014) respectively. An MS contains the data of only one subband. The raw data rate scales with the number of channels recorded and is roughly 30 times larger than data with a single channel average. The typical size for the latter is about 1 GB for 10 hours of data with time resolution of 1s. The corresponding JPEG images and thumbnails have about the same size, while the FITS images need about three times as much. The size of beam-formed data scales with the time resolution and number of channels. It is similar to the size of one MS while providing a higher resolution. In summary a typical solar observation of a few hours produces a few TB of data.

4.3.3 New Default Pre-Processing Pipeline (NDPPP)

The first step in the pre-processing of imaging data is done with the New Default Pre-Processing Pipeline (NDPPP). This includes flagging of the channels of the calibrator data for RFI with the AOFlagger (Offringa et al., 2013). The Sun data are not flagged, to preserve all variable radio features. Subsequently, the channels (excluding edge channel) of all subbands are averaged to one channel per subband to reduce the amount of data significantly. Also the uv-range is limited to 0-1000 wavelengths to exclude data that exceeds the resolution limits of the corona and therefore is not useful for the calibration and the imaging. This also reduces the amount of data and consequently the processing time.

4.3.4 BlackBoard Selfcal (BBS)

The second step of the pre-processing is the calibration with LOFAR's BlackBoard Selfcal (BBS) system. Here amplitude and phase corrections are determined for every 30 seconds of calibrator data using a calibrator sky model. This sky model only contains the calibrator either modeled by a two-dimensional Gaussian or by its clean components. However, a simple Gaussian model is sufficient, since the calibration quality is limited by the angular separation between Sun and calibrator. The solutions are then transferred to the data from the Sun. Alternatively also two Gaussian sky models of the Sun for low- and high-bands have been developed which can be used for direct calibration of the data from the Sun. However this calibration is less accurate because of the extension of the model only short baselines can be calibrated. Also the determination of the astrometric position is limited to a few arcmin because of the asymmetric variability of the corona.

4.3.5 Solar calibration parameters

BBS is controlled through certain configuration parameters. The specific parameters for the Sun are derived from the standard imaging parameters and are included in the Solar Imaging Pipeline. They are optimized for the calibration of strong calibrator sources and a transfer of the calibration coefficients to the solar data.

4.3.6 Imaging

After the calibration the corrected data is imaged with the multi-scale CLEAN algorithm provided by CASA (McMullin et al., 2007). The final image is then transformed from equatorial to solar coordinates where the Sun is centered and the Sun's north pole is oriented upwards. This is done for every time step and frequency. Alternatively the CASA imager can be replaced by the AWImager. The AWImager provides additional correction by the w- and A-projection. The former projection removes the effects of non co-planar baselines in large fields. The latter takes into account a varying primary beam during synthesis observations. However, both corrections are not necessary for the small field of view used in solar observations.

With the CASA imager also images from multiple integration steps can be combined. This so-called aperture synthesis virtually increases the number of baselines by combining data from different times where the antenna positions have shifted because of the Earth's rotation. Aperture synthesis for the Sun is complicated since its celestial coordinates change by about one degree per day while imaging is usually done for fixed celestial coordinates. Therefore the aperture synthesis was extended for sources with changing celestial coordinates. It can be activated via the "movingsource" option of the CASA imager. With the key word "SUN" every time step of an observation is shifted such that the position of the Sun remains fixed. This avoids smearing of the Sun during longer observations periods of hours.

4.3.7 Self-calibration

Optionally an additional phase-only self-calibration can be applied to selected images. In the Standard Imaging Pipeline a source finding algorithm is applied to the image to find sources not contained in the sky model. These are then added to the sky model and applied in a new calibration. For solar observations a simplified method is used which directly uses the cleaned images as model. Since it does not require assumptions about the sources to find, it is useful where little is known about the radio source morphology. Then imaging is repeated resulting in a reduced noise and increased source brightness. Further self-calibration cycles can be repeated if needed until no further improvement is achieved. This is usually the case after one or two cycles. Similarly the first solar LOFAR images of a type I burst have been obtained by Vocks, Mann, and Breitling (2016).

4.3.8 Simulation of images

With BBS the Solar Imaging Pipeline also produces simulated reference images for the LOFAR array configuration and the position of radio sources for a particular time of observation. One of these simulations is an image of a Gaussian model of the Sun

shown in Fig. 4.12. Another simulation in Fig. 4.13 shows the contribution through side-lobes from the strongest four radio sources at the LOFAR frequency range: Cygnus A, Cassiopeia A, Taurus A and Virgo A. The simulation also includes an image of the point spread function (PSF) shown in Fig. 4.14. These simulated images are useful for evaluating the calibration quality and its limitations. The simulated images are accessible through the LOFAR Solar Data Center described in section 4.4.

4.3.9 Solar Pipeline controller

The pipeline controller replaces the scheduler of the Standard Imaging Pipeline. It controls which processing steps are applied to the data. Earlier it was also responsible for the data management, which included the distribution of data to the LOFAR processing cluster and its collection. With newer clusters central file systems and job schedulers became available and are used.

4.3.10 Solar toolbox

The solar toolbox contains further programs for various tasks related to the data processing. This includes calculations of solar coordinates and angles, image format conversion, extraction of specific observation periods, job and disk space monitoring, the correction of pointing positions and many other tasks.

4.3.11 Dynamic spectra

The Solar Imaging Pipeline also provides the spectrum maker for processing beam-formed data. At first all channels are divided by an estimate of their decile. Then channels close to the edge of a subband are excluded since they contain data of lower quality. Also channels with a high standard deviation are identified and excluded which are likely to be caused by RFI. The default limit for excluding channels is a standard deviation exceeding 0.5 of the channels decile value. If less than 6 channels fulfill this criterion the limit is increased until at least 6 channels remain. The remaining channel values of each subband are averaged to values a and scaled to values s between 0 and 1 according to $s = (a - a_{\min})/(a_{\max} - a_{\min})$. Here $a_{\min}$ is the minimum value of a excluding 0. $a_{\max}$ is the maximum value of a excluding the highest 1% to make the scaling more robust against spikes from RFI. To emphasize radio burst signatures the values v are gamma corrected according to the function $f(v) = v^{\gamma}$. Intermediate values between the different subbands are usually interpolated to mimic the smooth transition between subbands. But interpolation can also be disabled if a representation of the width of individual subbands and the actually recorded data is preferred.

4.4 The LOFAR Solar Data Center

The LOFAR Solar Data Center (LSDC) is the archive for LOFAR data products of the Solar KSP. Its software is part of the Solar Imaging Pipeline and it is located and operated at the AIP. It provides a web user interface at `http://lsdc.aip.de/` to share LOFAR solar observations with the solar science community. It was designed for browsing through available data, for finding specific observations and for presenting

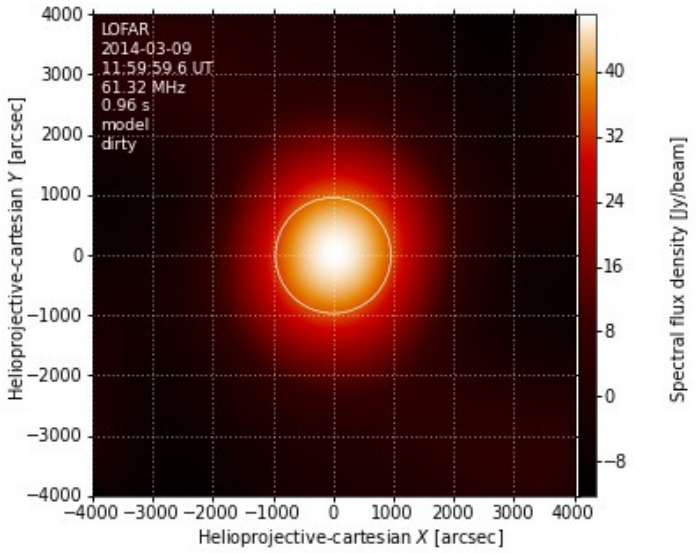

Figure 4.12: Simulated radio image of a two-dimensional Gaussian model of the Sun for the LOFAR array configuration for an observation on March 9, 2014.

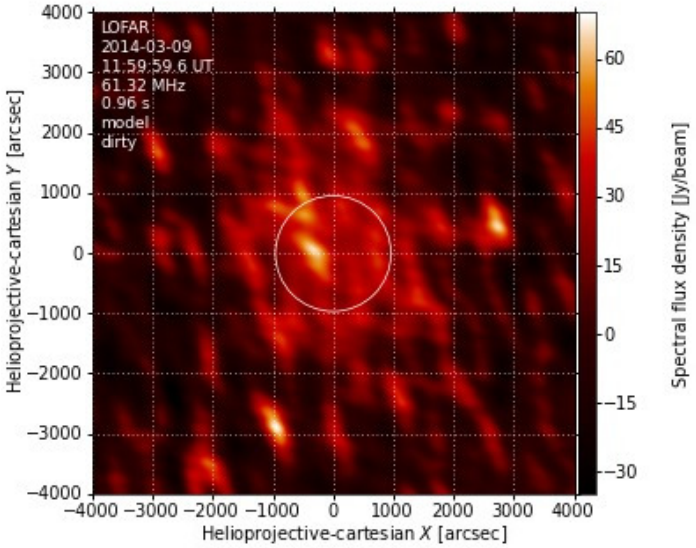

Figure 4.13: Simulated radio image of the model in Fig. 4.12 with additional contributions from the four strong radio sources Cygnus A, Cassiopeia A, Taurus A and Virgo A through side-lobes for the array configuration on March 9, 2014.

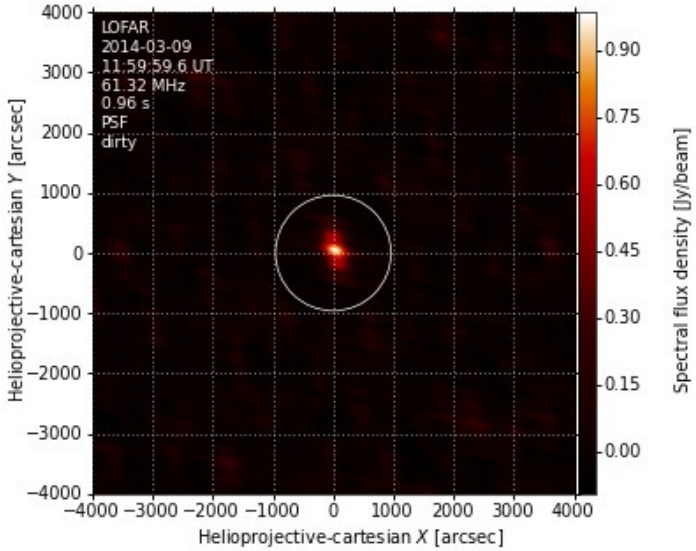

Figure 4.14: Simulated radio image of the PFS of the LOFAR array configuration for an observation on March 9, 2014.

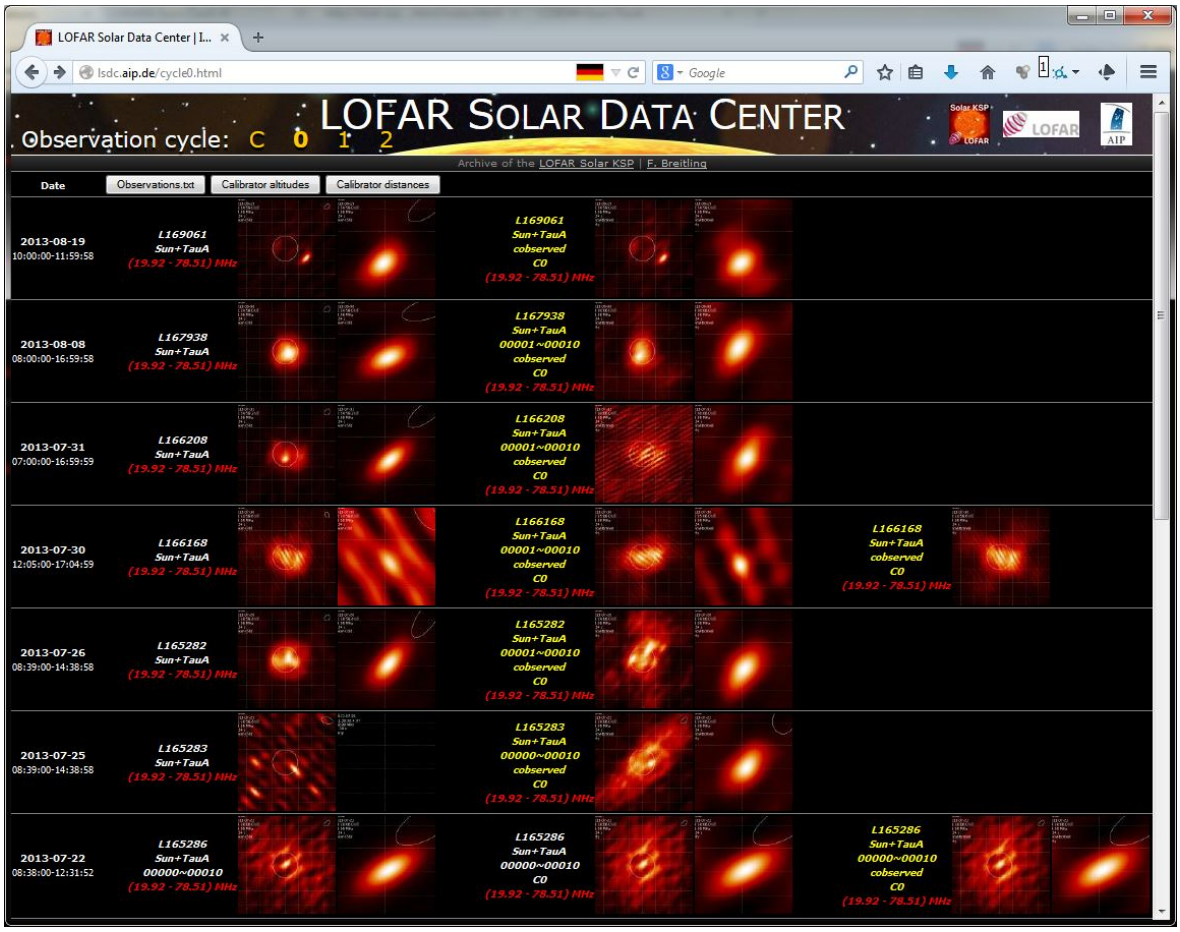

Figure 4.15: Main page of the LOFAR Solar Data Center showing data from observations cycle 0. The available observations are listed chronologically line by line and linked to their corresponding observation page.

the data products in a way that supports the identification of solar events and their interpretation. To serve this purpose the LSDC is structured as follows.

4.4.1 Main page

The LSDC is entered through the main page shown in Fig. 4.15. It shows a header with the title, icons and a menu at the left for switching between different observation cycles to be displayed in the main section of the page. Currently available options are `C` for the commissioning cycle and `0` to `2` for the regular operation cycles. Here cycle 0 is selected for the further discussion. The main section starts with a row of three buttons: observations.txt, calibrator altitudes, calibrator distances. They link to the list of available observations and to plots of the altitudes of the solar calibration sources (Fig. 4.10) and their distances to the Sun (Fig. 4.9). The plots provide useful information for selecting calibrators for observations and the data processing. Next a chronological table follows with the available data of the observation cycle. Each row represents one observation and its available data products. It starts with the observation date including start and end time followed by the results from different processing strategies. Each result contains information about the observation ID which is assigned automatically during scheduling of the observation, the target and calibrator source,

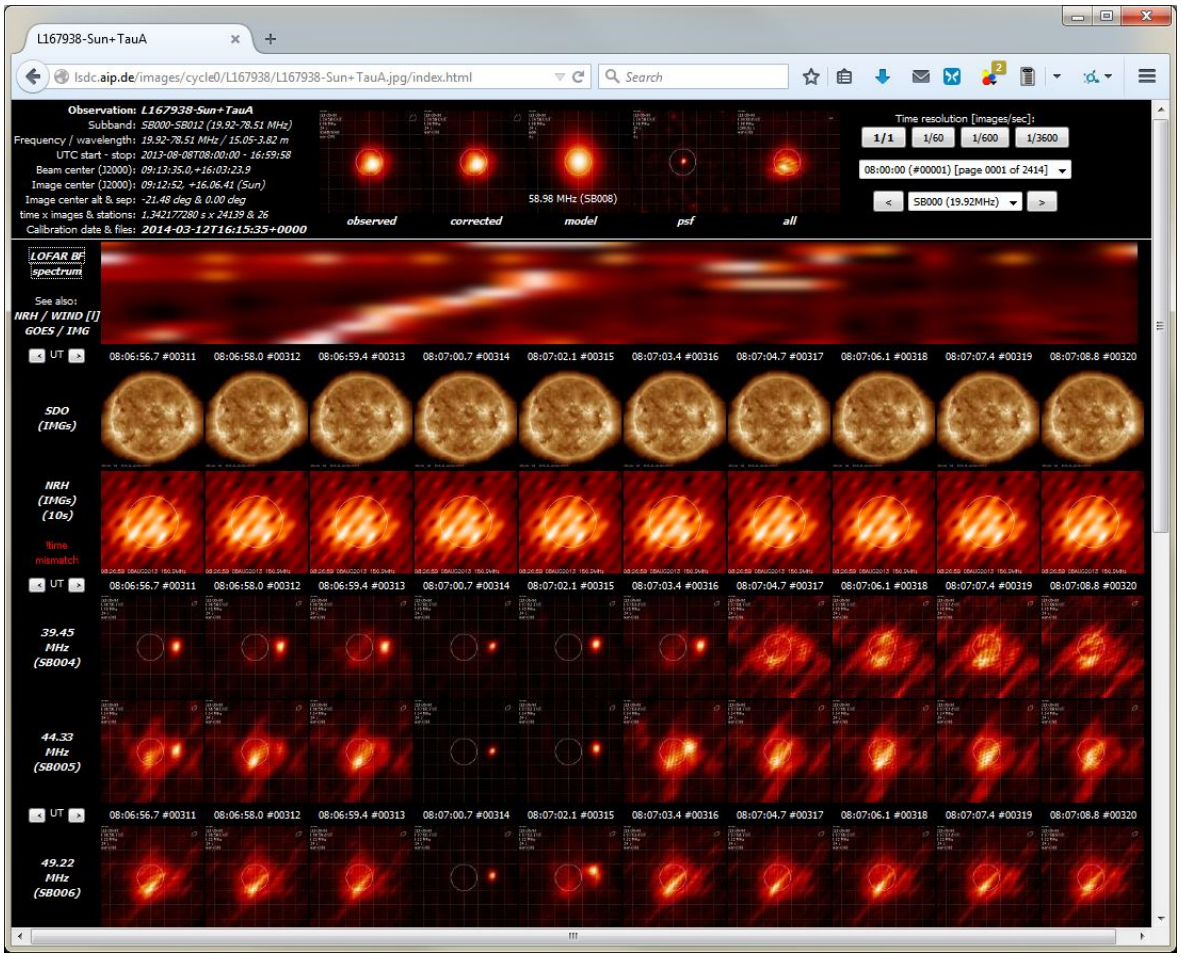

Figure 4.16: LSDC page of observation L206894 providing observation details, diagnostic images and a navigation box in the first row. Spectra, images from other instruments and images of the individual subbands follow. All images are previews that are linked to their full resolution version. A solar type III burst is visible in the dynamic radio spectrum at 08:06:58 to 08:07:02 UTC. and in the corresponding images.

possible additional information regarding the calibration and cleaning parameters, the observation frequency and a preview images of the Sun and the calibrator. Each image links to the corresponding observation page with all related data products.

4.4.2 Observation page

The observation pages provide access to the available data products for viewing and downloading. It also provides a control box to browse through them. An example is Fig. 4.16 which represents observation L206894. It is organized in rows, each showing the image sequence of a subband. However the first four rows are different:

1. The first row starts with a summary of observation specifications and a link to configuration and logfiles from the processing. The following five diagnostic images give an idea about the data and calibration quality. They show the un-calibrated data, the calibrated data, a simulated model and the point spread function (PSF) for the time step at the middle of the observation. The fifth image is integrated over the complete observation period. The row ends with the control box for

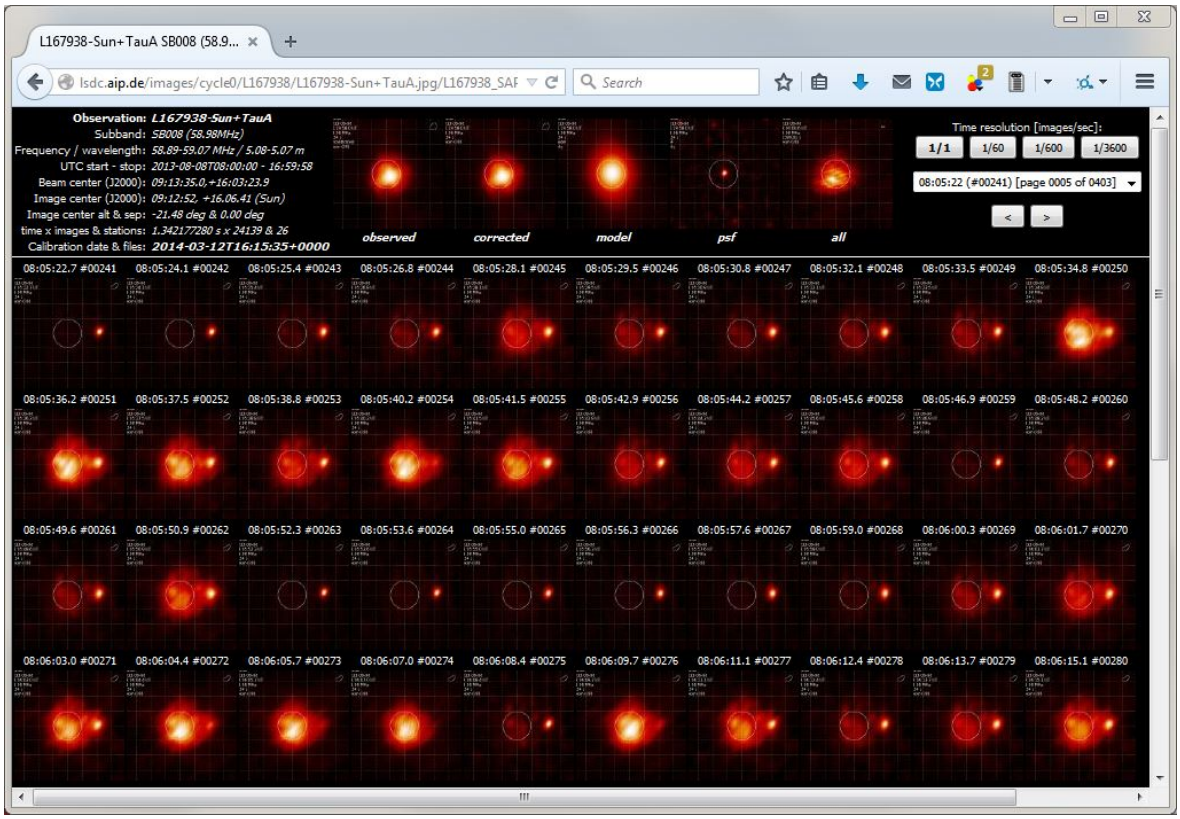

Figure 4.17: The page of subband 180 (65 MHz) of observation L206894. It can show longer periods of a single subband than the observation page. Here the sudden brightening within seconds in the north east reveals a type III burst. The first row is very similar to the first row of the observation page and has the same functionality.

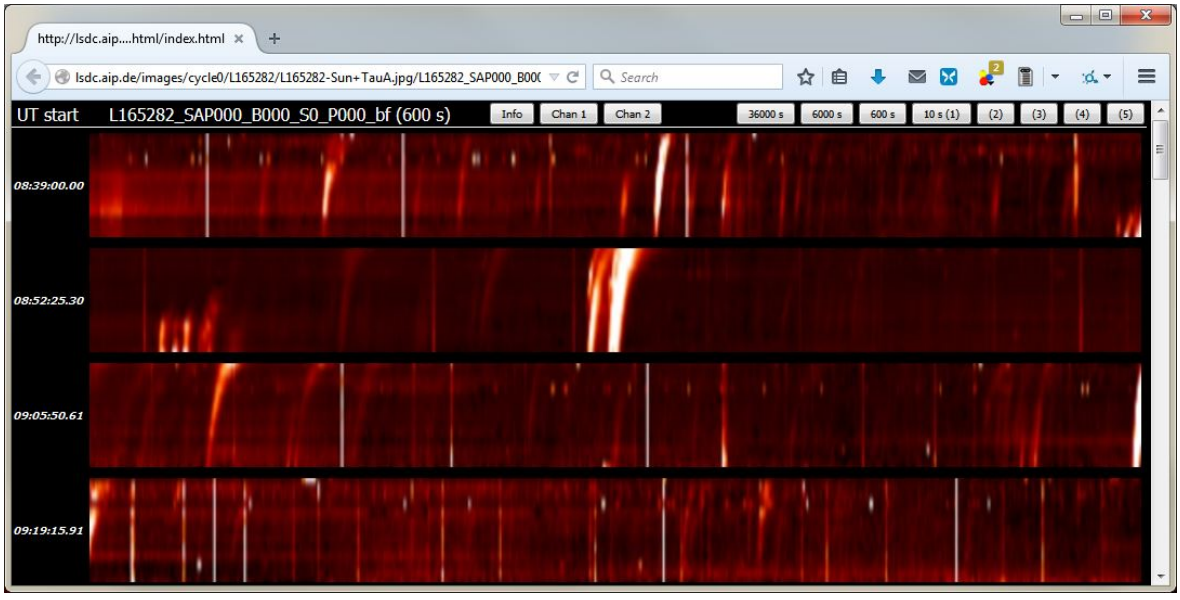

Figure 4.18: The dynamic spectrum page shows the sequence of LOFAR dynamic spectra from top to bottom. It is useful to identify solar events such as solar radio bursts, which are clearly visible as drifting broadband peaks. The top row provides further information and functionality explained in the text.

browsing through the data. It starts with four buttons to select different time resolutions that shows every first, 60th, 600th and 3600th image. The drop-down menu in the next line lets the user jump directly to a specific time range. The arrow buttons in the line below steps back or forward in time. The last drop-down menu in this last line opens the page of a selected subband in a new window.

2. The second row shows the dynamic radio spectrum by LOFAR. It also provides links to dynamic spectra from the Nançay Decameter Array (Lecacheux, 2000), the WIND satellite (Bougeret et al., 1995) and the Geostationary Operational Environmental Satellites (GOES).

3. The third row serves as a time axis showing the image numbers and recording times. It also contains navigation buttons to step one page back or forward. It repeats after every two image rows.

4. The fourth row shows extreme ultraviolet images of the lower corona from the AIA instrument (Lemen et al., 2012) of the SDO satellite with a time resolution of minutes.

5. The fifth row shows the images from the Nançay Radio Heliograph (Kerdraon and Delouis, 1997) at 151 MHz with an exposure time of 10 s. The time stamp marks the start of the exposure time.

6. The sixth row shows the same time axis as the third row.

7. From the seventh row on the LOFAR images from the different subbands follow with increasing frequency.

The images are only previews linked to the full resolution images. The page also contains links to the individual subband pages and to the dynamic spectrum page.

4.4.3 Subband page

The subband page shows images of a single subband and so can display a longer image sequence. This is useful for studying the temporal evolution of a solar radio event over a longer period. Fig. 4.17 shows subband 180 (65 MHz) of observation L206894 as an example. The first row is very similar to the first row of the observation page and provides the same functionality.

4.4.4 Dynamic spectrum page

The dynamic spectrum page is shown in Fig. 4.18. Its purpose is to display the LOFAR dynamic spectra next to each other to cover a long time range. This arrangement is useful for identifying solar radio bursts. Each row continues the time range covered by the previous row. Each spectrum is only a preview and links to its full resolution version. The first row shows the observation id and buttons with additional functionality. One provides further information about the observation settings, two others show RFI (Fig. 4.19 and 4.20), some can change the time resolution of the spectra and others can select pages of a certain time range.

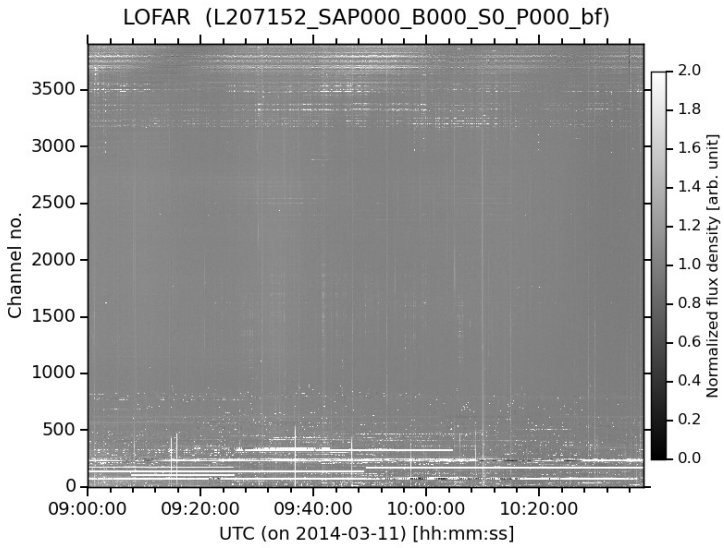

Figure 4.19: Dynamic spectrum of the channels of LOFAR beam-formed data. This plot shows at which times channels are disturbed by RFI. For example a significant disturbance by RFI is found at the first channels from 0 – 500. It appears for certain periods during the observation. Also time dependent systematic effects could be detected. Since this plot is not normalized it shows the antenna sensitivity reaching its maximum at a channel number of about 2300.

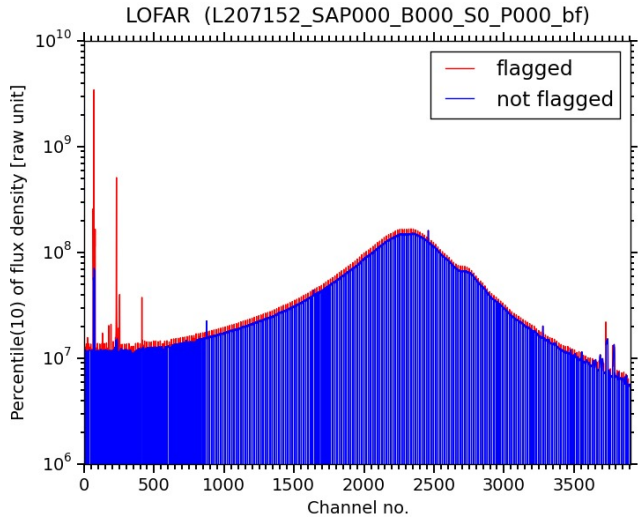

Figure 4.20: 10th percentile (decile) of the intensity (Stokes I) of each channel of LOFAR beam formed data. Channels with standard deviations greater than 0.5 of these decile values are printed red. Those channels are flagged as disturbed by RFI and are been removed from LOFAR dynamic spectra. Also channels close to the edge of a subband are flagged and removed. The remaining channels (blue) are used in the LOFAR dynamic spectrum.

4.5 Summary

LOFAR is a new radio interferometer for dynamic imaging spectroscopy that can be used for observations of the Sun. Solar observations are managed by the LOFAR Key Science Project “Solar Physics and Space Weather with LOFAR”, which has developed the Solar Imaging Pipeline and the Solar Data Center for processing the LOFAR data and providing access to the data product by the solar physics community. The Solar Imaging Pipeline builds upon the Standard Imaging Pipeline and differs in several ways as required by solar radio observations. It provides access to processed data from solar observations through the LOFAR Solar Data Center. LOFAR spectra and images of the Sun have been compared with other observations by other instruments such as the Nançay Radio Heliograph and the Nançay Decameter Array (Lecacheux, 2000) and good agreement has been found. The successful verification permits the usage of solar LOFAR observations for scientific studies.

Chapter

5

Electron Propagation from Dynamic Radio Spectra and Density Models

In many situations only dynamic radio spectra are available, since images are generally more difficult to obtain as they require more complex and extended instrumentation such as radio interferometer arrays. Therefore radio observations by a single satellites like Wind are limited to spectroscopy. Also LOFAR obtains more solar spectroscopic than imaging observations because dynamic spectra can already be provide by one LOFAR station which is more often available than at least 24 LOFAR core stations required for solar imaging. An example of a LOFAR spectrum without images of a type III burst on March 16, 2016 at 6:37:30 UTC is shown in Fig. 5.1.

Nevertheless, it is also possible to derive the radial distance and propagation velocity of radio bursts from the Sun from dynamic radio spectra using the relation between plasma emission and electron number density in the corona (Section 3.3). Some radio bursts propagate from the corona far into interplanetary space and can then be seen over a wide frequency range by a number of instruments such as LOFAR, URAN-2 (Fig. 5.2) and the Wind satellite (Fig. 5.3) for example. To calculate the propagation velocity of a radio burst over such a long distance an appropriate density model is required for the region from $1\,R_\odot$ to 1 AU (here $1\,R_\odot$ refers to the bottom of the corona excluding the photo- and chromosphere). The density of the corona within $2\,R_\odot$ was measured for example by Newkirk (1961) and from 0.3 to 1 AU by Schwenn (1990) with the HELIOS satellite. However, the density model by Newkirk (1961) $N(r) = N_\odot \times 10^{4.32 R_\odot / r}$ corresponds to a barometric height formula. Therefore it is only valid for a static atmosphere found close to the Sun but not at the LOFAR observation distance between 1.5 to $3\,R_\odot$ where the solar wind starts streaming away (Fig. 5.4). This region is particularly interesting because precise measurements of the solar wind density in this region are not available. However a model is needed that connects both available measurements so that it can be applied to dynamic radio spectra of LOFAR and other instruments. Mann et al. (1999) has developed such a density model but for a higher coronal density (Fig. 5.4). Here a new density model will be presented that fits the densities and temperatures in the corona and near Earth observed by Newkirk (1961) and Schwenn (1990).

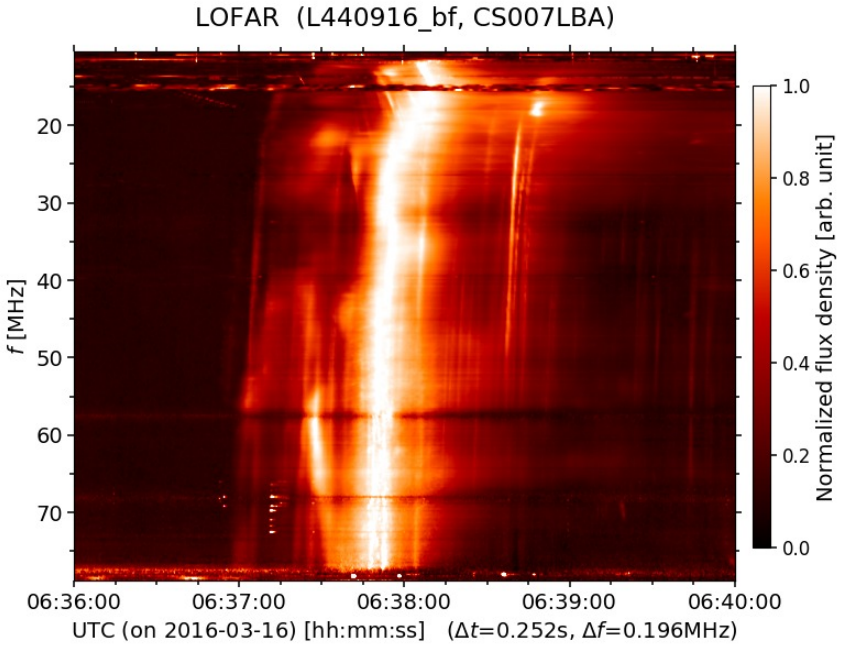

Figure 5.1: LOFAR spectrum of a type III bursts on March 16, 2016 that propagated far into interplanetary space and has also been seen by URAN-2 and Wind.

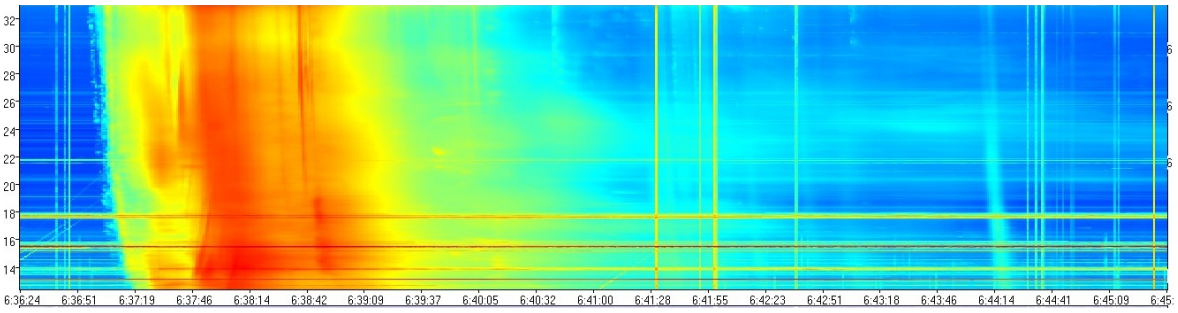

Figure 5.2: URAN-2 spectrum of the type III bursts on March 16 provided by V. Melnik.

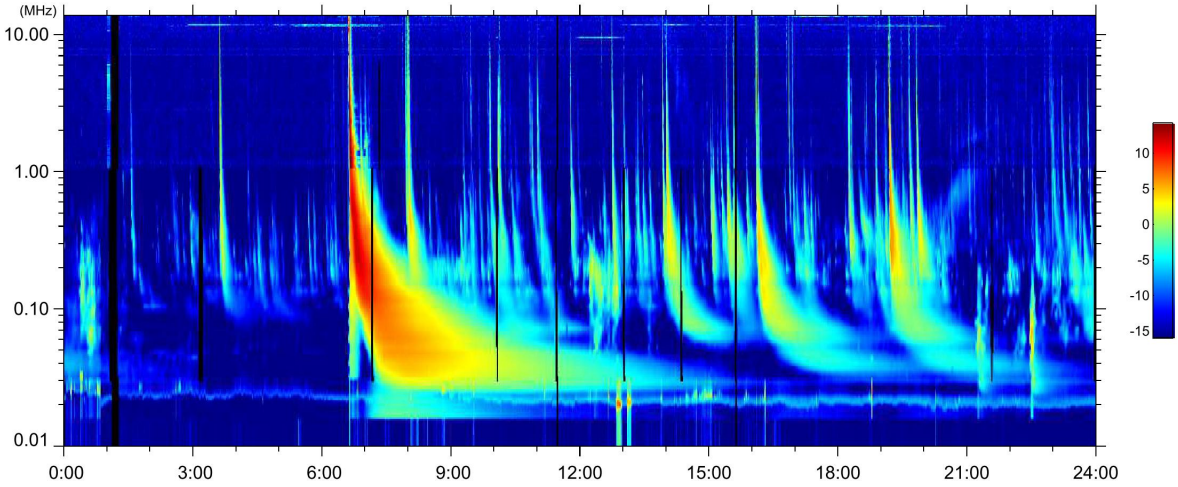

Figure 5.3: Wind satellite spectrum of the type III bursts on March 16, 2016 obtained from `https://stereo-ssc.nascom.nasa.gov/browse/2016/03/16/insitu.shtml`.

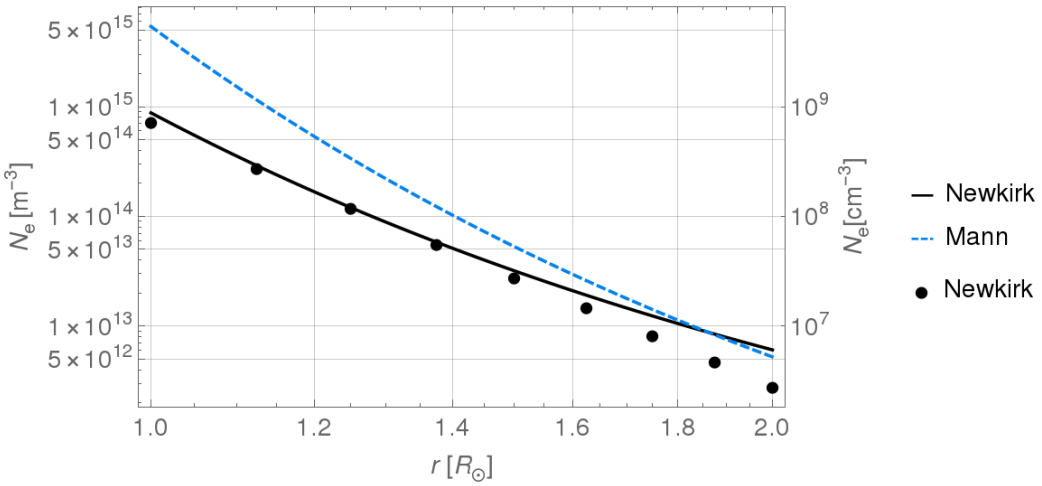

Figure 5.4: Electron density in the corona as measured by Newkirk (1961) (points) and the corresponding density model $N(r) = N_\odot \times 10^{4.32 R_\odot / r}$ (solid line). Also the model by Mann et al. (1999) is shown. The latter fits better to the observations at the LOFAR observation range at a distance greater than $1.8\,R_\odot$. However the density is a factor of two higher.

5.1 Earlier Density Models

A review of the historical development of spherical symmetric coronal density models is given by Priest (1982, Chapter 12), which is summarized here.

Chapman and Zirin (1957) calculated parameters of a static solar atmosphere with heat conduction. It predicts temperatures of 10^5 K near Earth which corresponds to the observed values. However, it also predicts higher than observed interstellar pressure and temperature near Earth and infinitely high densities at great distance.

Parker (1958) noticed these inconsistencies with observations and concluded that the Sun cannot have a static atmosphere but rather a certain amount of material steadily streaming away from it. This solar wind was soon confirmed in 1959 by the satellites Lunik III and Venus I. Parker calculated the flow of the solar from the Navier-Stockes equation of motion

$$\rho \frac{\partial \boldsymbol{v}}{\partial t} + \rho(\boldsymbol{v}\nabla)\boldsymbol{v} = -\nabla \boldsymbol{p} - \rho \boldsymbol{g} \tag{5.1}$$

with the density ρ, the flow velocity $\boldsymbol{v}$, the pressure $\boldsymbol{p}$ and the body acceleration $\boldsymbol{g}$. For a steady state, radial symmetry and the gravity field of the Sun this simplifies to

$$mNv\frac{\mathrm{d}v}{\mathrm{d}r} = -\frac{\mathrm{d}p}{\mathrm{d}r} - \frac{GM_\odot mN}{r^2} \tag{5.2}$$

with the gas total number density N, its mean particle mass m, its velocity in radial direction v, its pressure p, the distance from the center of the Sun r, the gravitational constant G and the solar mass $M_\odot$. In addition he used the integrated continuity equation of fluid dynamics

$$Nvr^2 = C \tag{5.3}$$

with the wind's number current C and the ideal gas law

$$p = Nk_\mathrm{B}T \tag{5.4}$$

with the Boltzmann constant k_B and the temperature T. For simplicity Parker assumed a constant temperature $T(r) = T_\odot$ which is maintained at is coronal value by unknown heating processes so that

$$\frac{\mathrm{d}p}{\mathrm{d}r} = \frac{\mathrm{d}N}{\mathrm{d}r} k_\mathrm{B} T + N k_\mathrm{B} \frac{\mathrm{d}T}{\mathrm{d}r} = \frac{\mathrm{d}N}{\mathrm{d}r} k_\mathrm{B} T_\odot. \tag{5.5}$$

Despite this simplification Parker's first solution of a stationary expanding solar wind provided wind velocities similar to those later observed. His implicit analytic expression for the wind velocity is independent of the current C and depends on the temperature T as free parameter.

Weber (1970) improved Parker's model further by removing the isothermal simplification with the integrated energy equation

$$mNvr^2 \left(\frac{1}{2} v^2 + \frac{5p}{2Nm} - \frac{GM_\odot}{r} \right) = \left(r^2 \kappa \frac{\mathrm{d}T}{\mathrm{d}r} \right) + E_\infty, \tag{5.6}$$

where E_∞ is the energy flux at infinite distance and $\kappa = \kappa_0 T^{5/2}$ is the thermal conductivity of the coronal plasma. The physical meaning of the three terms on the left are flux of kinetic energy, enthalpy and gravitational energy. The first term on the right is the conductive flux Priest (1982, Chapter 12). Since this model provides a decreasing temperature the solar wind is cooler, slower and denser.

Parker's solution provides the velocity of the solar wind as function of distance and temperature as parameter, but independent of the density. In order to obtain a density one needs to determine it for example through the electron current C. Mann et al. (1999) chose C according to Schwenn (1990) and a temperature of $10^6\,\mathrm{K}$ that resulted in a fourfold Newkirk density, which is often found in coronal streamers and loops. Generally the density in the corona is often heterogeneous and varies with coronal structures by three orders of magnitude (Koutchmy, 1994; Warmuth and Mann, 2005a).

5.2 A New Density Model with Heat Conduction and Alfvén Waves

To derive a density model that is well suited for most LOFAR solar observations we follow the approach by Mann et al. (1999) for fitting the solution by Parker (1958) to observations Schwenn (1990) and Newkirk (1961). We use the same parameters of Mann et al. (1999) shown in Table 5.1 and find a temperature of $1.17 \times 10^6\,\mathrm{K}$ reproducing the Newkirk density of $8.8 \times 10^8\,\mathrm{cm}^{-3}$ (Table 5.2, Fig. 5.5 and 5.6). However, the density at the LOFAR observation range of $2\,R_\odot$ and closer to Earth is too low by 15%. An explanation is the constant coronal temperature of the Parker model, which is unrealistic and leads to lower densities.

To avoid this problem we fit the model by Weber (1970) to the Newkirk density which has a variable temperature by including the energy equation of Eq. 5.6. This system of differential equations requires two additional boundary conditions for the temperature. These temperatures $T_\odot$ and $T_\oplus$ are chosen according to Schwenn (1990) in Table 5.1. Solving this system of equations was delicate and is described in App. C. Table 5.2 shows that the solution labeled New($P_0 = 0$) also provides the correct density at $R_\odot$. At the LOFAR observation range of $2\,R_\odot$ and close to Earth its densities are

Table 5.1: Parameters and their references of the new density model: (a) Newkirk (1961), (b) Schwenn (1990), (c) Mann et al. (1999), (d) Priest (1982), (e) Hackenberg, Marsch, and Mann (2000). m_p is the proton mass. The temperatures are calculated in App. B. The values represent a long term average of the fast and slow solar wind.

Parameter	Symbol	Value	Reference
Electron number density at $R_\odot$	$N_\mathrm{e}(R_\odot)$	$8.8 \times 10^8/\mathrm{cm}^2$	a
Electron number density at $2R_\odot$	$N_\mathrm{e}(2R_\odot)$	$2.8 \times 10^6/\mathrm{cm}^2$	a
N_e at $0.3\,\mathrm{AU} < r < 1.0\,\mathrm{AU}$	$N_e(r)$	$N_{\mathrm{e},\oplus} \times (r/\mathrm{AU})^{-2.10}$	b
Electron number density at Earth	$N_{\mathrm{e},\oplus}$	$6.59\,\mathrm{cm}^{-3}$	c
Electron number current	C	$6.266 \times 10^{34}\,\mathrm{s}^{-1}$	c
Temperature at the Sun	$T_\odot$	$1.4 \times 10^6\,\mathrm{K}$	c
Temperature at Earth	$T_\oplus$	$0.14 \times 10^6\,\mathrm{K}$	c
Relative atomic mass in units of m_p	μ	0.6	d
Mean particle mass	m	μm_p	d
Thermal conductivity (parallel to B)	κ	$10^{-11}(T/\mathrm{K})^{5/2}\,\mathrm{W/mK}$	d
Radial magnetic field	$B_\odot$	$2\,\mathrm{G}$	e

Table 5.2: Temperatures and electron number densities according to observations (Table 5.1) and different solutions of the new density models introduced in this chapter. The wave parameters P_a and P_b are 2.2 and $5.9\times10^{-6}\,\mathrm{Jm}^{-3}$, respectively. Values that fit the observations are marked in gray.

Model	$T(R_\odot)$ [10^6 K]	T(1AU) [10^6 K]	$N_\mathrm{e}(R_\odot)$ [$10^8\,\mathrm{cm}^{-3}$]	$N_\mathrm{e}(2\,R_\odot)$ [$10^6\,\mathrm{cm}^{-3}$]	N_e(0.3 AU) [cm^{-3}]	N_e(1 AU) [cm^{-3}]
Observations	1.4	0.14	8.8	2.8	83	6.6
Mann	1.0	1.0	53.8	5.2	91	6.5
Parker	1.17	1.17	8.8	2.4	81	5.7
New($P_0 = 0$)	1.24	0.14	8.8	3.1	119	9.2
New($P_0 = P_a$)	1.22	0.14	8.8	2.8	101	7.9
New($P_0 = P_b$)	1.19	0.14	8.8	2.4	83	6.6

higher than observed by about 10% and 40%. But it also provides a higher coronal temperature of 1.24 MK and the correct temperature of 0.14 MK at Earth.

Despite its correcter physical description the model with a variable temperature did not generally provide more realistic densities. Apparently the solar wind model is missing some acceleration. Additional acceleration could arise from pressure and heating from Alfvén waves. Therefore we include such terms as done by Hackenberg, Marsch, and Mann (2000). The first term for Alfvén wave pressure p_A is added to the equation of motion providing

$$mNv\frac{\mathrm{d}v}{\mathrm{d}r} = -\frac{\mathrm{d}p}{\mathrm{d}r} - \frac{GM_\odot mN}{r^2} - \frac{\mathrm{d}p_\mathrm{A}}{\mathrm{d}r}, \tag{5.7}$$

where

$$p_\mathrm{A}(r) = \frac{1}{2}P_0 \log\left(\frac{\omega_\mathrm{H}}{\omega_\mathrm{L}}\right) \frac{\frac{v(R_\odot)}{v_\mathrm{A}(R_\odot)}\left(1+\frac{v(R_\odot)}{v_\mathrm{A}(R_\odot)}\right)^2}{\frac{v(r)}{v_\mathrm{A}(r)}\left(1+\frac{v(r)}{v_\mathrm{A}(r)}\right)^2} \tag{5.8}$$

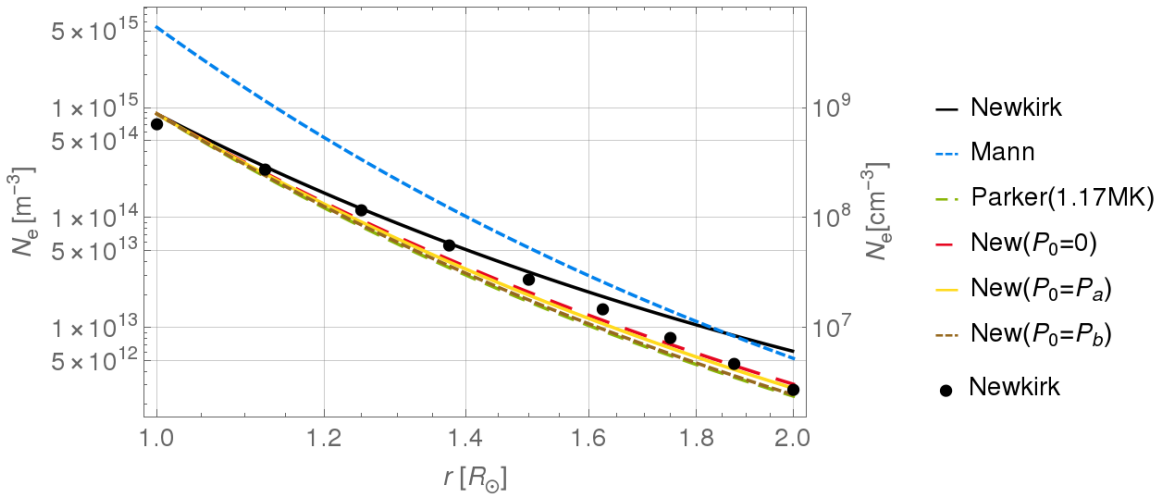

Figure 5.5: Electron density in the corona according to the density models of Table 5.2. The new model fits the Newkirk observations (points) well.

with a wave energy density parameter P_0, the lower and higher cut-off frequencies of Alfvén wave spectrum ω_L and $\omega_\mathrm{H} = 0.8\,\Omega_\mathrm{p}$ with the proton-cyclotron frequency

$$\Omega_\mathrm{p} = B(r)e/m_\mathrm{p}, \tag{5.9}$$

where e and m_p are the elementary charge and proton mass and the radial magnetic field given by our simplified choice as

$$B(r) = B_\odot(R_\odot/r)^2 \tag{5.10}$$

in terms of the magnetic field $B_\odot$ at $R_\odot$ and the Alfvén velocity

$$v_\mathrm{A}(r) = B(r)/(\mu_0 m N)^{1/2}, \tag{5.11}$$

with the vacuum permeability μ_0. We assume that the initial length of the Alfvén waves is limited by the diameter of the supergranules of 30×10^6 m. Hence the lower cut-off frequency is given as

$$\omega_\mathrm{L} = 2\pi/(30 \times 10^6\,\mathrm{m}/v_A(R_\odot), \tag{5.12}$$

where v_A is calculated for the density determined by Newkirk (1961) (Table 5.1).

Second we use the energy equation in its differential form and add the term H for the heating by Alfvén waves to obtain

$$Nv\left(\frac{3}{2}k_\mathrm{B}\frac{\mathrm{d}T}{\mathrm{d}r} - k_\mathrm{B}\frac{T}{N}\frac{\mathrm{d}N}{\mathrm{d}r}\right) = \frac{1}{r^2}\frac{\mathrm{d}}{\mathrm{d}r}\left(r^2\kappa\frac{\mathrm{d}T}{\mathrm{d}r}\right) + H, \tag{5.13}$$

where

$$H(r) = -P_0[v(r) + v_\mathrm{A}(r)]\frac{1}{\omega_\mathrm{H}}\frac{\frac{v(R_\odot)}{v_\mathrm{A}(R_\odot)}\left(1+\frac{v(R_\odot)}{v_\mathrm{A}(R_\odot)}\right)^2}{\frac{v(r)}{v_\mathrm{A}(r)}\left(1+\frac{v(r)}{v_\mathrm{A}(r)}\right)^2}\frac{\partial\omega_\mathrm{H}}{\partial r}. \tag{5.14}$$

Now we can solve this system of equations as before (App. C). With a wave parameter $P_0 = 2.2 \times 10^{-6}\,\mathrm{Jm}^{-3}$ and a slightly lower coronal temperature of 1.22 MK the density

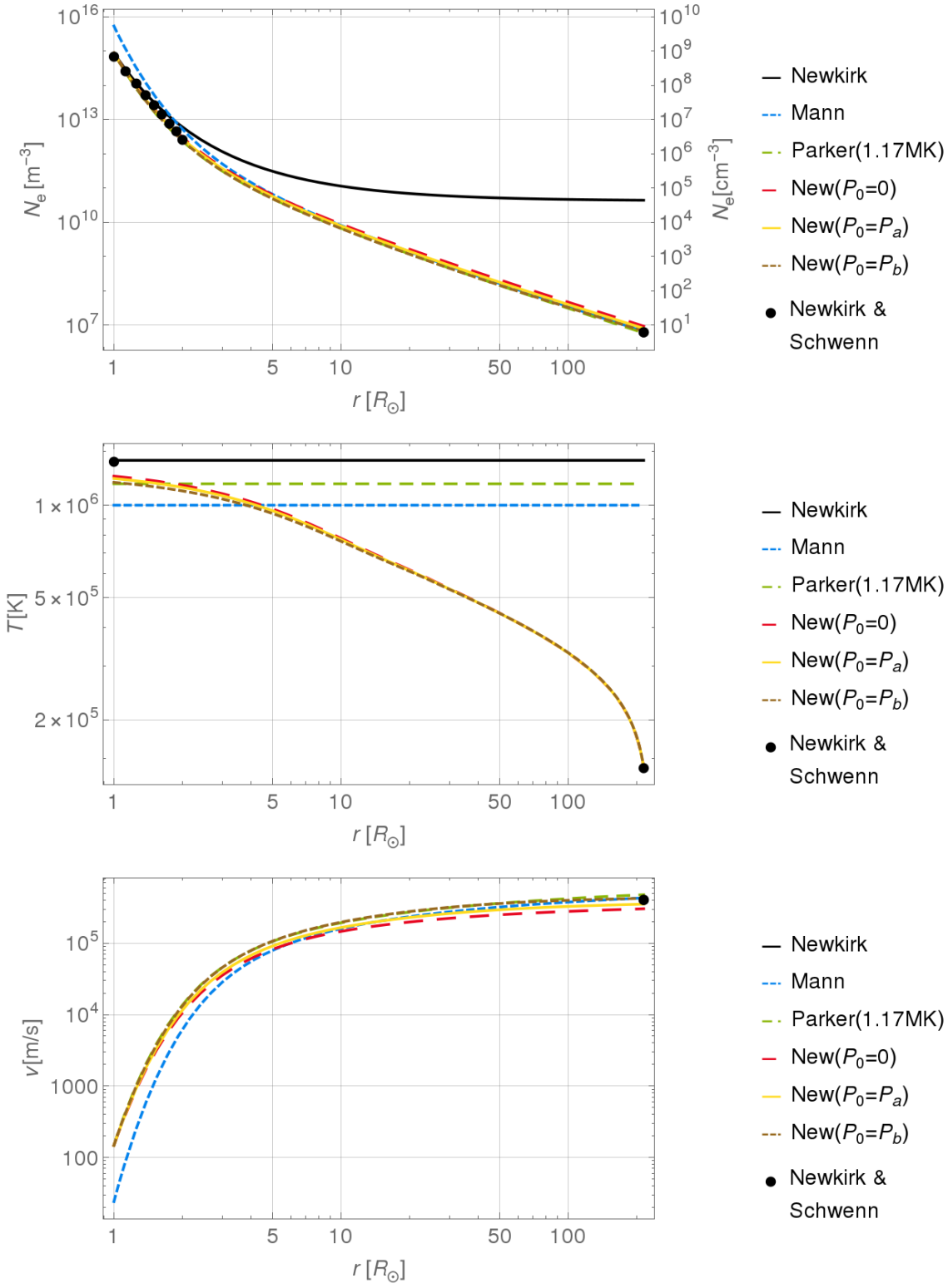

Figure 5.6: Electron density, temperature and velocity of the solar wind in interplanetary space between Sun and Earth according to the models of Table 5.2. The new model fits the observations (points) well.

fits the observed values in the corona at 1 and 2 $R_\odot$. Toward Earth the densities are higher than observed by about 20% (Table 5.2).

However, with a different wave parameter $P_0 = 5.9 \times 10^{-6}\,\mathrm{Jm}^{-3}$ and a lower temperature of 1.19 MK one can change the model to provide the correct densities at $R_\odot$ and at Earth. Then the density is about 15% too small at a distance of $2\,R_\odot$ (Table 5.2). It is noteworthy that the Alfvén pressure of the new model is 2 orders of magnitude less than gas pressure $p(R_\odot)$ and hence its contribution is relatively small.

The colored fields in the table mark the fields which reproduce the observed densities. Fig. 5.5 and 5.6 show the electron number density, temperature and velocity of the different models in comparison. For the analysis of LOFAR data one needs a density model which models the density most accurately in the region of $2\,R_\odot$. So the model with $P_0 = 2.2 \times 10^{-6}\,\mathrm{Jm}^{-3}$ seems best suited for the analysis of solar LOFAR spectra. The results show, that the new model can reproduce the observed density at $R_\odot$ and either at $2\,R_\odot$ or 1 AU simultaneously and can model the electron number density most accurately in the region of LOFAR solar observation.

5.3 Propagation velocity of solar type III bursts

The new density model can now be applied for example to determine the radial propagation velocity of the type III burst on March 16 2016 from the dynamic spectra of Fig. 5.1 to 5.3. As explained in Chapter 3 the frequency of solar radio burst is determined by the plasma frequency ($n = 1$) and its first harmonic ($n = 2$)

$$f_{\mathrm{pe}}(n) = \frac{n}{2\pi}\sqrt{\frac{e^2 N_{\mathrm{e}}}{\epsilon_0 m_{\mathrm{e}}}}, \tag{5.15}$$

where ϵ_0 is the vacuum permittivity, e and m_{e} are the charge and mass of the electron and N_{e} is the plasma's electron density. With this expression for f_{pe} the drift rate becomes

$$D_f = \frac{\mathrm{d}f_{\mathrm{pe}}}{\mathrm{d}t} = \frac{\mathrm{d}f_{\mathrm{pe}}}{\mathrm{d}N_{\mathrm{e}}}\frac{\mathrm{d}N_{\mathrm{e}}}{\mathrm{d}r}\frac{\mathrm{d}r}{\mathrm{d}t} = \frac{f_{\mathrm{pe}}}{2N_{\mathrm{e}}}\frac{\mathrm{d}N_{\mathrm{e}}}{\mathrm{d}r}\frac{\mathrm{d}r}{\mathrm{d}t}, \tag{5.16}$$

where t is the time. If we identify the term $\mathrm{d}r/\mathrm{d}t$ as radial propagation velocity v_r we can rewriting Equation (5.16) as

$$v_r = \frac{2D_f}{f_{\mathrm{pe}}} N_{\mathrm{e}} \left(\frac{\mathrm{d}N_{\mathrm{e}}}{\mathrm{d}r}\right)^{-1}. \tag{5.17}$$

D_f can be obtained observationally. Fig. 5.7 shows the drift rates of the type III burst on March 16, 2016. They have been calculated from Table 5.3 as quotients of the differences in frequency and time ($D_f = \Delta f/\Delta t$). The drift rate is often described by a power law (Mann et al., 1999; Reid and Ratcliffe, 2014)

$$D_f = a f_{\mathrm{pe}}^b. \tag{5.18}$$

This fit provides $a = -7.764 \times 10^{-3}\,\mathrm{MHz/s}$ and $b = 1.75$ in the frequency range from 50 kHz to 80 MHz. These values are similar to $-7.354 \times 10^{-3}\mathrm{MHz/s}$ and 1.76 found by Mann et al. (1999) for a group of type III burst in the frequency range from 20 kHz to 170 MHz.

The radial propagation distance as a function of time $r(t)$ is obtained by expanding

$$r(t) = r(N_e(f_{\mathrm{pe}}(t))), \tag{5.19}$$

Table 5.3: Onset times of the leading edge of the type III burst on March 16 2016 found in the dynamic spectra of Fig. 5.1 to 5.3. The values have been determined from the dynamic spectra.

f [MHz]	80	20	10	3	1	0.3	0.1	0.05
t [s]	1	7	30	60	120	300	600	23×60

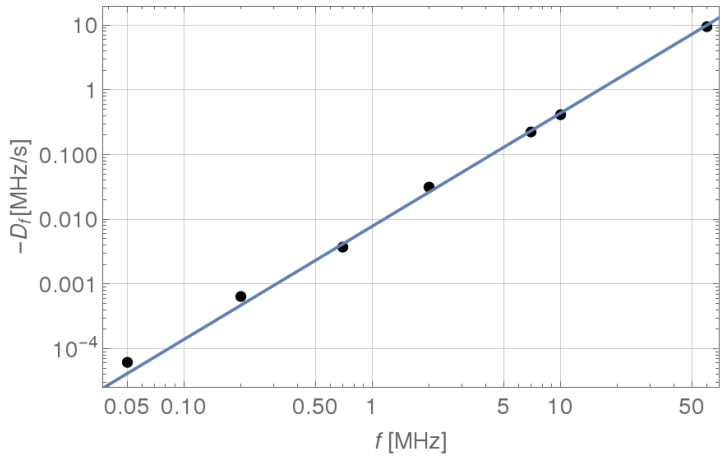

Figure 5.7: Drift rates of the type III burst on March 16 2016 found in the dynamic spectra of Fig. 5.1 to 5.3. The drift rates have been calculated from Table 5.3. The fit to a power law is shown by the blue line.

where r is obtained from a density model. The frequency as a function of time can be found by integration of Eq. 5.18 to

$$f_{\mathrm{pe}}(t) = \left[a(1-b)t + f_0^{1-b}\right]^{\frac{1}{1-b}} . \tag{5.20}$$

Fig. 5.8 to 5.10 show radial distance versus plasma frequency, radial propagation velocity versus radial distance and radial distance versus time as determined from the power law fit for the drift rate and the new density model. Surprisingly v_r first decreases and later increases. This nonuniform propagation also appears in Fig. 5.10 as deviations from the straight lines $l(t) = gt$ with the slope $g = dr/dt$ at $t = 0\,\mathrm{s}$. Also other density models such as the models by Parker (1958) and Newkirk (1961) show a similar behavior. So this is general feature of type III bursts. It is surprising, since it contradict the simple picture of a mono-energetic beam of electrons causing the emission. Hence a more complex explanation is necessary for a first decreasing and later increasing propagation velocity. An ensemble of energetic electrons with a velocity spectrum can explain such a propagation by electrons of different velocities causing the emission at different times and regions.

Observations by radio interferometers like LOFAR can provide direct images of radio bursts and show if the indirect observation of a varying radial propagation velocity from dynamic spectra can be confirmed. This is investigated in Chapter 6.

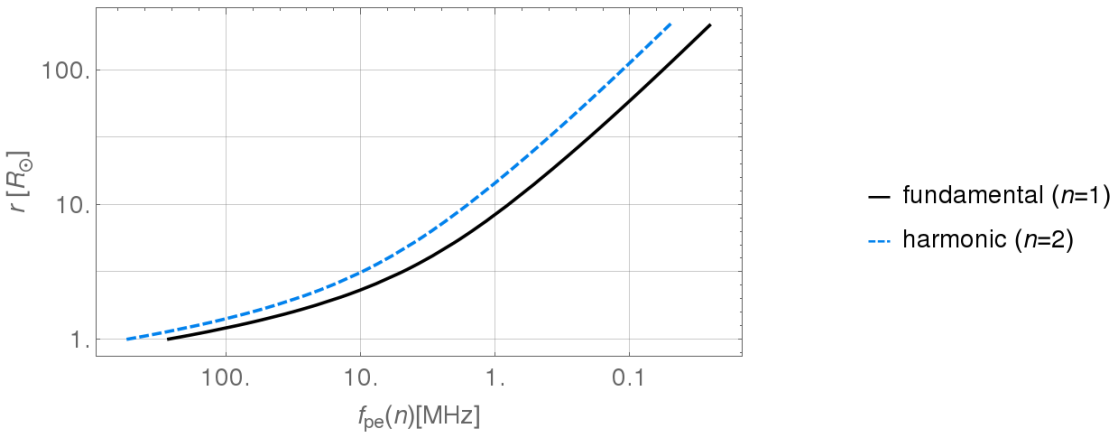

Figure 5.8: Radial distance as function of plasma frequency for fundamental and first harmonic emission according to the new density model.

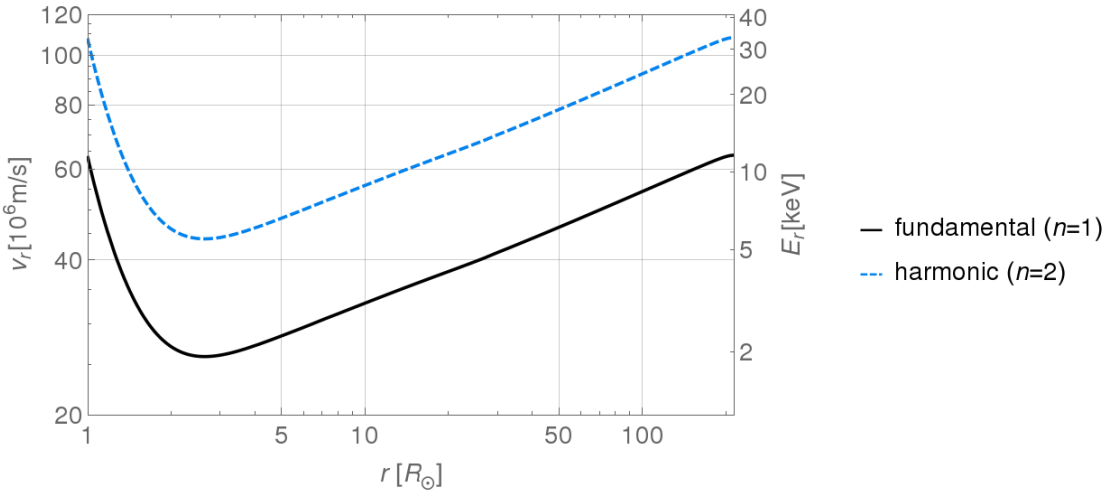

Figure 5.9: Radial propagation velocity of the type III burst on March 16, 2016 for fundamental and first harmonic emission according to the new density model.

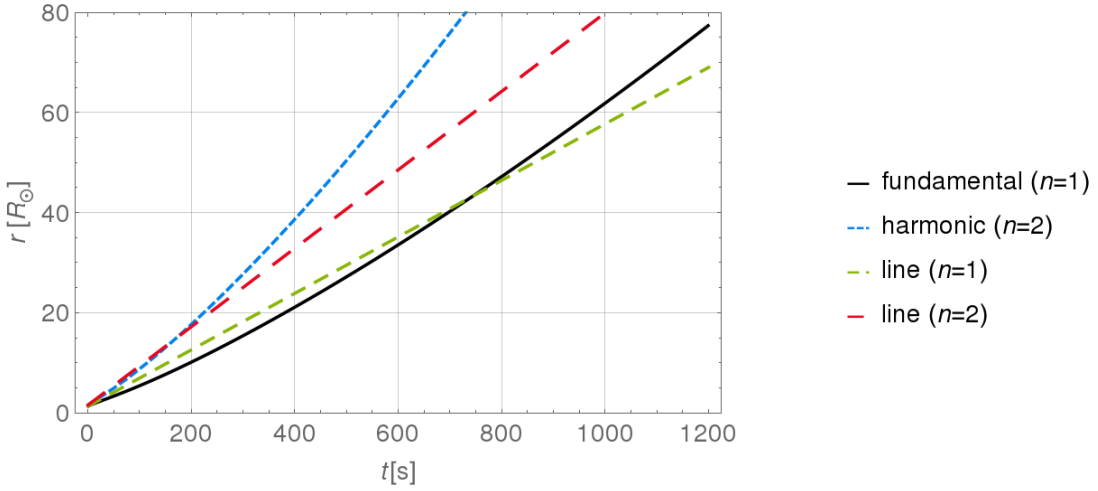

Figure 5.10: Radial distance of the type III burst on March 16, 2016 as function of time for fundamental and first harmonic emission according to the new density model. Lines with velocity at $t = 0\,\mathrm{s}$ serve as reference.

Chapter

6

Solar Type III burst observations with LOFAR

First data from LOFAR observations of the Sun were obtained during LOFAR's commissioning phase in 2010. The Solar Imaging Pipeline converted them into dynamic radio spectra and images. Here the results of one of these observations are presented. They show the quality of solar LOFAR data and allow a discussion of various aspects concerning type III radio bursts that have been captured during the observation period. For example one of these aspects concerns the burst's propagation with respect to the coronal magnetic field lines which have been obtained by the PFSS method introduced in Section 2.3. Another aspect concerns the coronal plasma density which has been obtained using the relation between plasma frequency and electron number density as described in Chapter 5. These and further results are discussed by Mann et al. (n.d.) and in this chapter.

6.1 Observation

LOFAR observed the Sun on June 23, 2012 from 11:00 to 11:10 UTC with 22 core and 9 remote stations in LBA outer configuration in the frequency range from 30 to 80 MHz at 11 equidistant frequencies. The data from 28 low-band antenna stations within 15 km of the central core was used. The time resolution for imaging and dynamic spectra were 0.94 s and 9.8 ms, respectively. Each of these 11 frequency subbands had a bandwidth of 195 kHz and a subdivision into 64 channels. The frequency difference between two subbands Δf was 4.63 MHz. Two sub-array pointings were formed and directed to the Sun and to Virgo A. The latter was used as a calibrator. For each sub-array pointing, the data from the individual LOFAR stations was correlated and integrated to time steps of 0.94 s at the computing center in Groningen, and stored as CASA (McMullin et al., 2007) Measurement Sets for further post processing. Simultaneously, the flux density of the sub-array pointing to the Sun was recorded as dynamic spectrum at the same frequencies but with an increased time resolution of 9.8 ms and stored in LOFAR's HDF5 format for dynamic spectra (Stappers et al., 2011).

6.2 Data Processing

Post-processing was done with LOFAR's Solar Imaging Pipeline (Breitling et al., 2015) and the parameters described in Chapter 4.

The dynamic spectrum was produced with the spectrum maker of the Solar Imaging Pipeline described in Section 4.3.11. The default procedure for the removal of RFI was applied. The removed and included channels are shown in Fig. 6.1. Most channels are free of RFI. Only some channels of the second subband (channels 65–128 at 35 MHz) seem effected. The dynamic channel representation in Fig. 6.2 shows that the RFI of the second subband appears during the whole observation period. Short RFI periods can be seen at a few subbands but the overall quality of the data is good. The remaining channels were processed according to the standard procedure. To emphasize the burst signatures the values were additionally scaled from -0.2 to 1.3, saturating all values greater than 1 or smaller than 0 at white or black respectively. The resulting dynamic spectrum in Fig. 6.3 and Fig. 6.4 was interpolated in time and frequency.

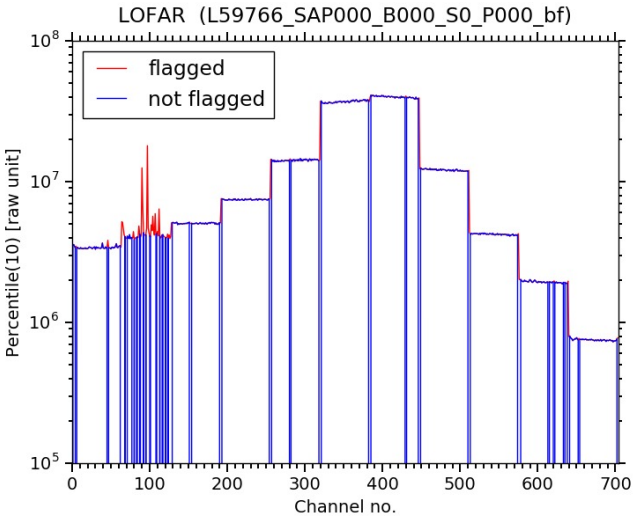

Figure 6.1: Deciles of the intensity (Stokes I) of each channel of the LOFAR beam-formed data. Channels with standard deviations greater than half the decile are printed red. Those channels have been flagged as disturbed by RFI. Also channels close to the edge of a subband are generally flagged. The flagged channels (red) are removed and the remaining channels (blue) are used in the dynamic spectrum.

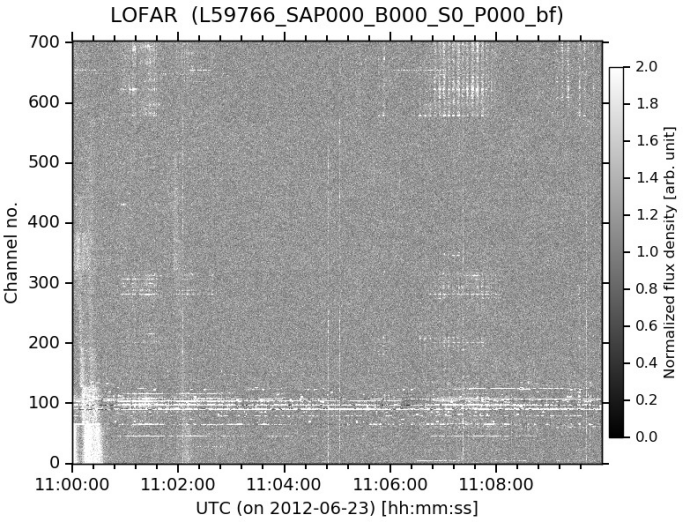

Figure 6.2: Intensity (Stokes I) by channel of the LOFAR beam formed data. Each channel has been divided by its median and the amplitude scale has been truncated at two. The RFI in the second subband (channel 65–128) exists during the total observation period. No other time dependent systematic effects are apparent that could effect the dynamic spectrum.

The imaging also followed the standard procedure described in Chapter 4. This included flagging the channels of the calibrator but not the Sun data for RFI. Subsequently, the channels (excluding channel numbers 1, 2, 63 and 64) of all subbands

were averaged to one channel per subband and the uv-range was limited to 0-1000 wavelength. For the calibration amplitude and phase corrections were determined for every 30 seconds of calibrator data using a corresponding sky model of Taurus A. The solutions were transferred to the data of the Sun. The imaging of the corrected data happened with the multi-scale CLEAN algorithm provided by CASA and transforming from equatorial to solar coordinates. This was done for each time step of 1 s and each frequency.

6.3 Dynamic Spectrum

Fig. 6.3 shows the dynamic radio spectrum from LOFAR of the first 3 minutes of the observation and the X-ray flux density measured by the GOES 15 satellite. The signature of three type III radio bursts can be identified in the radio spectrum at 11:00:04, 11:00:25 and 11:01:55 UTC. The X-ray flux does not show a significant variation during this period.

Fig. 6.4 shows the first burst starting at 11:00:04 UTC on a smaller time scale. The dynamic spectra of the other two bursts look similar. The burst starts at 55 MHz and drifts to 30 MHz within about 10 s. This corresponds to a frequency drift of -2.5 MHz/s which is typical drift rate for type III bursts in this frequency range (Mann and Klassen,

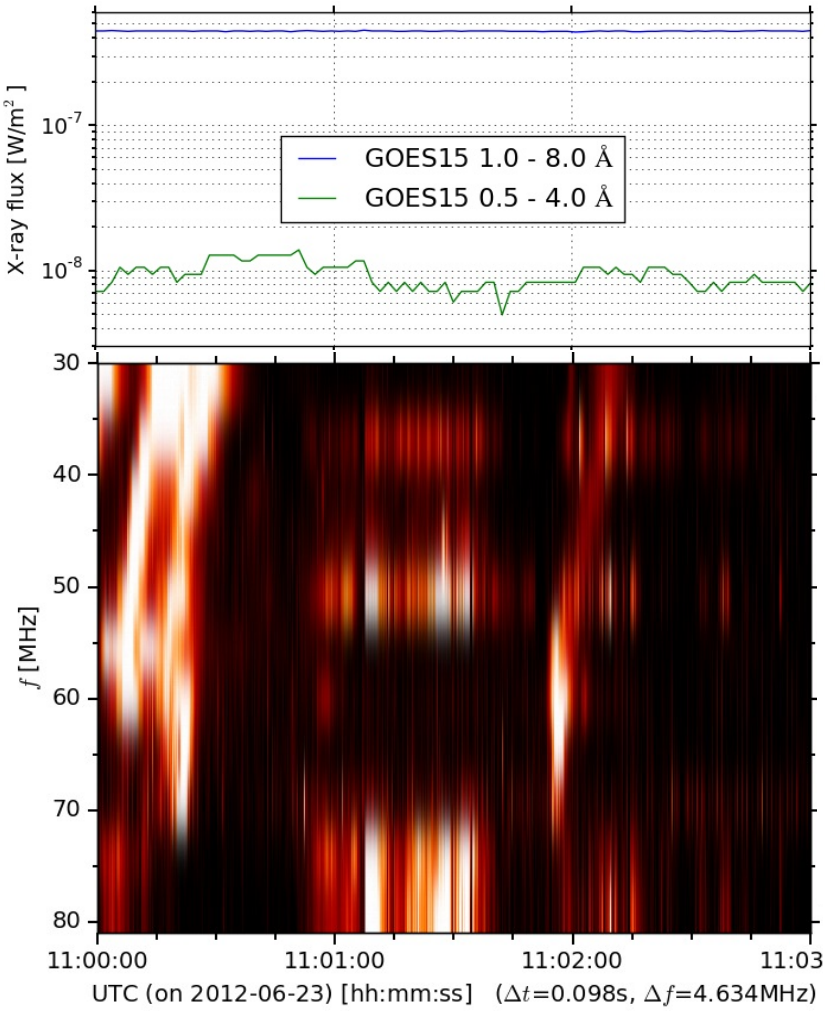

Figure 6.3: Dynamic radio spectrum (bottom) of the LOFAR observation of the Sun on June 23 2012 showing the normalized flux density. Typical signatures of three type III bursts are found at 11:00:05, 11:00:25 and 11:01:55 UTC. They exceed the flux density of the quiet Sun by 20% at 60 MHz and 100% at 30 MHz. The other vertical features between the second and third burst are broadband radio frequency interference (RFI). The simultaneous X-ray flux from the GOES 15 satellite (top) does not indicate any significant activity.

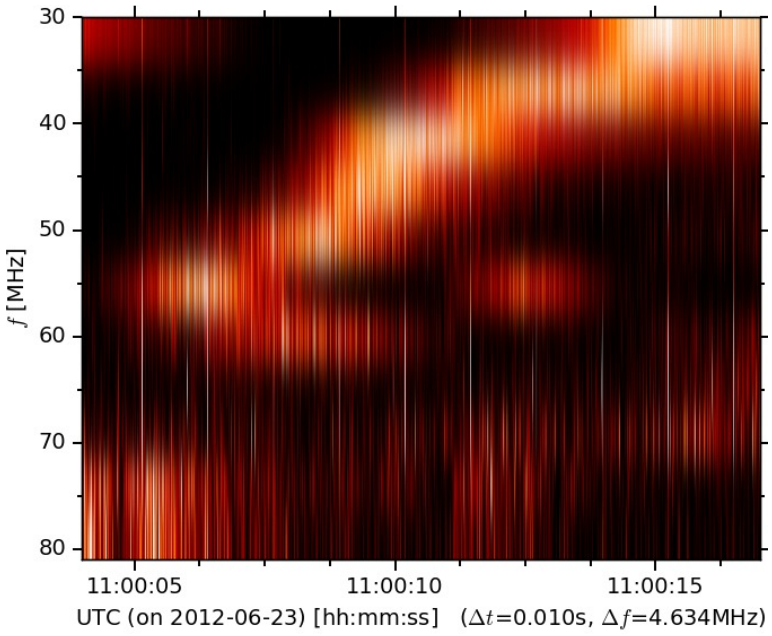

Figure 6.4: Dynamic radio spectrum of the type III burst at 11:00:04 UTC on June 23, 2012. It starts at 55 MHz and drifts to lower frequencies. Also a reverse burst appears at the same time drifting from 55 to 60 MHz.

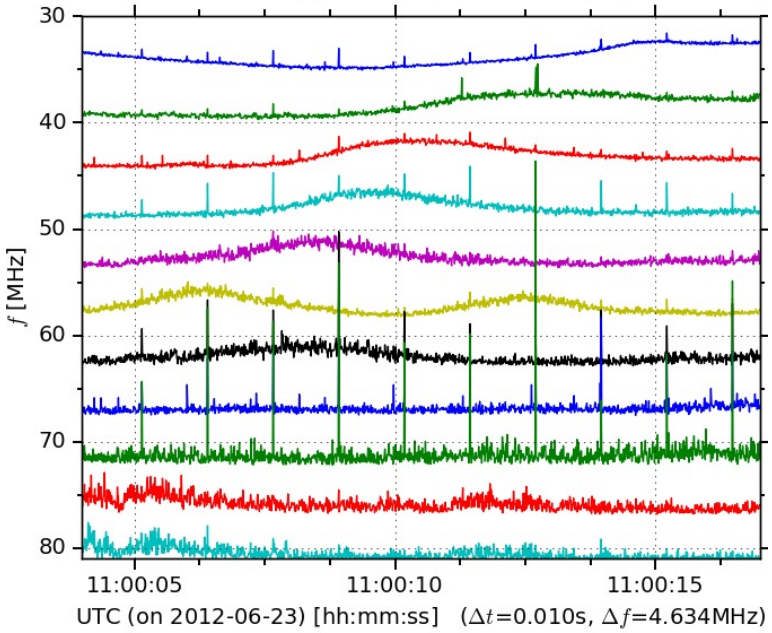

Figure 6.5: Amplitudes of normalized flux density of the dynamic spectrum of Fig. 6.4. The normalized flux density from 0 to 1 (Section 4.3.11) was further divided by 2 and offset by the observation frequency. So a constant signal corresponds to a horizontal line at the observation frequency, while a variable signal results in vertical deviations from this line.

2002). In addition a short reverse burst is visible with a frequency drift from 55 MHz to 60 MHz. The dynamic spectrum of the first two minutes with high time resolution is shown in Fig. D.13. Fig. 6.5 shows the amplitudes of the normalized flux density at different frequencies. This alternative representation allows a more precise timing. If the onset time of the burst is defined as its time of maximum slope change (second time derivative) of the flux density then the times t_s in Table 6.1 are obtained from Fig. 6.5.

6.4 Sky Maps

An overview of the LOFAR sky maps of the first two minutes of observation is shown by Fig. D.1 to Fig. D.12 of App. D. They show the quiet Sun and the location of the three type III bursts that have been found in the spectrum. The Sun and the burst appear as extended circular and an almost point like Gaussian source respectively. Depending

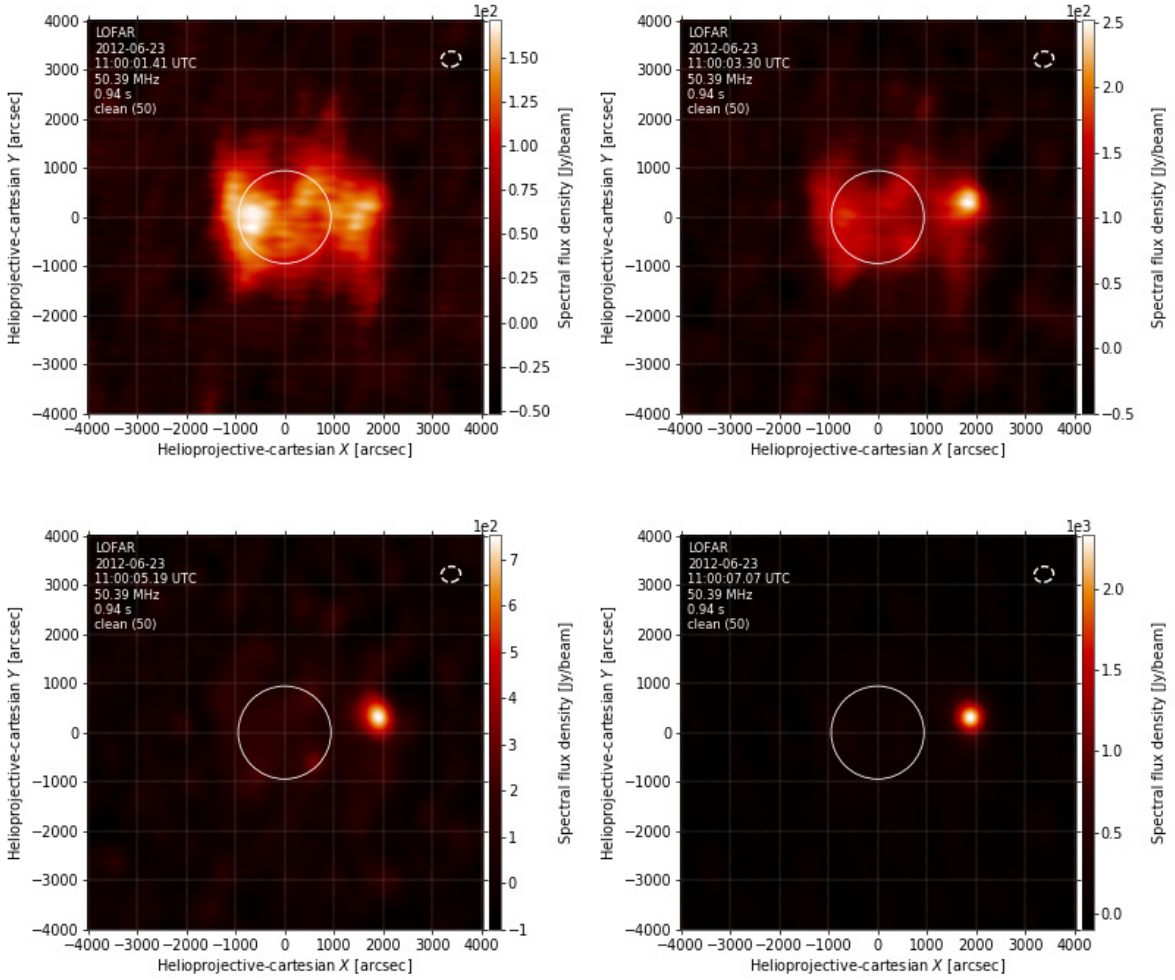

Figure 6.6: LOFAR sky maps of the Sun on June 23, 2012 at 50 MHz with an exposure of 1 s. The Sun and the type III burst is visible in the first and last images respectively. Next to the bright radio burst the radio flux from the Sun is too small to be seen.

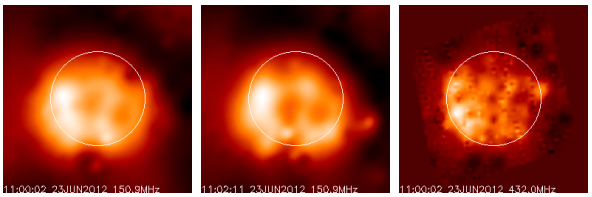

Figure 6.7: NRH sky maps of the Sun on June 23, 2012 at 151 MHz starting at 11:00:02 UTC (left) and 11:02:11 UTC (middle) and at 432 MHz starting at 11:00:02 UTC (right) with an exposure of 10 s. (Images from `http://secchirh.obspm.fr/`.)

on their relative brightness either one of them or both are visible.

Fig. 6.6 shows four of these LOFAR images at 50 MHz at four different times before, during and after the onset of the burst. First only the quiet Sun is visible at 11:00:01 UTC with a peak flux density at about 160 Jy/beam. At 11:00:03 UTC the burst appears with a flux density of about 250 Jy/beam. In the last two images its flux density increases to about 1850 Jy/beam so that the Sun completely disappears on this color scale. Fig. 6.7 shows the radio emission from the Sun at 151 and 432 MHz as recorded by the Nançay Radio Heliograph (NRH, Kerdraon and Delouis, 1997) with an exposure of 10 s. Only the quiet Sun is apparent in these maps. This is expected from the dynamic spectrum, which does not show emission at frequencies above 65 MHz.

The brightening of the burst source in the LOFAR images coincides approximately with the burst times determined from the dynamic spectrum, but generally the burst can already be seen earlier in the images than in the spectrum. The start of the first burst appears at 11:00:00 UTC in the first image at 55 MHz in Fig. D.1 even before it is visible in the dynamic spectrum. Later the burst also appears at lower frequencies with a delay of roughly 1 s per 5 MHz. At the lowest observed frequencies of 30 and 35 MHz the burst is already visible earlier. This is probably emission of an earlier burst which is found in the spectrum from the Nançay Decameter Array (DAM, Lecacheux, 2000) at 10:59:45 UTC (Fig. 6.14) discussed in Section 6.7. The burst also coincides with a reverse burst that drifts to higher frequencies of 70 MHz with a slower frequency drift. Especially the third burst shows a very defined short appearance in Fig. D.10 and D.11. It coincides with a burst like feature in the NRH image at 151 MHz in the same region. Fig. 6.7 (middle) shows this image enlarged. If this feature is a burst it could be associated with the LOFAR data and caused by second harmonic radiation.

6.5 Propagation of the Type III Burst

The location above the solar limb provides a good example for studying the spatio-temporal evolution of type III bursts in the corona. For this study the burst region has been imaged in Fig. 6.8. The data had an additional phase-only self-calibration applied using the cleaned images as model. Then imaging was repeated, resulting in a reduced noise and increased brightness of the burst with unchanged position. Since further self-calibration cycles did not result in apparent improvements they were not applied. The astrometric consistency between images of different time and frequency was verified with the image of the Sun which was clearly visible during periods without bursts and remained unchanged.

The burst appears at seven frequencies (f) between 30-60 MHz. Fig. 6.8 shows the burst region for each frequency near the onset time of the burst. They have a delay of 1 s per subband to roughly follow the observed frequency drift. Their time stamp represents the time when half the exposure is reached. The point spread function (PSF) was determined from the LOFAR stations involved and given in terms of the full width at half maximum (FWHM) major (p) $\times$ minor (q) axis of its fit by a two-dimensional Gaussian. The centroid position (X, Y) of the radio source was calculated within the 80% flux density contour, by weighting the position by the flux density and marked by a black cross on top of a white dot in Fig. 6.8. The projected radial distance in the plane of sky of each centroid to the center of the Sun is denoted by r. The propagation distance between one centroid to the next is denoted by $\Delta s = [(Y_{i+1} - Y_i)^2 + (X_{i+1} - X_i)^2]^{1/2}$, where i+1 is the index of the centroid next centroid i. The total propagation distance is s and measured since $t_s = 4.3$ s. Like the PSF, the radio source was fitted by a two-dimensional Gaussian to estimate its size. The results were obtained as the FWHM major (m) $\times$ minor (n) axis, corrected for the contribution from the PSF. The size significantly exceeds the extension of the PSF and shows widening with decreasing frequency. This is typical for type III burst sources (Saint-Hilaire, Vilmer, and Kerdraon, 2013). The numerical values are summarized in Table 6.1 to 6.3. The white dots that mark the source centroids of all frequencies illustrate the path along which the radio source propagates away from the Sun. The 50% flux density contour of the source and the PFS are represented by the yellow and by the dashed blue line respectively.

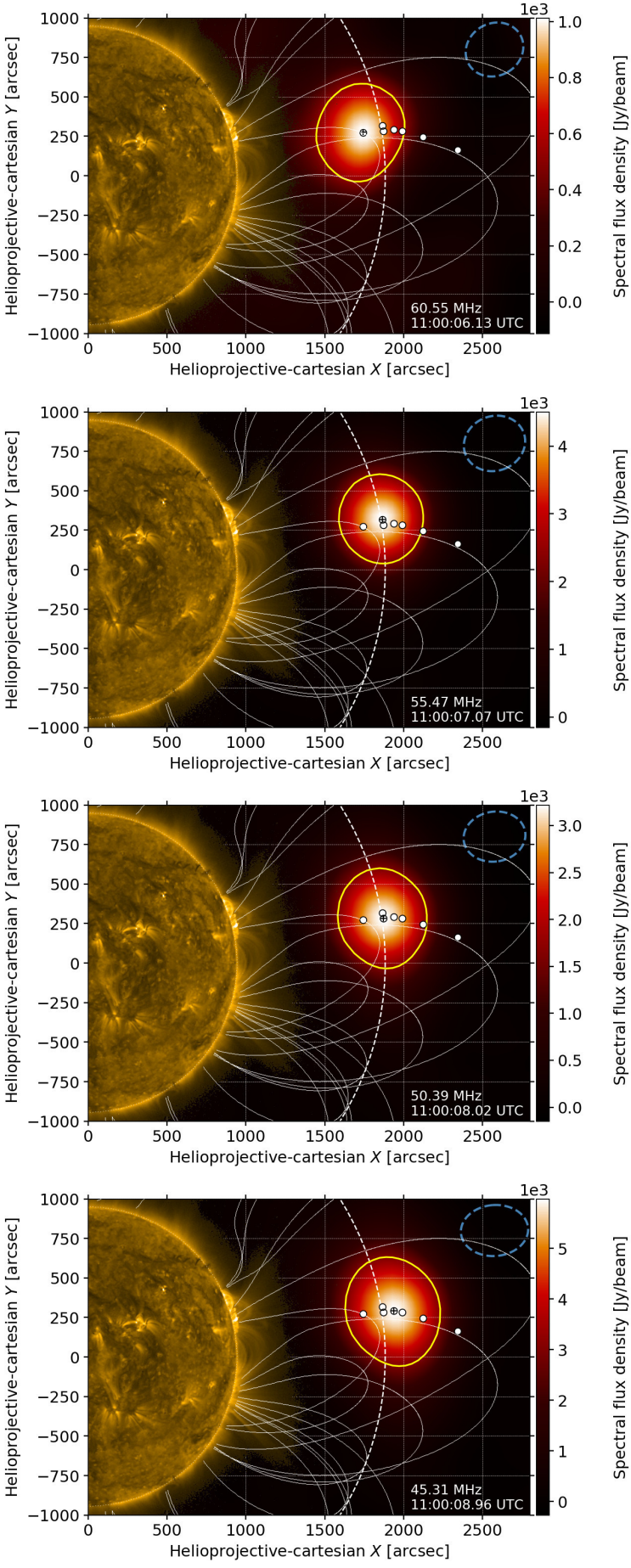

Figure 6.8: LOFAR's imaging spectroscopy of the type III burst of Fig. 6.4 at seven frequencies. The radio source is enclosed by a yellow contour line at a 50% flux density level. The white dots mark the source centers at all observed frequencies (Table 6.1) and show the burst's propagation path. The center at each image frequency is marked by a black cross. The propagation appears outwards and along the coronal magnetic-field lines (white lines). The white dashed line indicates the distance of $2\,R_\odot$. The blue dashed ellipse (top right) represents the FWHM of the Gaussian fit of the PSF. The corresponding extreme ultraviolet (174 Å) image from the SWAP instrument (Halain et al., 2013) on PROBA2 shows the structure of the lower corona.

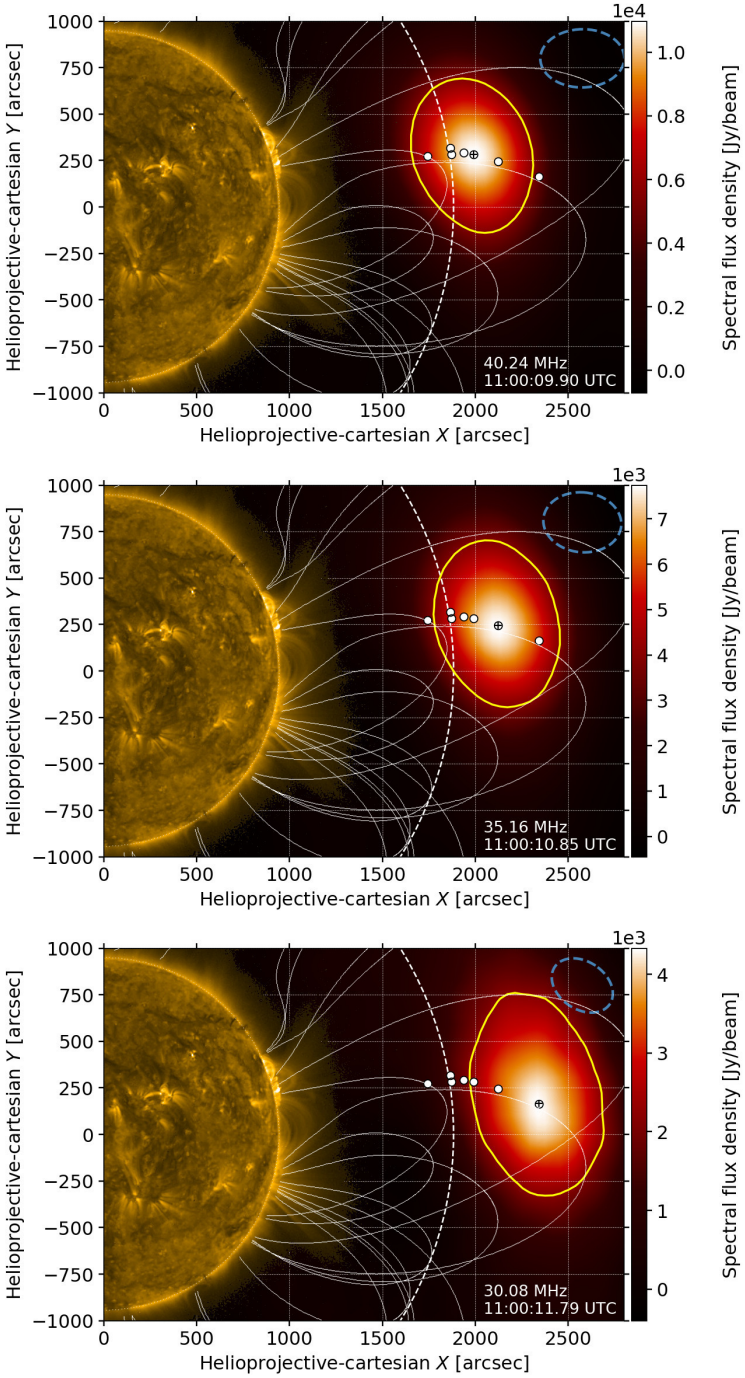

Figure 6.8: Continued for 40, 35 and 30 MHz.

6.5.1 The Coronal Magnetic Field

The white lines in Fig. 6.8 represent the Sun's coronal magnetic field obtained by the potential-field source-surface (PFSS) method described in A. In Fig. 6.8 only field lines originating within a longitude of +15 and -5 degrees from the western limb are shown. They mainly extend westward and coincide with the path of the type III burst source. Hence we assume a propagation in the plane of sky. Because the choice of field lines representing a magnetic field is not unique, we have made a choice with a field line close to the burst's first appearance at 55 MHz. As it drifts to lower frequencies we find that the burst source closely follows this field line. Since the field lines are closed they could confine the electrons to the corona. This could explain why this burst is not

Table 6.1: Parameters from the LOFAR maps and the dynamic spectrum of the type III burst on June 23, 2012: frequency f, time since 11:00:00 UTC of the images t_i and from spectrum t_s, source position X, Y, projected propagation distance s, FWHM major × minor axes of the PSF ($p \times q$) and the radio source ($m \times n$). The geometric quantities have a systematic uncertainty of about 5%.

f	t_i	t_s	X	Y	s	s	$p \times q$	$m \times n$
[MHz]	[s]	[s]	[′]	[′]	[$R_\odot$]	[Mm]	[$10^{3\prime\prime} \times 10^{3\prime\prime}$]	[$10^{3\prime\prime} \times 10^{3\prime\prime}$]
60.6	6.13	6.1	28.9	4.4	-	-	0.38 × 0.33	0.66 × 0.61
55.5	7.07	4.3	30.9	5.1	0.00	0	0.39 × 0.35	0.52 × 0.40
50.4	8.02	6.1	31.1	4.5	0.04	28	0.39 × 0.32	0.68 × 0.44
45.3	8.96	7.0	32.2	4.6	0.11	79	0.43 × 0.32	0.73 × 0.45
40.2	9.90	7.9	33.1	4.5	0.17	116	0.45 × 0.31	0.91 × 0.49
35.2	10.85	9.0	35.3	3.9	0.31	214	0.42 × 0.32	1.0 × 0.55
30.1	11.79	10.0	39.0	2.5	0.55	386	0.36 × 0.26	1.3 × 0.63

detected at lower frequencies at interplanetary space for instance by the Wind satellite (Section 6.7). A propagation along magnetic field lines agrees with the expectations for plasma emission generated by a beam of energetic electrons and with previous observations. For example Klein et al. (2008) located type III bursts associated with solar energetic particle events with NRH in open magnetic flux tubes. Also Boudjada et al. (2014) studied the propagation of type III bursts along the Parker spiral with dynamic radio spectra from satellites.

6.5.2 Propagation Velocity

$f_a - f_b$	Δt	Δs	v
[MHz]	[s]	[$R_\odot$]	[c]
55.5 − 50.4	1.8	0.04	0.05
50.4 − 45.3	0.9	0.07	0.19
45.3 − 40.2	0.9	0.05	0.14
40.2 − 35.2	1.1	0.14	0.30
35.2 − 30.1	1.0	0.25	0.57

Table 6.2: Differences derived from Table 6.1 for the frequency drift from f_a to f_b: propagation time Δt_s, propagation distance Δs and velocity v in units of the velocity of light c.

Table 6.2 shows the propagation velocity v as calculated from Table 6.1 using the burst onset times t_s from the dynamic spectrum. The corresponding diagram of v and the propagated distance s versus time is Fig. 6.9. The error bars reflect the uncertainties of the burst's onset times (0.5 s) and of the fit positions (10 arcsec) of Gaussian functions to the radio maps. The onset of the burst at 55 MHz defines the origin. The propagation velocity of the radio source increases. In total a distance of $0.55\,R_\odot$ (3.9×10^8 m) was traversed by the type III burst within 5.7 s. This corresponds to an average propagation velocity $v = 6.8 \times 10^4$km/s $= 0.23\,c$ (c, velocity of light). This is a typical velocity for type III burst as discussed in Section 3.3.3.

The nonuniform motion of the radio source in Fig. 6.9 agrees with the indirect observation from spectroscopy of nonuniform motion in Fig. 5.9 in Section 5.3.

6.5.3 Propagation Model

The explanation of the nonuniform motion of the radio source by an acceleration of the electron beam associated with the type III burst requires a hypothetical mechanism for which no theory is established. Therefore the question arises whether an alternative explanation without such a mechanism is possible. The following considerations are such an attempt. They start from the conditions for the excitation of radio emission by an electron beam in a plasma. Since the electrons mainly propagate along the magnetic field, its motion can be considered as one-dimensional, their velocity distribution f_{beam} is a function of the particle velocity V, the spatial coordinate s along the magnetic field, and the time t. The electron beam is considered to be injected around $s = 0$ over a spatial length d at the time $t = 0$. Then the velocity distribution function of the electron beam at $t = 0$ can be expressed by

$$f_{\mathrm{beam}}(V, s, t = 0) \sim e^{-(V-V_b)^2/2v_w^2} \times e^{-s^2/2d^2} \tag{6.1}$$

with the beam velocity V_b and the width of the beam v_w in the velocity space (Mel'nik and Kontar, 1999).

In the case of a free or unperturbed propagation, the evolution of the velocity distribution function f can be described by a force-free Vlasov equation (Baumjohann and Treumann, 1996)

$$0 = \frac{\partial f}{\partial t} + V \cdot \frac{\partial f}{\partial s}. \tag{6.2}$$

Here, we neglect the response of the plasma waves excited by the beam back on the electron velocity distribution.

The solution of Eq. 6.2 with the initial condition of Eq. 6.1 provides the spatio-temporal evolution of the electron velocity distribution function as (Estel, 1999)

$$f_{\mathrm{beam}} \propto e^{-(V-V_b)^2/2v_w^2} \times e^{-(s-Vt)^2/2d^2} = e^{-W(V)/2} \tag{6.3}$$

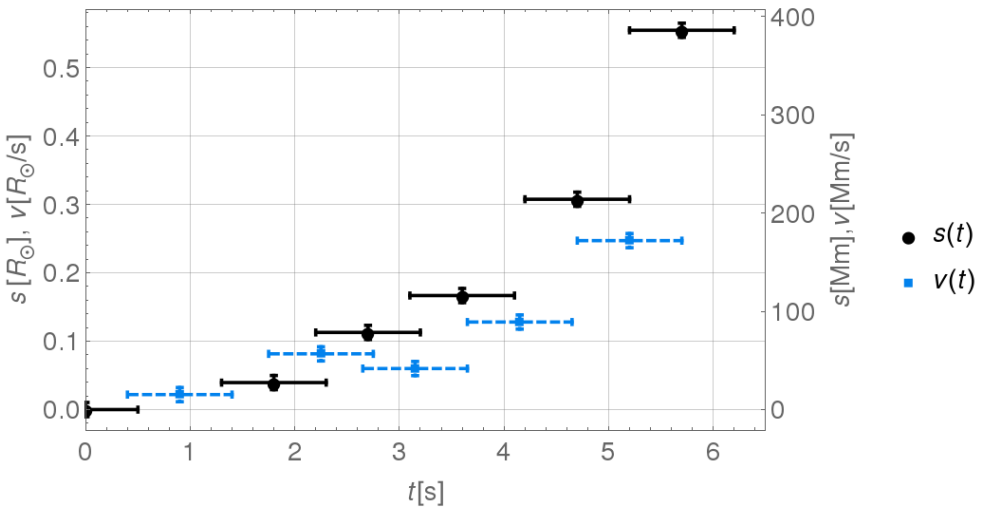

Figure 6.9: Propagation distance s and velocity v of the type III burst on June 23, 2012 in the plane of sky as found in Table 6.1 and 6.2. The velocity increases with time.

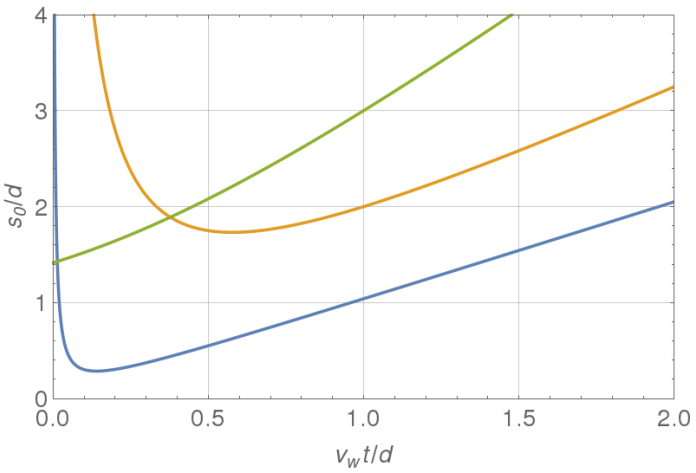

Figure 6.10: The function $s_0(t)$ for the cases: $v_b/v_w = 1$, $V/v_w = 1.02$ (blue line) and $V/v_w = 1.5$ (yellow line) according to Eq. 6.5. The corresponding function s_{max} is given as the green line according to Eq. 6.6.

with

$$W(V) = \frac{\left(1 + \frac{v_w^2 t^2}{d^2}\right)}{v_w^2} \cdot [V - V_{\rm beam}]^2 + \frac{1}{d^2} \cdot \frac{(s - V_b t)^2}{\left(1 + \frac{v_w^2 t^2}{d^2}\right)}$$

and

$$V_{\rm beam} = \frac{\left(V_b + \frac{v_w^2 st}{d^2}\right)}{\left(1 + \frac{v_w^2 t^2}{d^2}\right)} \tag{6.4}$$

This represents a beam-like distribution with the effective beam velocity $V_{\rm beam}$ which is depending on s and t. This means that this beam is formed by different parts of the electron ensemble at different positions and times. Langmuir waves and hence, the type III radio burst radiation are generated by these beam electrons, i.e. by electrons with the velocity $V = V_{beam}$. Langmuir wave excitation requires $\partial f/\partial V > 0$ (Treumann and Baumjohann, 1997; Reid, Vilmer, and Kontar, 2011) leading to the relationship

$$s_0(t) = Vt + \frac{d^2}{v_w^2} \cdot \frac{(V - V_b)}{t} < s. \tag{6.5}$$

between the location $s_0(t)$ of the type III burst source and the time t. For illustration, $s_0(t)$ is presented for two examples in Fig. 6.10. The function $s_0(t)$ has a local minimum at $s_{min} = s_0(t = t_{min}) = 2(d/v_w)[V(V - V_b)]^{1/2}$ and $t_{min} = (d/v_w)[(V - V_b)/V]^{1/2}$. The inspection of Eq. 6.5 shows that, in the case of a monoenergetic beam, i. e. $V = V_b$, $s_0(t)$ reduces to a straight line, i.e. $s_0(t) = V_b t$. The blue line in Fig. 6.10 show such a case with a V close to V_b.

$s_0(t)$ represents the line of the motion of the type III radio burst source. For the type III burst considered here, this curve is shown in Fig. 6.9 as deduced from LOFAR measurements. Because it significantly deviates from a straight line, we conclude that this type III burst is not caused by electrons with nearly the same velocity but by different parts of a broad electron ensemble in velocity space. The inspection of Eq. 6.4 and 6.5 shows, that even in the case of an initial non-beam electron velocity distribution, i. e. $V_b = 0$, the spatio-temporal evolution of the distribution leads to an effective beam-like one as required for the type III radio burst radiation.

In order to guarantee that the beam is carried by enough electrons for generating radio emission, the condition $W(V) < 2$ should be fulfilled for $V = V_{beam}$ (see Eq. 6.4) leading to

$$s_0 < s_{max}(t) = V_b t + d \cdot \sqrt{2\left(1 + \frac{v_w^2 t^2}{d^2}\right)} \tag{6.6}$$

For illustration, the function s_{max} is drawn as the green line in Fig. 6.10. Because of $s_{max} = 2^{1/2}d$ at $t = 0$, the type III radio emission can not take place at large distances, i. e. $s \gg 2^{1/2}d$. That explains, why the type III burst emission starts roughly near the minimum of $s_0(t)$ (see Fig. 6.9 and Fig. 6.10).

So an explanation of the emission as a propagation effect of an ensemble of electrons is possible. Then electrons of different velocities excite plasma emission at different times and locations leading to a nonuniform propagation of the radio source. It does not require a hypothetical acceleration of the electron beam and additionally excludes a monoenergetic electron beam associated with the type III burst.

6.6 The Coronal Plasma Density

As explained in Chapter 3 the emission frequency of a type III burst is determined by the plasma frequency f_{pe} in the emission region. It is emitted at $f \approx n f_{\mathrm{pe}}$ for fundamental ($n = 1$) and harmonic ($n = 2$) emission. Since the plasma frequency is a function of the electron number density N_{e} according to Eq. 5.15 N_{e} is given by the observation frequency as

$$N_{\mathrm{e}} = \left(\frac{2\pi}{n}\right)^2 \frac{\epsilon_0 m_{\mathrm{e}}}{e^2} f_{\mathrm{pe}}^2. \tag{6.7}$$

Table 6.3 shows the electron number density densities corresponding to the observation frequency measured by LOFAR.

The advantage of imaging observations lies in the possibility to localize the emission region. So the emission region can be associated with the observation frequency and hence the electron number density. Thus LOFAR imaging observations of type III bursts provide direct density measurements of the corona. Table 6.3 also contains the radial distance from the Sun as calculated from the X and Y coordinates of the emission regions in Table 6.1. The corresponding profiles of the electron number density are shown in Fig. 6.11. It represents a measurement of the coronal plasma density during the time of observation.

This new measurement can be used to constrains the density models introduced in Chapter 5. Their fit to the data provides density profiles for the whole interplanetary space from $1\,R_\odot$ to 1 AU. The models have been fitted for the case of fundamental and harmonic emission and added to Fig. 6.11. The Newkirk model requires a multiplication constant of 5 and 1.25 respectively. The new model requires a multiplication constant of 11 and 2.75 respectively. However, the new model also fits the data for coronal temperatures $T_\odot$ of 0.9 and 1.1×10^6 K. One can now see that the slope of the Newkirk model is slightly too low as expected for a barometric model according to the discussed in Chapter 5 and Fig. 5.4. On the other hand the slope of the new model with a lower temperature is too high. This is also not surprising since these temperatures are quite low for the corona. This suggests that the solar wind is not streaming away freely from a cold corona as represented by this density model. Instead the increased plasma

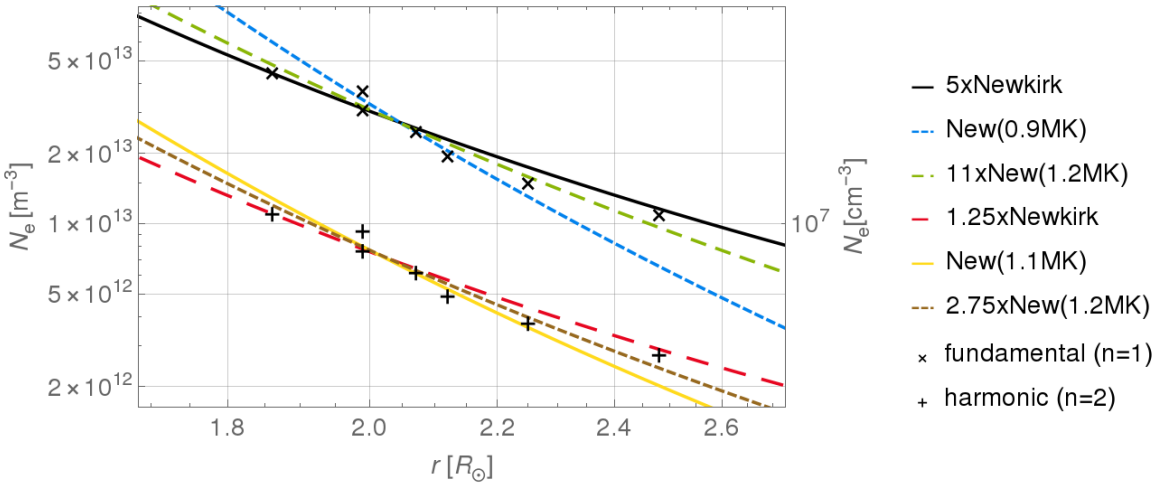

Figure 6.11: Electron number density in the corona versus radial distance from the Sun according to Table 6.3 for fundamental and harmonic emission. Fits of the new density model and that of Newkirk (1961) are shown for comparison.

f [MHz]	r [$R_\odot$]	$N_e(n=1)$ [10^6cm^{-3}]	$N_e(n=2)$ [10^6cm^{-3}]
60.6	1.81	46	11
55.5	1.94	38	9.5
50.4	1.94	32	7.9
45.3	2.02	26	6.4
40.2	2.07	20	5.0
35.2	2.20	15	3.8
30.1	2.42	11	2.8

Table 6.3: Radial distance r and electron number density N_e in the corona derived for fundamental ($n = 1$) and harmonic ($n = 2$) emission from LOFAR radio maps (Table 6.1).

density in the corona could be a result of coronal structures of usually higher density such as streamers. In fact Fig. 6.12 of the Large Angle and Spectrometric Coronagraph Experiment of the SOHO satellite shows a streamer west-northwest exactly at the position of the type III burst. Streamers are radially oriented structures of increased density that extend to a few solar radii (Aschwanden, 2004, Chp. 1). The best fit is provided by the multiplied new model. Its density decreases slower than the colder new model but also not as slow as in the hydrostatic Newkirk model. So by comparison of the observed density profile with that from different models it is possible to distinguish different coronal structures.

A distinction between fundamental and harmonic emission seems more difficult, since the density in the corona is often heterogeneous and varies by three orders of magnitude (Koutchmy, 1994; Warmuth and Mann, 2005a). However, the observation of a type III burst with both (fundamental and harmonic) emissions could allow such a distinction. A monitoring of the Sun is currently discussed as part of the LOFAR upgrade 2.0. This would significantly increase the observation time and hence the number of type III bursts with fundamental and harmonic emission. Then the coronal density will be uniquely defined.

With imaging observations by LOFAR and the Solar Imaging Pipeline new measurements of the corona become available which were previously not available.

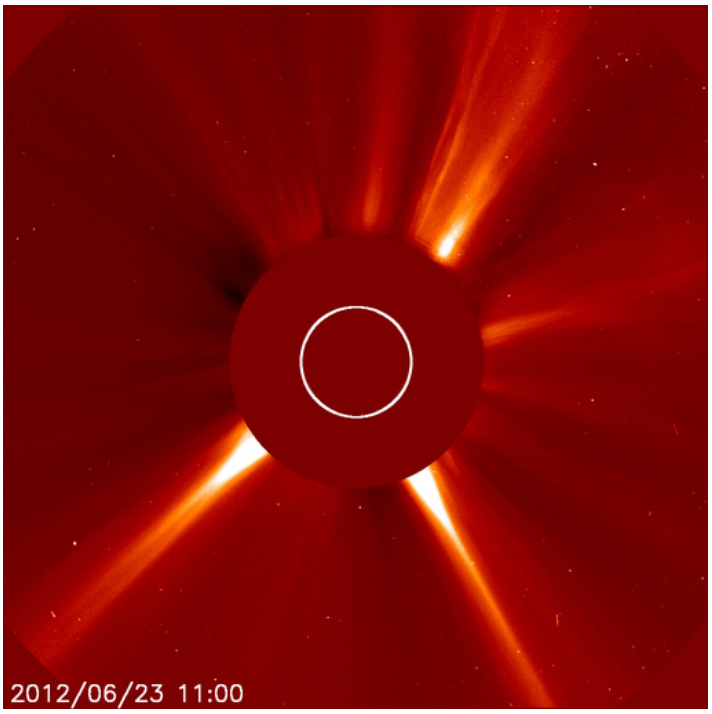

Figure 6.12: Image of visible light of the Large Angle and Spectrometric Coronagraph Experiment (LASCO) of the SOHO satellite. A streamer is visible west-northwest directly at the position where the type III burst occurred and the coronal plasma density has been determined. Image from `https://sohowww.nascom.nasa.gov/data/data.html`.

6.7 Observations from other Instruments

Other instruments that could have seen the bursts are the radio spectrometers of the CALISTO network (Benz, Monstein, and Meyer, 2005), ARTEMIS (Kontogeorgos et al., 2006) and the Nançay Decametric Array (Lecacheux, 2000) which observed the Sun at the same frequencies. Some dynamic spectra are shown in Fig. 6.15 and 6.14. Also the Waves (Bougeret et al., 1995) spectrum in Fig. 6.13 of the Wind satellite could show the burst, if it had propagated to interplanetary space resulting in a drift of the radiation to lower frequencies. However, only the DAM spectrum shows possible faint counterparts. This suggests that these bursts were relatively faint. It also shows LOFAR's high sensitivity. Moreover if the burst is confined to closed field lines in the corona then this can explain why it is not propagating to interplanetary space where it could be detected by the Waves spectrometer. If fundamental emission was observed by LOFAR, then harmonic emission could have been emitted at frequencies as high as the lowest detectable frequency of the NRH. A possible counterpart is seen in the NHR image of Fig. 6.6 that could be associated with this burst. In this case it can be concluded that LOFAR observed fundamental radio emission from the burst.

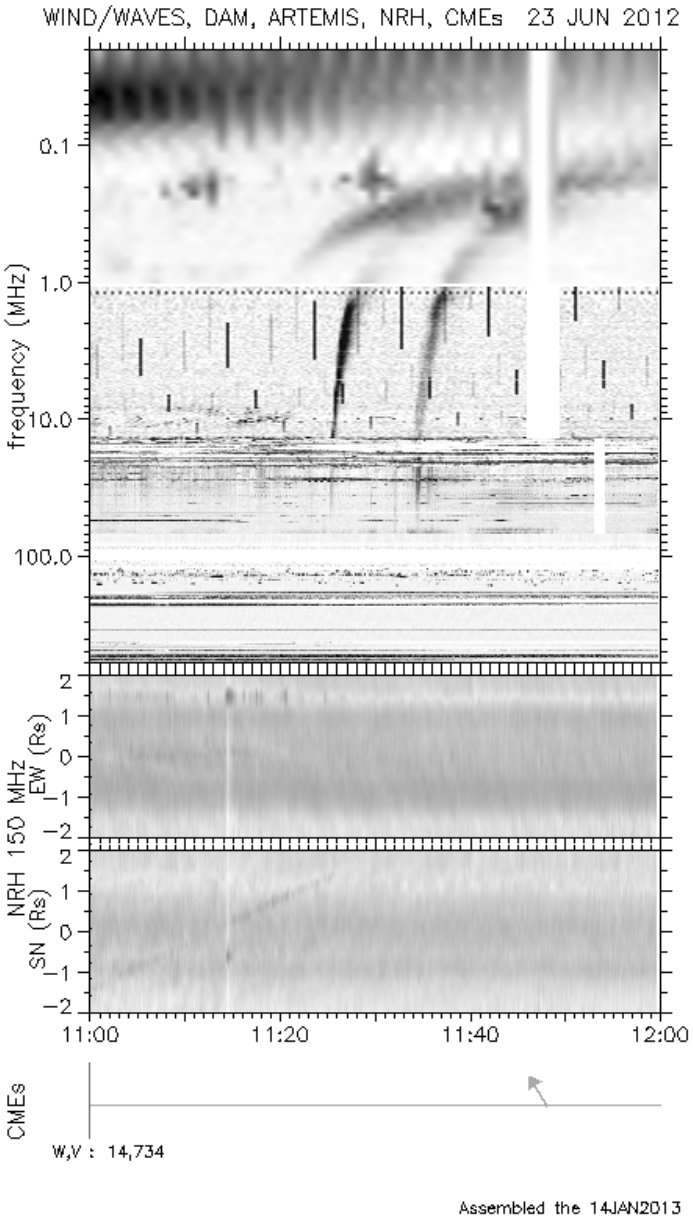

Figure 6.13: Dynamic spectra from different spectrometers covering the LOFAR observation range and lower frequencies. However the LOFAR burst cannot be seen. Figure from `http://secchirh.obspm.fr/`.

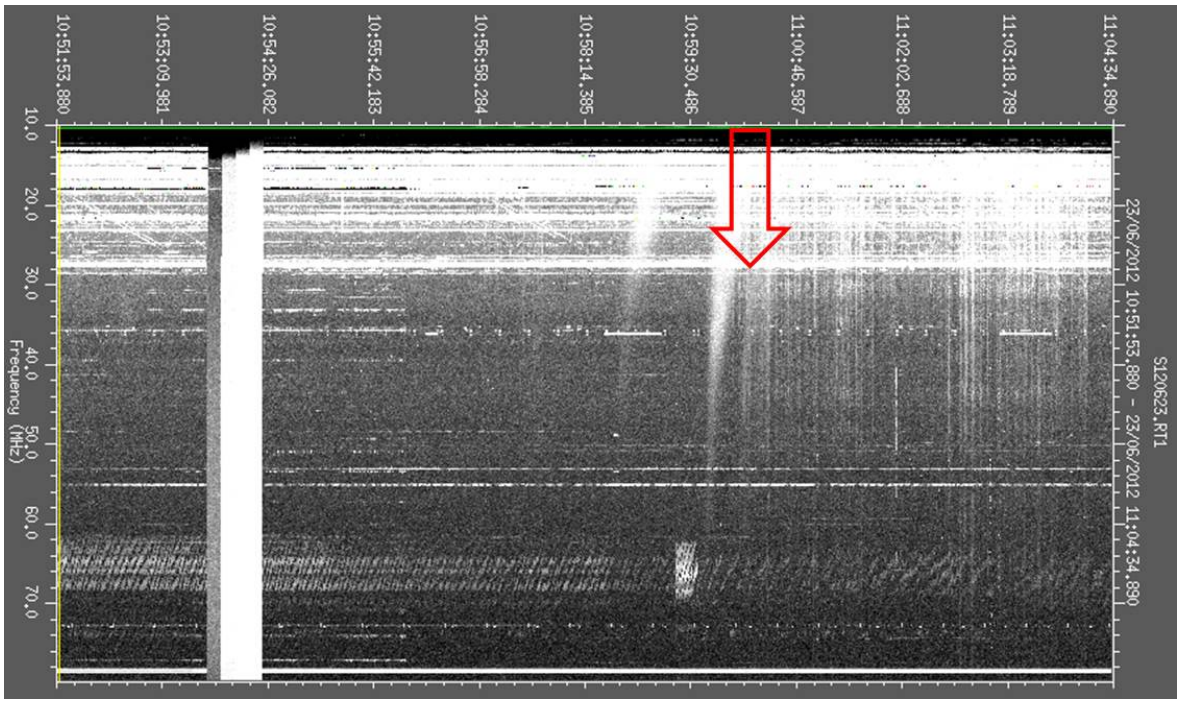

Figure 6.14: Dynamic spectrum of the Nançay Decametric Array. The red arrow points to faint type III burst signatures that could be the type III bursts observed by LOFAR. Also a brighter type III burst is visible about 15 seconds before the first LOFAR burst. This could explain why a burst is already seen at 30 and 35 MHz at 11:00:00 UTC. Data provided by A. Coffre.

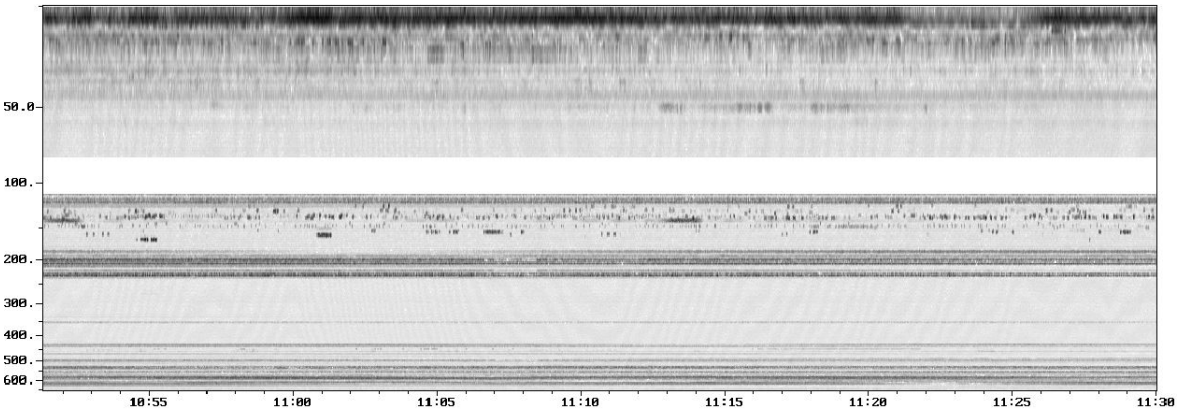

Figure 6.15: Dynamic spectrum of ARTEMIS. No signatures of a solar radio burst are visible that could be associated with the LOFAR burst.

Chapter

7

Summary and Outlook

The Sun is the closest star to Earth and as such a unique plasma laboratory which exposes numerous plasma processes under very different conditions. It also provides unique insights into the phenomena of a star such as differential rotation, a magneto-hydrodynamic dynamo, stellar activity and its associated phenomena such as eruptive events, nonthermal radiation and space weather. Radio telescopes play a central role for the study of these phenomena. The reasons are that their radio emission provides important information about the processes and that some solar radio bursts don't have a counterpart at other wavelengths. The nonthermal radiation is generated predominantly through plasma emission. Solar radio bursts appear in different types and can already be observed by a single antenna of sufficient sensitivity. With sufficient time and frequency resolution dynamic radio spectra can be recorded which show the spectral flux density versus time and the typical signatures of solar radio bursts. From the observed frequency the height of a burst in the corona can be derived via a frequency-height relation. This is given by the plasma frequency as a function of plasma density which decreases with radial distance from the Sun according to the Sun's gravitational field.

With LOFAR a new radio interferometer has become available that provides imaging capabilities in addition to its spectroscopic observation mode. Its images reach unprecedented spectral, temporal and spatial resolution. However, because of many differences between typical astronomical objects and the Sun, it cannot be used for solar observation without essential changes in the observations mode and the data analysis. As a solution the Solar Imaging Pipeline and Solar Data Center was developed. This software package builds on the Standard Imaging Pipeline and contains the necessary modifications for imaging of LOFAR solar data. It also contains software for dynamic spectra. The Solar Data Center provides the corresponding archive and a web interface to access and display an overview of the processed images and spectra. A comparison with other observations for example with images from the Nançay radio heliograph at 151 MHz showed good agreement. Thus the Solar Imaging Pipeline is an essential component for solar observations with LOFAR and their scientific evaluation.

Images of solar radio observations are generally more difficult to obtain than dynamic spectra. Especially the interplanetary space between the Sun and Earth can only be completely covered with spectrometers. But dynamic spectra can also provide information about the location of a radio bursts if the plasma density at the burst

location is known. A new density model for interplanetary space between Sun and Earth has been developed that builds on the fluid equations of motion and energy and includes heat conduction as well as heating and pressure from Alfvén waves. It has been fitted to density measurements in the corona and near Earth and it reproduces consistent results. The application to drift rates of a type III burst observed with LOFAR on March 16, 2016 showed a nonuniform propagation.

High resolution imaging spectroscopic solar observations with LOFAR on June 23, 2016 showed three type III radio burst in the frequency range at 30 to 60 MHz. The images of the burst could clearly resolve its position and extension in the corona while the dynamic spectrum provided the timing information about the burst's onset. This information was used to reconstruct the burst's propagation through the corona. A nonuniform motion along coronal magnetic field lines in the projection on the plane of sky was found with an average velocity of $0.23c$. A propagation along magnetic field lines agrees with the expectations for plasma emission generated by a beam of energetic electrons and with previous observations. The direct observation of a nonuniform propagation of a radio burst with LOFAR confirms previous indirect observations derived from dynamic spectra presented in Chp. 5. The nonuniform propagation could be explained as a propagation effect of an ensemble of electrons with different velocities. This also constrains models of type III bursts by ruling out monoenergetic electron beams exciting the emission. Instead slower and faster electrons cause the radiation at smaller and greater distance from the acceleration region, respectively.

The coronal density was derived in case of fundamental and harmonic emission and used to fit the model by Newkirk and the new model developed in Chp 5. Good agreement was found. This demonstrates, that radio imaging spectroscopy by LOFAR is a useful method for measuring the coronal plasma density in the region from about 1.5 to $2.5\,R_\odot$. This transition region from a static atmosphere to a dynamic solar wind is of great interest since the processes in this region have consequences for the development of the solar wind and its plasma density is an important parameter for many processes in the corona. However so far it is not well measured since it is difficult to observe.

The dynamic spectra of other radio spectrometers show that only one was able to resolve the bursts, too. This demonstrates LOFAR's high sensitivity and its capability to detect bursts that where previously below the detection limit. Generally it was found that LOFAR solar images provide a sensitive and precise basis for studying solar radio bursts.

In the near future an upgrade of LOFAR (2.0) is planed. This upgrade will provide the opportunity of a daily monitoring and continuous low frequency radio images of the Sun. This will support the study of solar activity and space weather by greatly increasing the amount of solar LOFAR data. The upgrade will also increase the number of LOFAR's short baselines and hence LOFAR's uv-coverage and image fidelity for extended objects like the Sun as well as its sensitivity for the detection of faint solar radio bursts. As seen from first LOFAR solar observations, LOFAR's sensitivity is sufficient to regularly observe faint type III bursts. A monitoring with increased sensitivity and resolution will provide enough data for statistical analyses of solar radio burst and also a chance to discover rare and unknown phenomena in the corona. Combined with observations at other wavelengths comprehensive studies will be possible that can provide new insides into radio bursts and their associated processes.

Appendix

A

The Potential-Field Source-Surface (PFSS) Method

The potential-field source-surface (PFSS) method by Schatten, Wilcox, and Ness (1969) is a magnetostatic approach to extrapolate the magnetic field from the photosphere with radius $R_\odot$ to a so called source surface with a radius r_s of about 2 to 4 $R_\odot$. At r_s the magnetic field is significantly modified by the solar wind. As it streams away from the Sun it carries away magnetic flux which leads to field lines mostly orthogonal to the source surface (Fig. 2.5). Here we describe the calculations by Schrijver and De Rosa (2003) which only use the radial component of the magnetic field $\mathbf{B}$ in the photosphere which has been found most reliable (Wang and Sheeley, 1992). This calculations are also implemented in the PFSS package of the IDL library SolarSoft (Bentely and Freeland, 1998). Its assumptions (A) and boundary conditions (BC) are:

A1: the electric and magnetic fields are static, i.e. $\partial\mathbf{B}/\partial t = 0$ and $\partial E/\partial t = 0$,
A2: there are no currents, i.e. $j = 0$,
BC1: the radial component $B_r(R_\odot, \theta, \phi)$ can be measured in the photosphere,
BC2: the $\mathbf{B}$ field is orthogonal to the source surface at $r = r_s$.

A1 leads to the decoupling of Maxwell's equation so that $\mathbf{B}$ is determined by the following two equations

$$\nabla \cdot \mathbf{B} = 0, \tag{A.1}$$

$$\nabla \times \mathbf{B} = \mu_0 j. \tag{A.2}$$

With A2 the curl of $\mathbf{B}$ is zero so that $\mathbf{B}$ can be expressed as gradient of a magnetic scalar (not vector) potential Φ as

$$\mathbf{B} = -\nabla\Phi. \tag{A.3}$$

Then this equation for $\mathbf{B}$ and Eq. A.1 result in Laplace's equation for Φ:

$$\nabla \cdot (-\nabla\Phi) = \nabla^2\Phi = 0. \tag{A.4}$$

Following the notation by Schrijver and De Rosa (2003) it has the general solution

$$\Phi(r, \theta, \phi) = \sum_{l,m} \left[A_l^m r^l + B_l^m r^{-(l+1)}\right] Y_l^m(\theta, \phi), \tag{A.5}$$

with the spherical harmonic functions

$$Y_l^m(\theta,\phi) = C_l^m P_l^m(\cos\theta) e^{im\phi}, \tag{A.6}$$

where $P_l^m(\cos\theta)$ are the associated Legendre functions, the coefficients

$$C_l^m = (-1)^m \left[\frac{2l+1}{4\pi}\frac{(l-m)!}{(l+m)!}\right]. \tag{A.7}$$

A_m^l and B_m^l are free coefficients since each $Y_l^m(\theta,\phi)$ fulfills Laplace's equation. So one can use this freedom of the solution to fulfill the given boundary conditions.

From BC1 one obtains

$$\left.\frac{\partial\Phi}{\partial r}\right|_{r=R_\odot} = -B_r(R_\odot,\theta,\phi) = \sum_{l,m} F_l^m Y_l^m(\theta,\phi), \tag{A.8}$$

where Eq. A.5 implies in units of $R_\odot$ (i.e. $R_\odot$=1)

$$-F_l^m = A_l^m l - B_l^m(l+1). \tag{A.9}$$

From BC2 one obtains

$$\mathbf{B}(r_s,\theta,\phi) = \begin{pmatrix} B_r(r_s) \\ 0 \\ 0 \end{pmatrix} = -\nabla\Phi(r_s,\theta,\phi) => \Phi(r_s,\theta,\Phi) = \Phi(r_s). \tag{A.10}$$

So BC2 implies that Φ is constant at the surface. Moreover since $\mathbf{B}$ is not affected by additive constants to Φ one can chose a gauge transformation such that $\Phi(r_s,\theta,\phi) = 0$. Then Eq. A.5 implies

$$A_l^m r_s^l + B_l^m r_s^{-(l+1)} = 0. \tag{A.11}$$

Hence with Eq. A.11 and A.9 the coefficients are determined and one obtains respectively

$$A_l^m = -B_l^m r_s^{-(2l+1)} \tag{A.12}$$

and

$$B_l^m = \frac{F_l^m}{1+l+lr_s^{-(2l+1)}}. \tag{A.13}$$

Finally the $\mathbf{B}$-field inside the shell of $R_\odot = 1 < r < r_s$ is given by

$$B_r(r,\theta,\phi) = -\sum_{l,m}\left[A_l^m l r^{(l-1)} - B_l^m(l+1)r^{-(l+2)}\right] Y_l^m(\theta,\phi), \tag{A.14}$$

$$B_\theta(r,\theta,\phi) = -\frac{1}{r\sin\theta}\sum_{l,m}\Big\{R_l^m(l-1)\left[A_{l-1}^m r^{l-1} - B_{l-1}^m r^{-l}\right] - \tag{A.15}$$

$$-R_{l+1}^m(l+2)\left[A_{l+1}^m r^{l+1} - B_{l+1}^m r^{-(l+2)}\right]\Big\} Y_l^m(\theta,\phi),$$

$$B_\phi(r,\theta,\phi) = -\frac{1}{r\sin\theta}\sum_{l,m} im\left[A_l^m r^l - B_l^m r^{-(l+1)}\right] Y_l^m(\theta,\phi), \tag{A.16}$$

with the step factor

$$R_l^m = \left[\frac{l^2-m^2}{4l^2-1}\right]^{1/2}. \tag{A.17}$$

It should be noted that the calculations are only valid inside the boundaries ($R_\odot \le r \le r_s$), since A_l^m is generally not zero so that B_r eventually increases for $r \gg r_s$ contrary to observation.

Appendix

B

Temperature of the Solar Wind

B.1 Temperature of the Solar Wind in the Corona

In the region where the solar wind velocity is low ($v \ll v_c$) the coronal density can be approximated by a barometric height formula (Mann et al., 1999) as

$$N(r) = N_\odot \exp\left(\frac{A}{R_\odot}\left[\frac{R_\odot}{r} - 1\right]\right) = N_\odot \exp\left(-\frac{A}{R_\odot}\right) \exp\left(\frac{A}{r}\right), \tag{B.1}$$

with $A = mGM_\odot/(k_B T_\odot)$.

Newkirk (1961) has measured the density profile of the corona through observations of white-light scattering with the K-coronameter at Climax. He found that within a distance of 1 to 1.5 $R_\odot$ the coronal electron density can be approximated by

$$N(r) = (4.2 \times 10^4 \mathrm{cm}^{-3}) \times 10^{4.32 R_\odot / r}. \tag{B.2}$$

A comparison of Eq. B.1 and Eq. B.2 requires

$$10^{4.32 R_\odot / r} = \exp\left(\frac{A}{r}\right) \tag{B.3}$$

$$T = 1.394 \times 10^6 \,\mathrm{K}. \tag{B.4}$$

B.2 Temperature of the Solar Wind near Earth

The solar wind is mainly composed of protons, alpha particles and electrons. Their densities N and temperatures T near Earth was determined with the Helios satellite by Schwenn (1990) as shown in Table B.1. Because the solar wind has neutral charge

Table B.1: Density and temperature of the solar wind near Earth as measured by the Helios satellite according to Schwenn (1990).

N_e	$6.67\,\mathrm{cm}^{-3}$
N_p	$6.10\,\mathrm{cm}^{-3}$
N_α/N_p	$0.047\,\mathrm{cm}^{-3}$
T_e	$0.12\times10^6\,\mathrm{K}$
T_p	$0.14\times10^6\,\mathrm{K}$
T_α	$0.58\times10^6\,\mathrm{K}$

$$N_\mathrm{e} = N_\mathrm{p} + 2N_\alpha = (1 + 2N_\alpha/N_\mathrm{p})N_\mathrm{p} = 1.094N_\mathrm{p} \tag{B.5}$$

The total density of the solar wind is given by

$$N = N_\mathrm{e} + N_\mathrm{p} + N_\alpha = (1.094 + 1 + 0.047)N_\mathrm{p} = 2.141N_\mathrm{p} \tag{B.6}$$

From Eq. B.5 and B.6 follows

$$N_\mathrm{e} = 0.511N. \tag{B.7}$$

For an ideal gas the pressure

$$p = Nk_\mathrm{B}T = k_\mathrm{B}(N_\mathrm{e}T_\mathrm{e} + N_\mathrm{p}T_\mathrm{p} + N_\alpha T_\alpha) \tag{B.8}$$

Hence the effective temperature (p/Nk_B) is giving as

$$T = \frac{1}{N}(0.511NT_\mathrm{e} + 0.467N[T_\mathrm{p} + 0.047T_\alpha]) = 0.14 \times 10^6\,\mathrm{K}. \tag{B.9}$$

Appendix

C

Solving the New Density Model with Heat Conduction and Alfvén Waves

To solve this system of differential equations numerically we use Mathematica 8 (Wolfram Research, 2010) and the iterative method described by Vocks and Mann (2003). The parameters in the equations are know from observations as summarized in Table 5.1. They correspond to a long term average of the fast and slow solar wind.

The initial temperature profile is isothermal with $T = T_\odot$. Then we use Eq. 5.3 to substitute N by an expression of v and rewrite Eq. 5.7 as

$$\frac{\mathrm{d}v}{\mathrm{d}r} = \frac{\frac{2v_\mathrm{s}^2}{r} - \frac{k_\mathrm{B}}{m}\frac{\mathrm{d}T}{\mathrm{d}r} - \frac{GM_\odot}{r^2} - \frac{r^2 v}{mC}\frac{\mathrm{d}p_\mathrm{A}}{\mathrm{d}r}}{\left(v - \frac{v_\mathrm{s}^2}{v}\right)}, \tag{C.1}$$

where $v_\mathrm{s}^2 = k_\mathrm{B}T/m$ is the isothermal sound speed.

In this equation $\mathrm{d}v/\mathrm{d}r$ has a singularity at $v = v_\mathrm{s}$ for which the denominator becomes zero. So v is only defined everywhere if this singularity is removable. This is only the case if the numerator becomes zero as well, i.e. if

$$\frac{2v_\mathrm{s}^2}{r} - \frac{k_\mathrm{B}}{m}\frac{\mathrm{d}T}{\mathrm{d}r} - \frac{GM_\odot}{r^2} - \frac{r^2 v_\mathrm{s}}{mC}\frac{\mathrm{d}p_\mathrm{A}}{\mathrm{d}r} = 0. \tag{C.2}$$

We can solve Eq. C.2 for r and obtain the critical radius r_c. It is the point where the wind speed reaches the sound velocity v_s. Now we can use this solution and l'Hopital's rule to tell Mathematica the specific solution we want. L'Hopital's rule applied to Eq. C.1 provides

$$\frac{\mathrm{d}v}{\mathrm{d}r} = \lim_{r\to r_\mathrm{c}, v\to v_\mathrm{s}} \frac{\frac{\mathrm{d}}{\mathrm{d}r}\left(\frac{2v_\mathrm{s}^2}{r} - \frac{k_\mathrm{B}}{m}\frac{\mathrm{d}T}{\mathrm{d}r} - \frac{GM_\odot}{r^2} - \frac{r^2 v}{mC}\frac{\mathrm{d}p_\mathrm{A}}{\mathrm{d}r}\right)}{\frac{\mathrm{d}}{\mathrm{d}r}\left(v - \frac{v_\mathrm{s}^2}{v}\right)}. \tag{C.3}$$

Now Mathematica is able to find a numerical solution for $v(r)$.

Next we use this solution for v, Eq. 5.3 and the two boundary conditions $T(R_\odot) = T_\odot$ and $T(1\mathrm{AU}) = T_\oplus$ to solve Eq. 5.13 for T to obtain an improved temperature profile.

As it turns out Mathematica 8 cannot find the solution for T in this equation directly. Before we need to make Eq. 5.13 time dependent by adding the term $N\frac{3}{2}k_\mathrm{B}\frac{\mathrm{d}T}{\mathrm{d}t}$ to its left-hand side resulting in

$$N\frac{3}{2}k_\mathrm{B}\frac{\mathrm{d}T}{\mathrm{d}t} + Nv\left(\frac{3}{2}k_\mathrm{B}\frac{\mathrm{d}T}{\mathrm{d}r} - k_\mathrm{B}\frac{T}{N}\frac{\mathrm{d}N}{\mathrm{d}r}\right) = \frac{1}{r^2}\frac{\mathrm{d}}{\mathrm{d}r}\left(r^2\kappa\frac{\mathrm{d}T}{\mathrm{d}r}\right) + H. \tag{C.4}$$

and provide the boundary conditions $T(t_0) = T_0(r)$, $T_\odot(t_1) = T_\odot$ and $T_\oplus(t_1) = T_\oplus$ where $t_0 = 0\,\mathrm{s}$, $t_1 = 10^5\,\mathrm{s}$ and $T_0(r)$ is an initial approximation of the temperature profile by a linear function as

$$T_0(r) = T_\odot - \frac{T_\odot - T_\oplus}{r_\oplus - r_\odot}(r - r_\odot). \tag{C.5}$$

Then Mathematica can find the solution $T = T(t_1)$ which is the stationary solution of Eq. 5.13.

Finally we can use the new temperature profile in Eq. C.1 to improve v and the improved v in Eq. 5.13 to improve T. So iteratively updating v and T defines an algorithm that converges to the solution for v and T. And for any v Eq. 5.3 provides the number density N.

Since the plasma frequency is determined by the electron number density N_e we are more interested in N_e than in total density $N = 1.92N_\mathrm{e}$ (Mann et al., 1999). One can either use N or N_e in the calculation. In case of N_e the total number current C becomes the electron number current. Here N_e was chosen.

Appendix

D

LOFAR's Dynamic Imaging Spectroscopy on 2012-06-23T11:00 UTC

The following figures give an overview of the first two minutes of LOFAR's dynamic high resolution imaging spectroscopy of the solar observation on 2012-06-23T11:00 UTC. This observation period covers three solar type III radio burst which are visible in LOFAR's dynamic spectrum and its images. The period of low activity 11:01:15 to 11:01:44 UTC is omitted. The evolution becomes clear from the combination of the images at different frequency. Each of the figures from Fig. D.1 to D.12 covers 10 s of solar data represented by 10 images with exposure of 1 s. Since these images are taken from the LOFAR Solar Data Center its contains the same rows as described in Section 4.4. It is a LOFAR spectrum followed by images of AIA, NRH and LOFAR with increasing frequency.

The LOFAR images show two kinds of sources: an extended circular and an almost point like Gaussian source. The former one is the quiet Sun the latter is a type III radio burst. Depending on their relative brightness either one of them can be visible or both of them together. The start of the burst can be seen in the first image at 55 MHz in Fig. D.1 even before it can be seen in the dynamic spectrum. Later the burst appears at lower frequencies with a delay of roughly 1 s per 5 MHz. At lowest observed frequencies of 30 and 35 MHz the burst is already visible, probably from the earlier burst that is visible in the DAM spectrum at 10:59:45 UTC (Fig. 6.14). The burst also appears at higher frequencies up to 70 MHz with a few times slower delay. This indicates a reverse burst which is also visible in the spectrum. Three individual bursts can be identified also using the dynamic spectra at 11:00:04, 11:00:24 and 11:01:54 UTC. Especially the last burst shows a very defined short appearance. It also coincides with a burst visible in the NRH image at 151 MHz which could be related and the result of second harmonic radiation.

An overview of the dynamic spectrum as provided through the LSDC is shown in Fig. D.13.

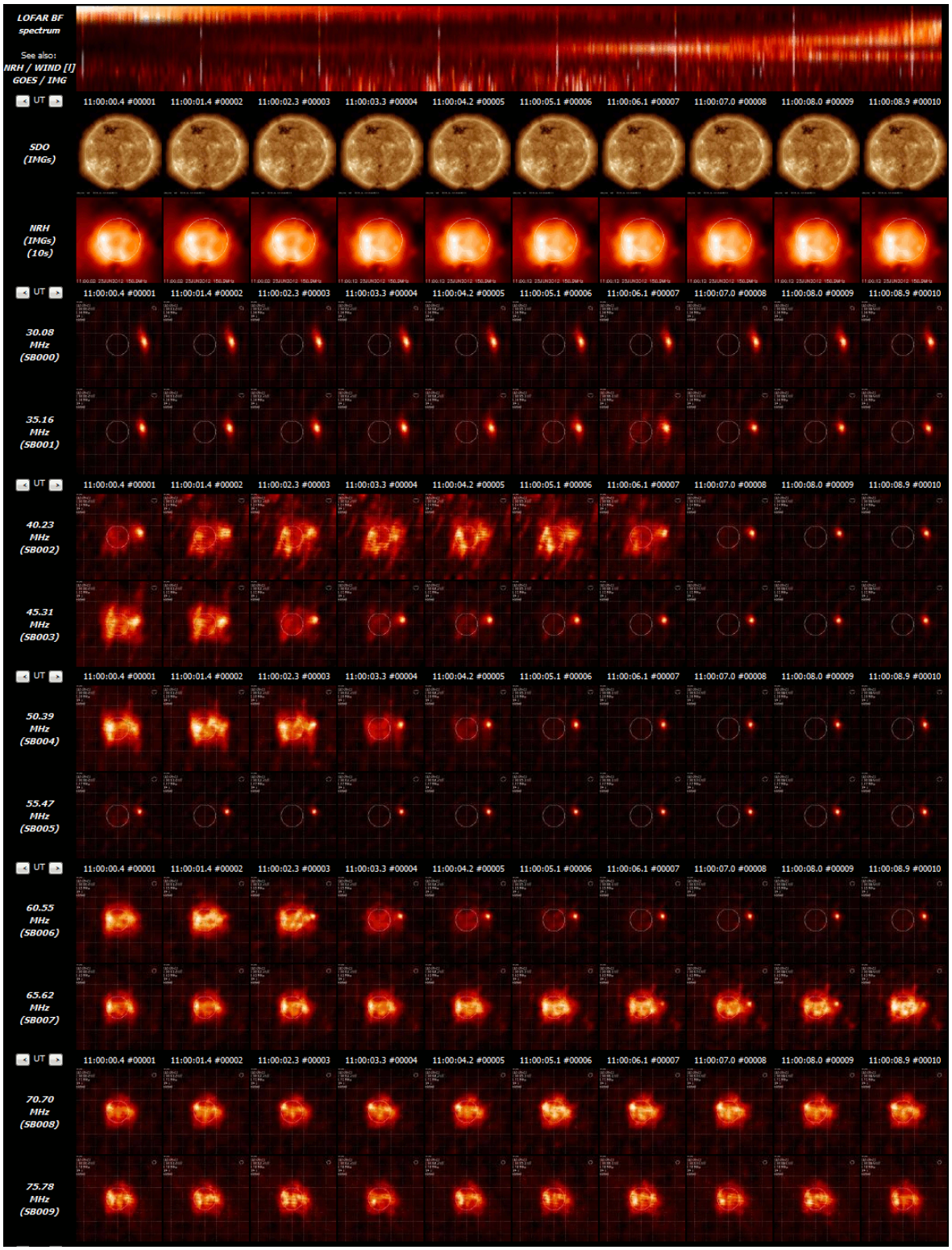

Figure D.1: LOFAR's dynamic imaging spectroscopy of 2012-06-23T11:00:00–11:00:09 UTC as found at `http://lsdc.aip.de/`.

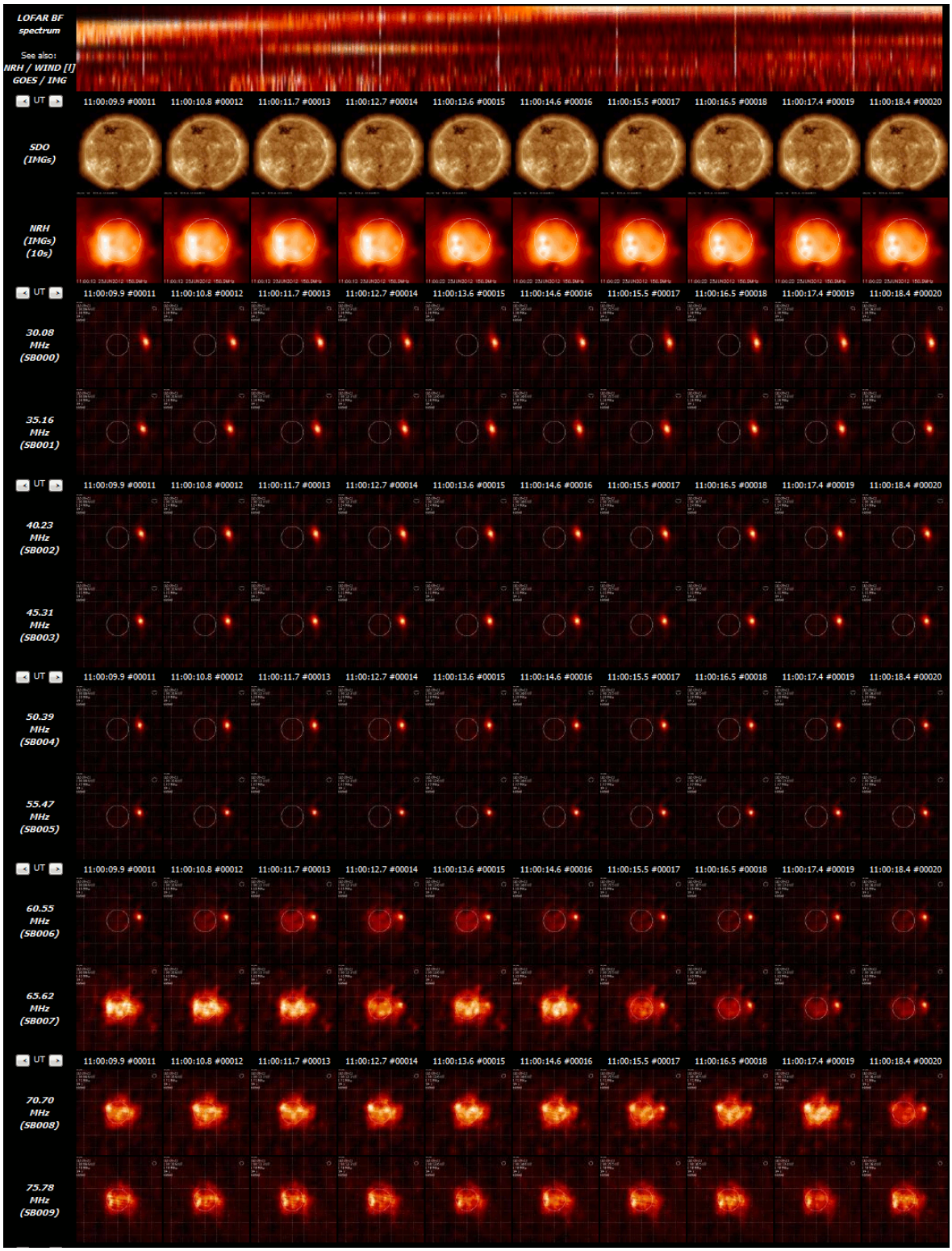

Figure D.2: LOFAR's dynamic imaging spectroscopy of 2012-06-23T11:00:09–11:00:19 UTC as found at `http://lsdc.aip.de/`.

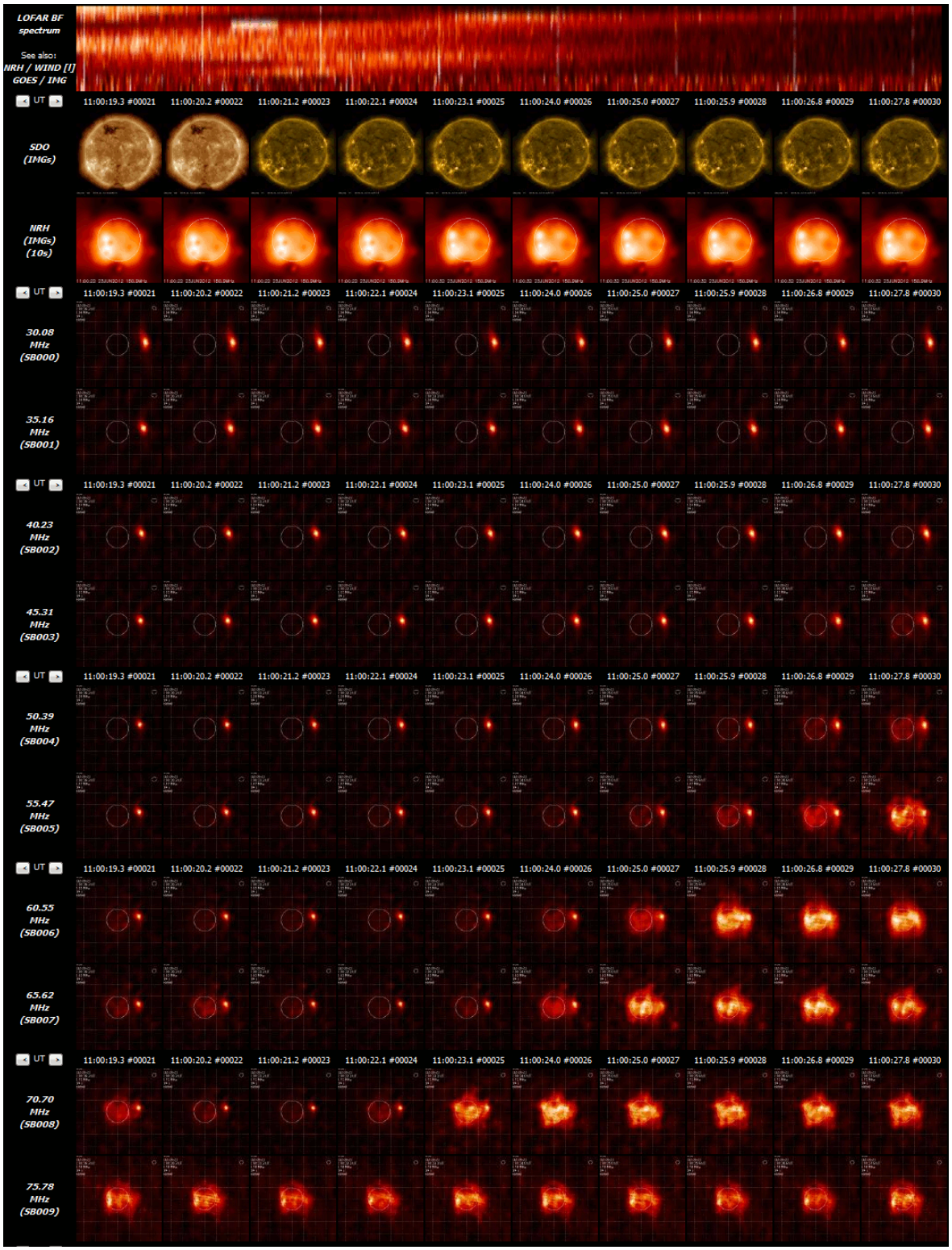

Figure D.3: LOFAR's dynamic imaging spectroscopy of 2012-06-23T11:00:19–11:00:28 UTC as found at `http://lsdc.aip.de/`.

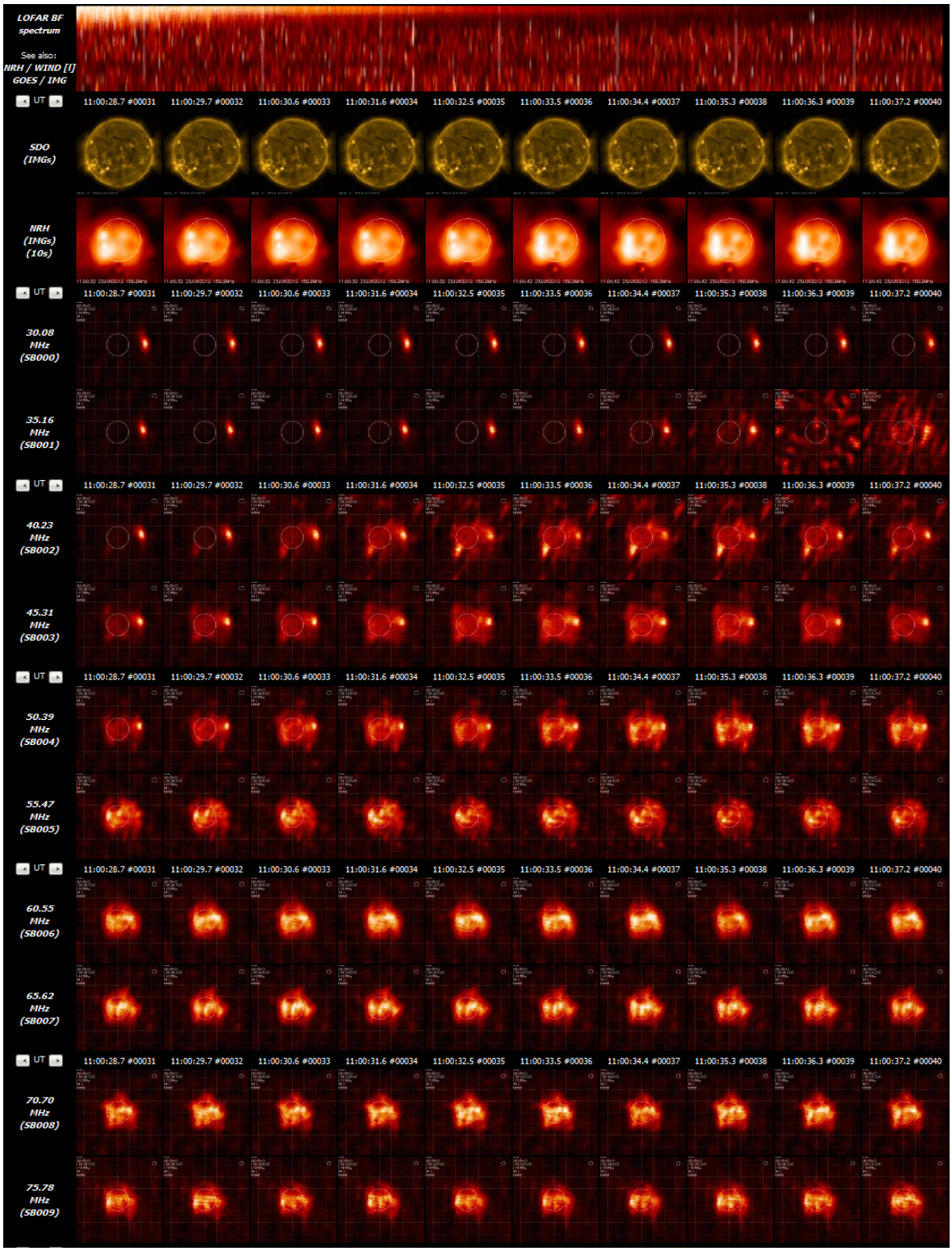

Figure D.4: LOFAR's dynamic imaging spectroscopy of 2012-06-23T11:00:28–11:00:38 UTC as found at `http://lsdc.aip.de/`.

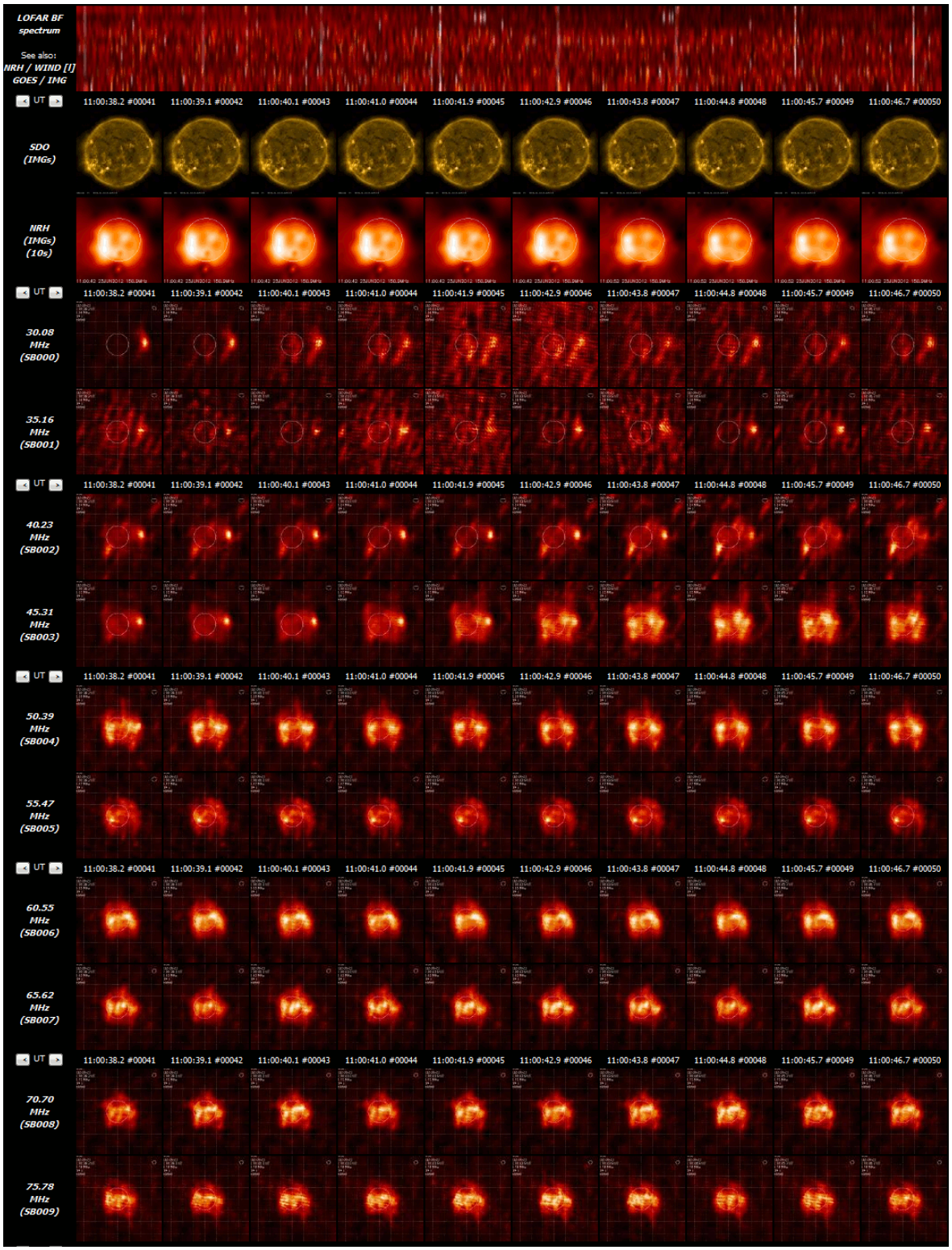

Figure D.5: LOFAR's dynamic imaging spectroscopy of 2012-06-23T11:00:38–11:00:47 UTC as found at `http://lsdc.aip.de/`.

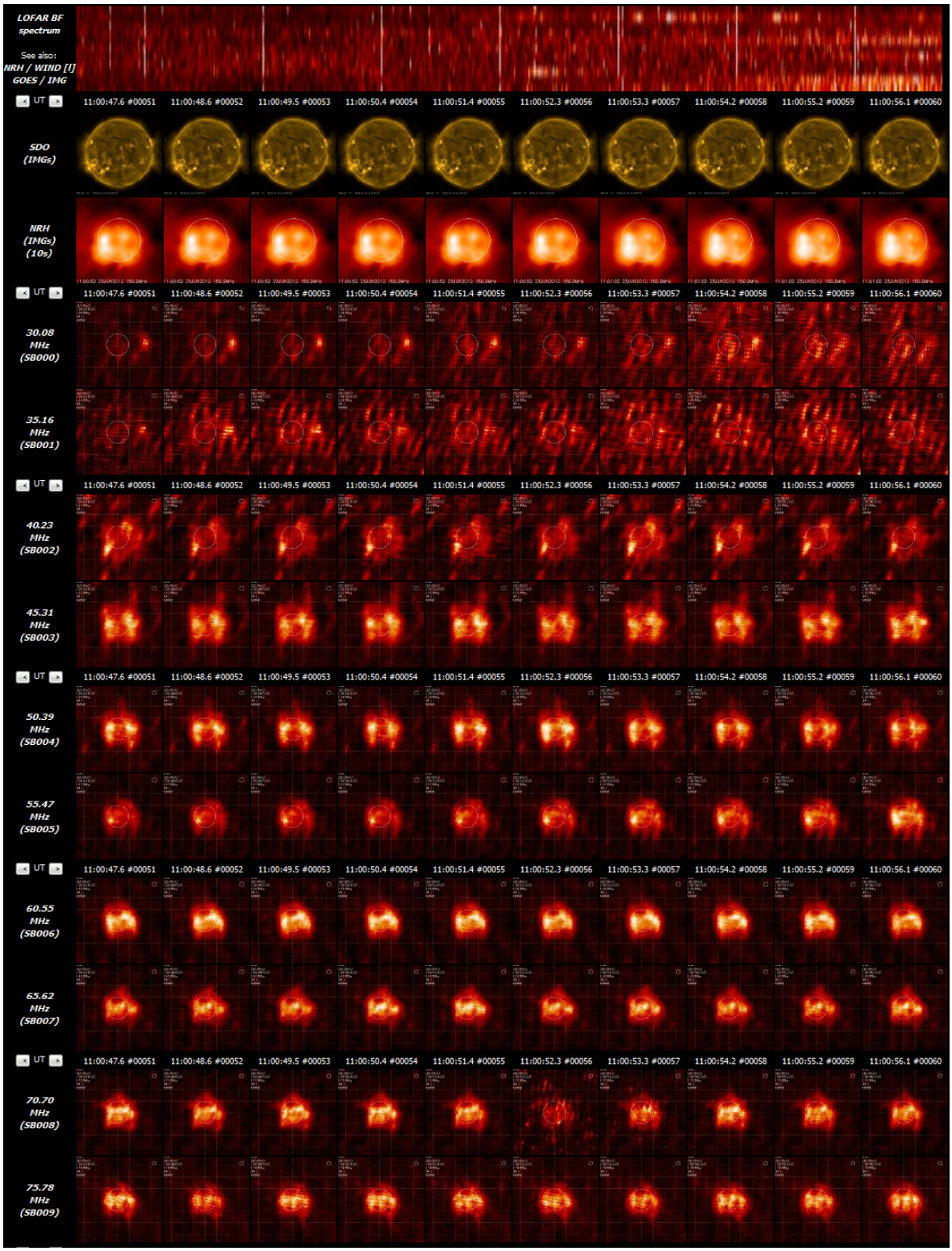

Figure D.6: LOFAR's dynamic imaging spectroscopy of 2012-06-23T11:00:47–11:00:57 UTC as found at `http://lsdc.aip.de/`.

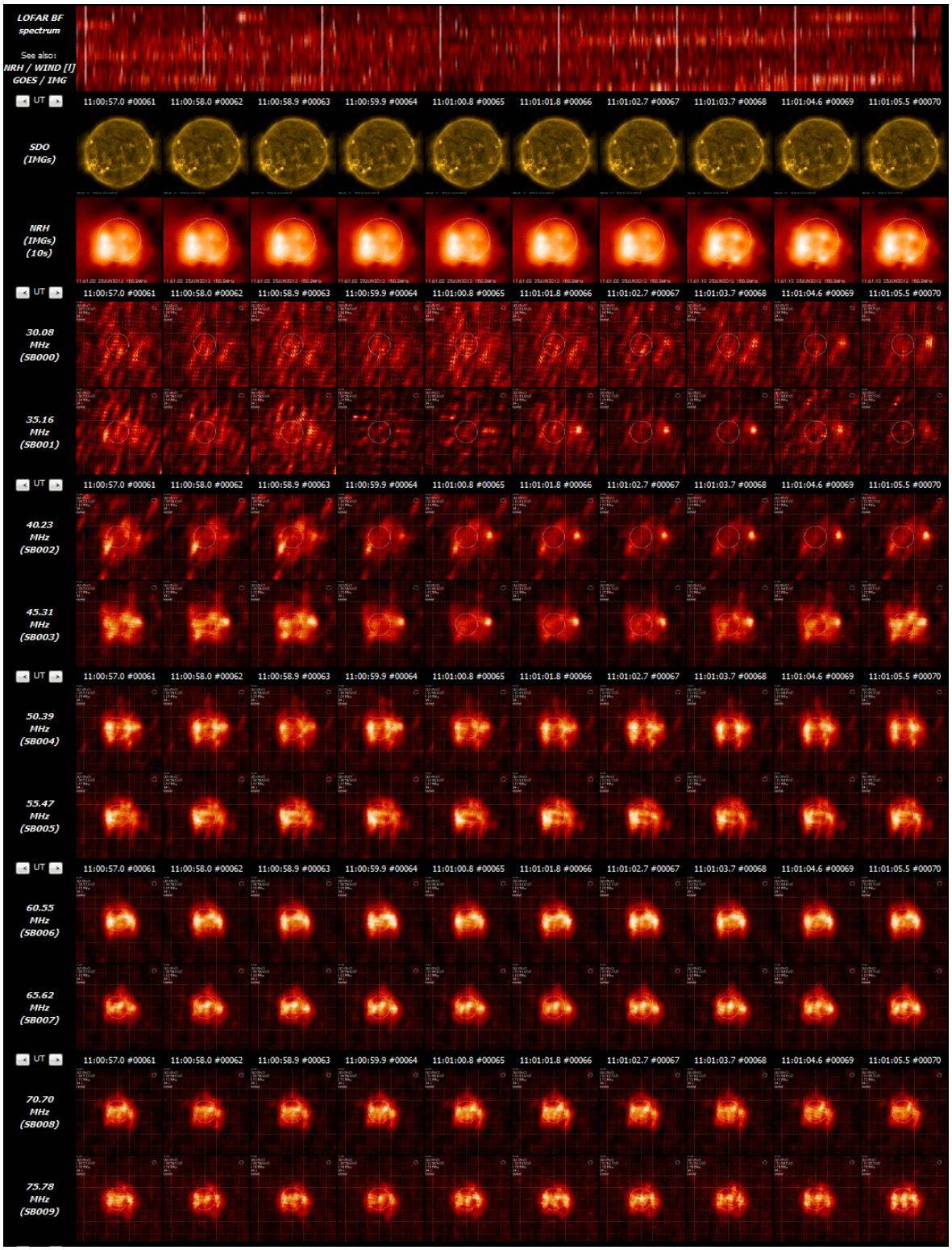

Figure D.7: LOFAR's dynamic imaging spectroscopy of 2012-06-23T11:00:57–11:01:06 UTC as found at `http://lsdc.aip.de/`.

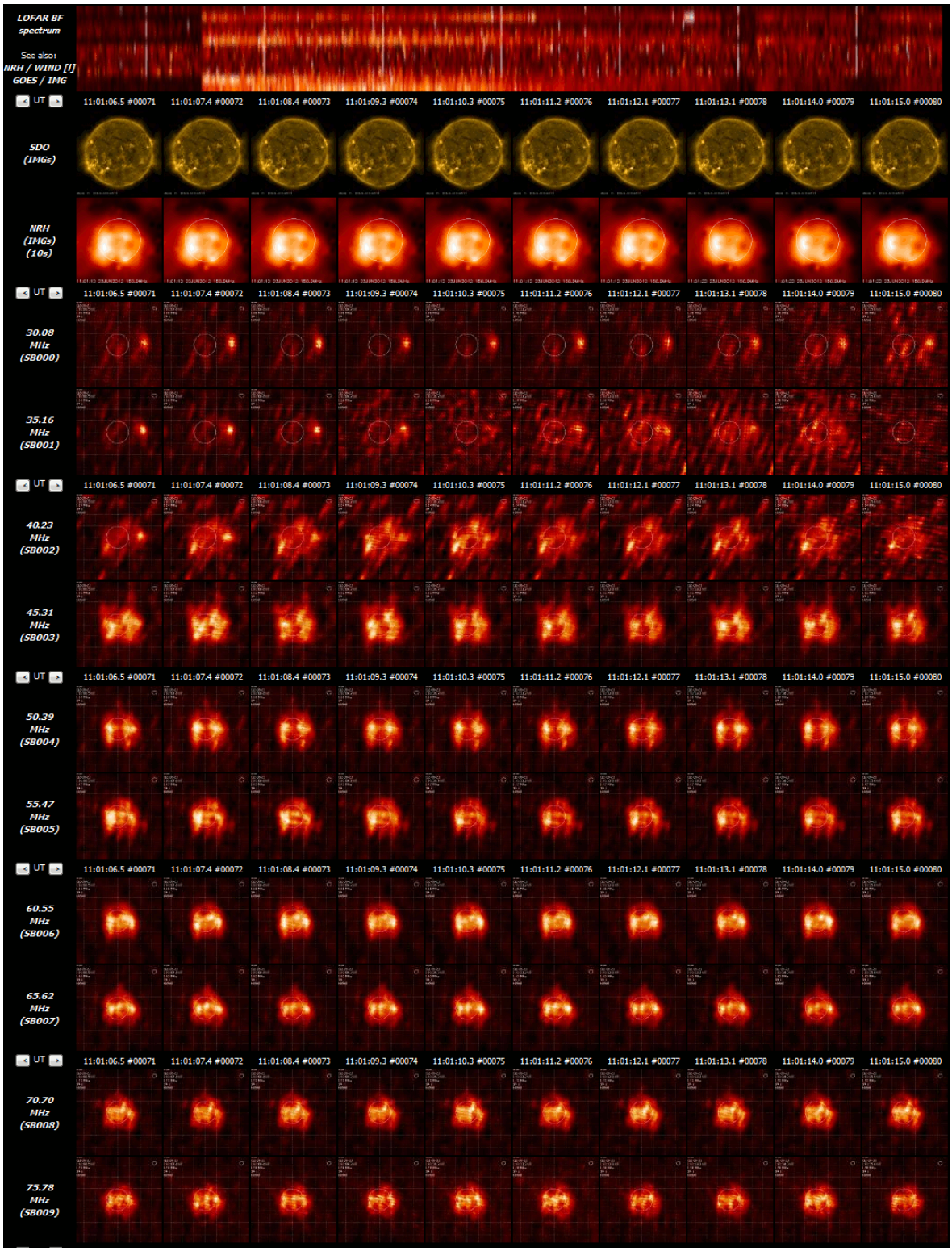

Figure D.8: LOFAR's dynamic imaging spectroscopy of 2012-06-23T11:01:06–11:01:15 UTC as found at `http://lsdc.aip.de/`.

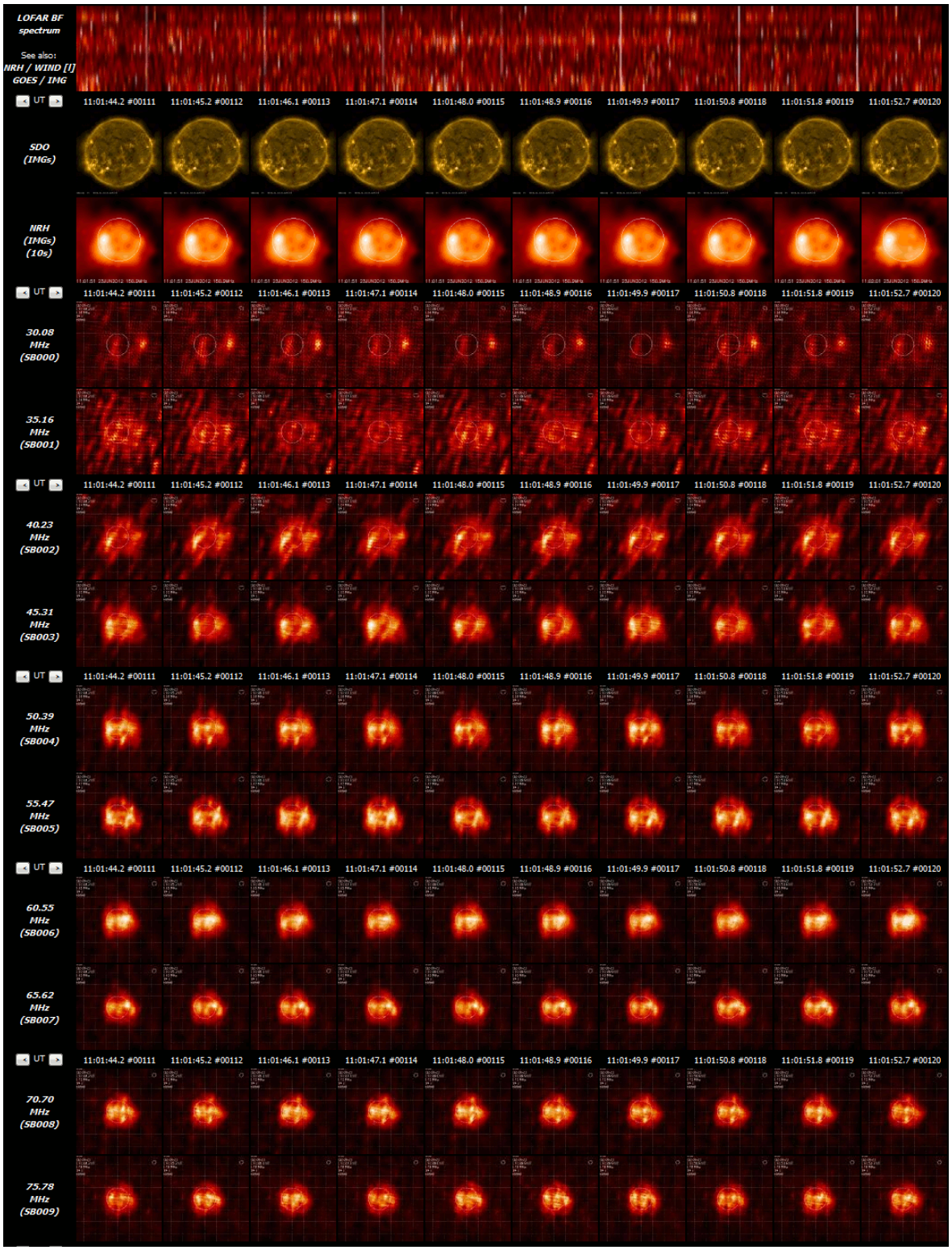

Figure D.9: LOFAR's dynamic imaging spectroscopy of 2012-06-23T11:01:44–11:01:53 UTC as found at `http://lsdc.aip.de/`.

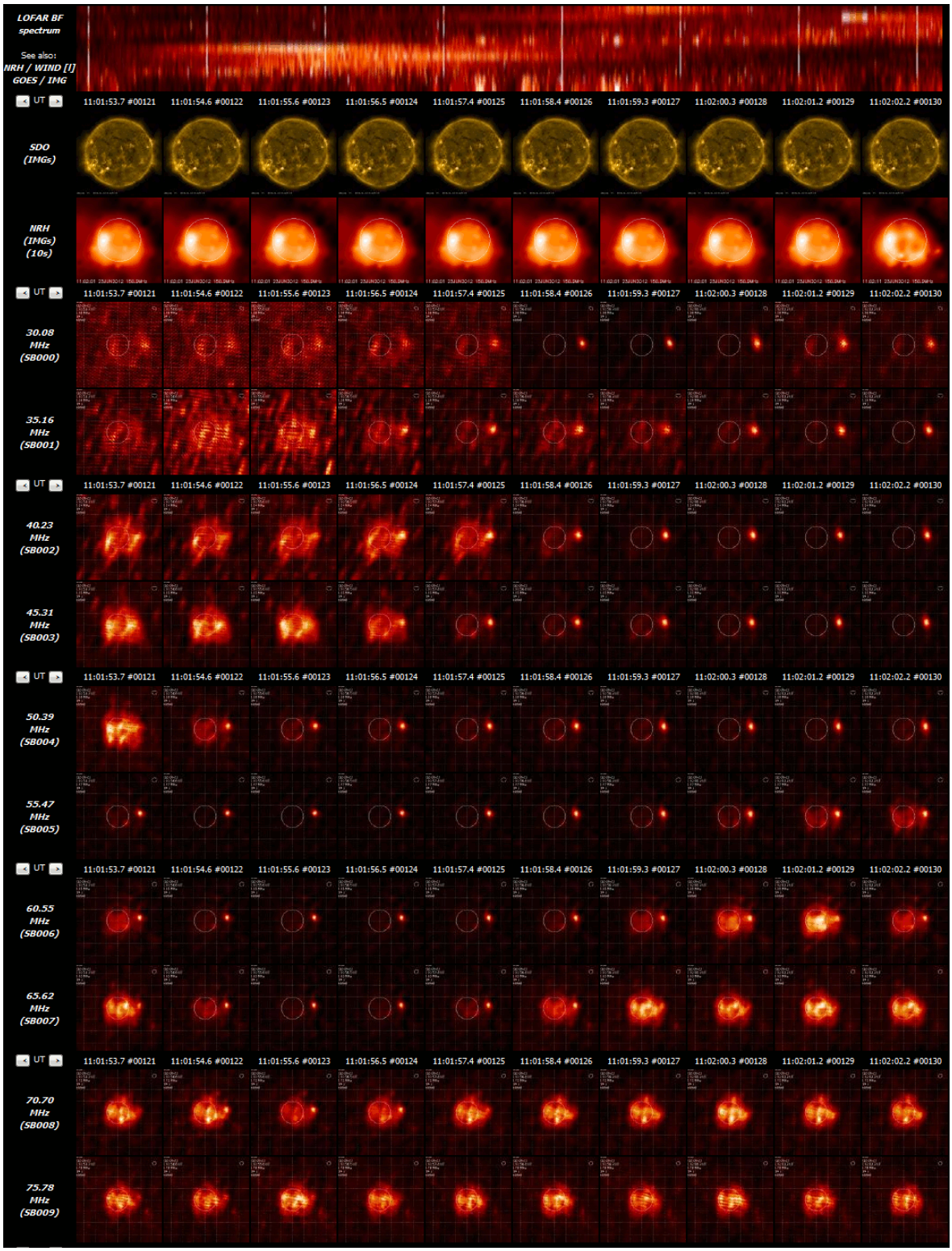

Figure D.10: LOFAR's dynamic imaging spectroscopy of 2012-06-23T11:01:53–11:02:03 UTC as found at `http://lsdc.aip.de/`.

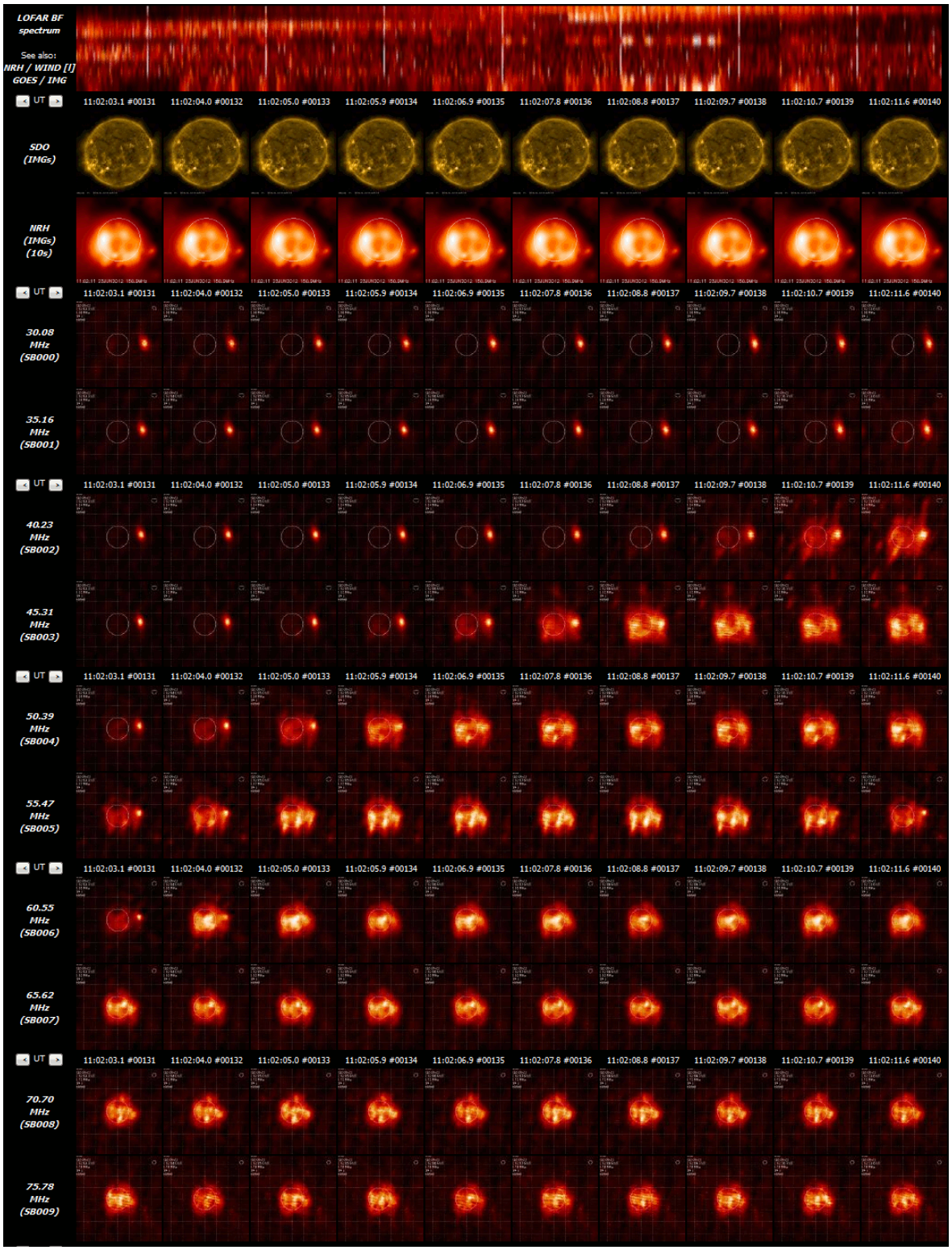

Figure D.11: LOFAR's dynamic imaging spectroscopy of 2012-06-23T11:02:03–11:02:12 UTC as found at `http://lsdc.aip.de/`.

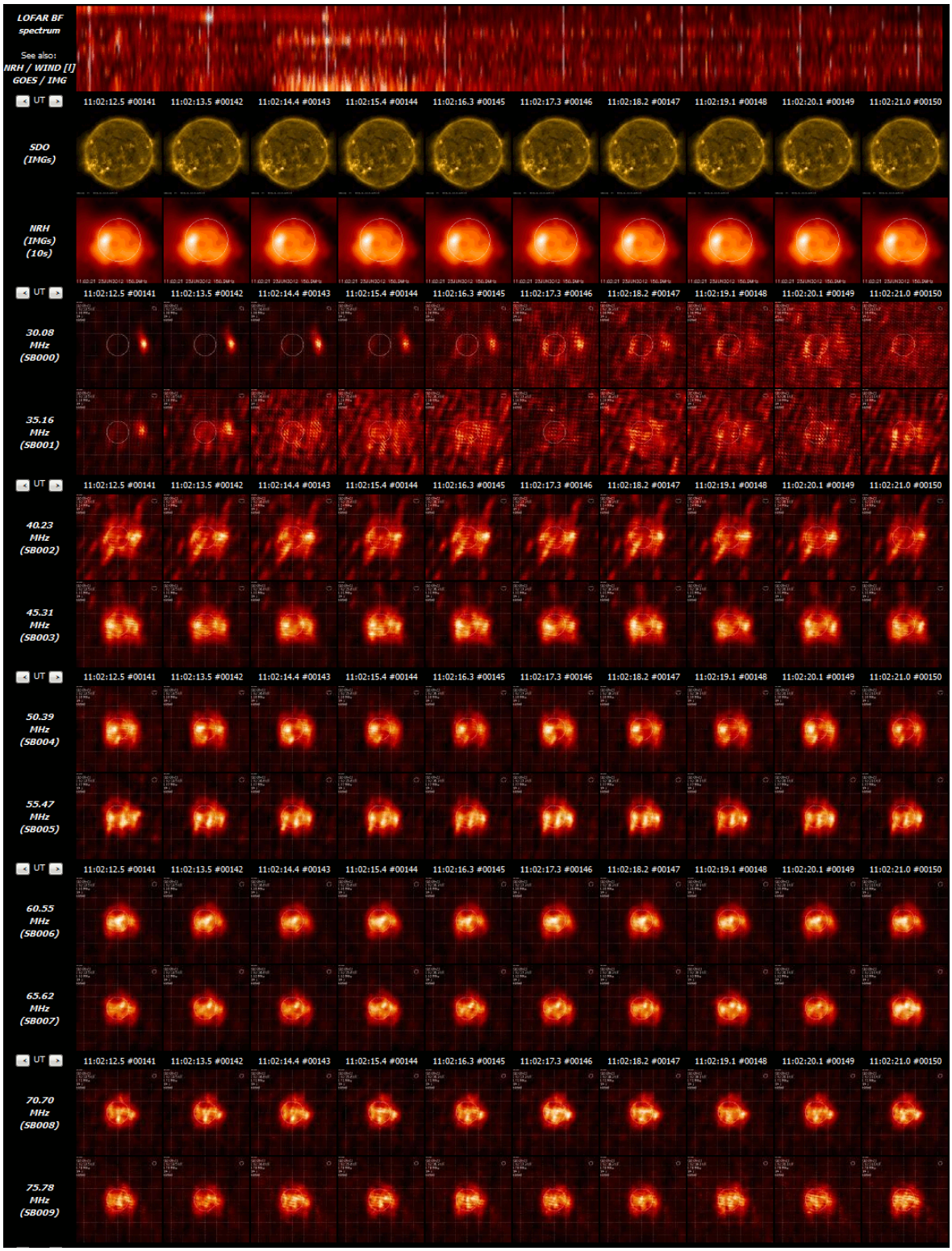

Figure D.12: LOFAR's dynamic imaging spectroscopy of 2012-06-23T11:02:12–11:02:21 UTC as found at `http://lsdc.aip.de/`.

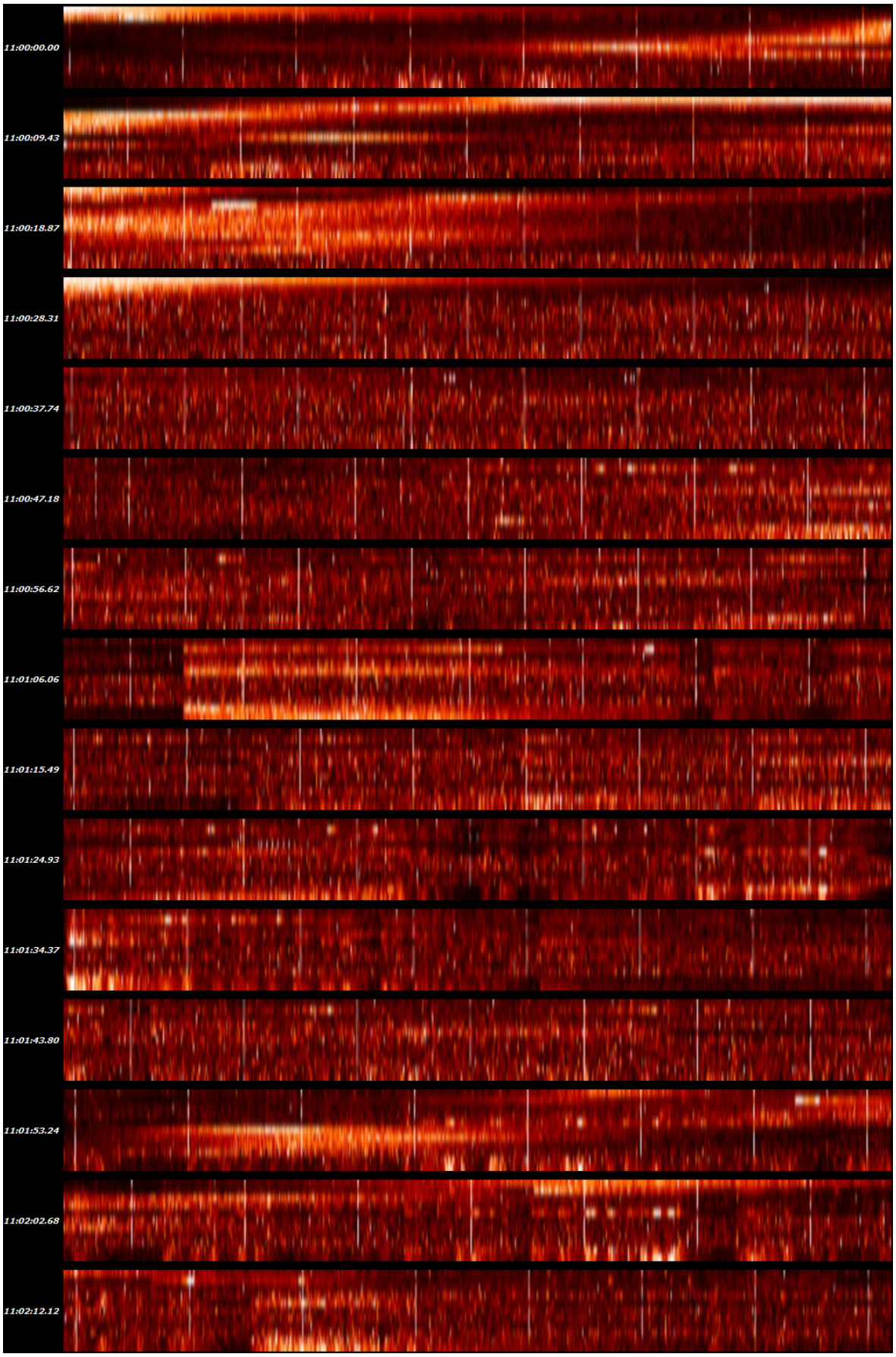

Figure D.13: LOFAR dynamic spectrum of 2012-06-23T11:00:00–11:02:21 UTC as found at `http://lsdc.aip.de/`.

Bibliography

1. Aschwanden, M. J. (2004). *Physics of the Solar Corona. An Introduction*. Praxis Publishing Ltd. Bibcode: 2004psci.book.....A.

2. Baars, J. W. M., Genzel, R., Pauliny-Toth, I. I. K., et al. (1977). "The absolute spectrum of CAS A - an accurate flux density scale and a set of secondary calibrators". In: A&A 61, pp. 99–106. Bibcode: 1977A%26A....61...99B.

3. Babcock, H. W. (1961). "The Topology of the Sun's Magnetic Field and the 22-YEAR Cycle." In: ApJ 133, p. 572. DOI: 10.1086/147060. Bibcode: 1961ApJ...133..572B.

4. Bastian, T. S. (2004). "Low-frequency solar radiophysics with LOFAR and FASR". In: Planet. Space Sci. 52, pp. 1381–1389. DOI: 10.1016/j.pss.2004.09.015. Bibcode: 2004P%26SS...52.1381B.

5. Baumjohann, W. and Treumann, R. A. (1996). *Basic space plasma physics*. London: Imperial College Press, |c1996. Bibcode: 1996bspp.book.....B.

6. Benz, A. O., Monstein, C., and Meyer, H. (2005). "Callisto A New Concept for Solar Radio Spectrometers". In: Sol. Phys. 226, pp. 143–151. DOI: 10.1007/s11207-005-5688-9. eprint: astro-ph/0410437. Bibcode: 2005SoPh..226..143B.

7. Bentely, R. D. and Freeland, S. L. (1998). "SOLARSOFT - an Analysis Environment for Solar Physics". In: *Crossroads for European Solar and Heliospheric Physics. Recent Achievements and Future Mission Possibilities*. Vol. 417. ESA Special Publication, p. 225. Bibcode: 1998ESASP.417..225B.

8. Benz, A. O. (2009). "4.1.1.6 Radio emission of the quiet Sun". In: *Landolt Börnstein*, p. 103. DOI: 10.1007/978-3-540-88055-4_5. Bibcode: 2009LanB...4B..103B.

9. Benz, A. O., ed. (1993). *Plasma astrophysics: Kinetic processes in solar and stellar coronae*. Vol. 184. Astrophysics and Space Science Library. Bibcode: 1993ASSL..184.....B.

10. Boischot, A. (1957). "Caractères d'un type d'émission hertzienne associé à certaines éruptions chromosphériques". In: *Academie des Sciences Paris Comptes Rendus* 244, pp. 1326–1329. Bibcode: 1957CRAS..244.1326B.

11. Boudjada, M. Y., Galopeau, P. H. M., Maksimovic, M., et al. (2014). "Visibility of Type III burst source location as inferred from stereoscopic space observations". In: *Advances in Radio Science* 12, pp. 167–170. Bibcode: 2014AdRS...12..167B.

12. Bougeret, J.-L., Caroubalos, C., Mercier, C., et al. (1970). "Sources of Type III Solar Bursts Observed at 169 MHz with the Nancay Radiohellograph". In: A&A 6, p. 406. Bibcode: 1970A%26A.....6..406B.

13. Bougeret, J.-L., Kaiser, M. L., Kellogg, P. J., et al. (1995). "Waves: The Radio and Plasma Wave Investigation on the Wind Spacecraft". In: Space Sci. Rev. 71, pp. 231–263. DOI: 10.1007/BF00751331. Bibcode: 1995SSRv...71..231B.

14. Breitling, F., Mann, G., and Vocks, C. (2011). "Propagation of Energetic Electrons from the Corona into Interplanetary Space and Type III Radio Emission". In: *Planetary, Solar and Heliospheric Radio Emissions (PRE VII)*, pp. 373–380. arXiv: 1511.03123 [astro-ph.SR]. Bibcode: 2011pre7.conf..373B.

15. Breitling, F., Mann, G., Vocks, C., et al. (2015). "The LOFAR Solar Imaging Pipeline and the LOFAR Solar Data Center". In: *Astronomy and Computing* 13, pp. 99–107. DOI: 10.1016/j.ascom.2015.08.001. arXiv: 1603.05990 [astro-ph.IM]. Bibcode: 2015A%26C....13...99B.

16. Chapman, S. and Zirin, H. (1957). "Notes on the Solar Corona and the Terrestrial Ionosphere". In: *Smithsonian Contributions to Astrophysics* 2, p. 1. Bibcode: 1957SCoA....2....1C.

17. Dulk, G. A. (2000). "Type III Solar Radio Bursts at Long Wavelengths". In: *Washington DC American Geophysical Union Geophysical Monograph Series* 119, p. 115. Bibcode: 2000GMS...119..115D.

18. Dulk, G. A. (1985). "Radio emission from the sun and stars". In: ARA&A 23, pp. 169–224. DOI: 10.1146/annurev.aa.23.090185.001125. Bibcode: 1985ARA%26A..23..169D.

19. Estel, C. (1999). "Ausbreitung energetischer Elektronen von der Sonnenkorona in die innere Heliosphäre". Astrophysikalisches Institut Potsdam (AIP). PhD thesis. Potsdam, Germany: University of Potsdam.

20. Ginzburg, V. L. and Zhelezniakov, V. V. (1958). "On the Possible Mechanisms of Sporadic Solar Radio Emission (Radiation in an Isotropic Plasma)". In: Soviet Ast. 2, p. 653. Bibcode: 1958SvA.....2..653G.

21. Gopalswamy, N., Kundu, M. R., and Szabo, A. (1987). "Propagation of electrons emitting weak type III bursts in coronal streamers". In: Sol. Phys. 108, pp. 333–345. DOI: 10.1007/BF00214168. Bibcode: 1987SoPh..108..333G.

22. Hackenberg, P., Marsch, E., and Mann, G. (2000). "On the origin of the fast solar wind in polar coronal funnels". In: A&A 360, pp. 1139–1147. Bibcode: 2000A%26A...360.1139H.

23. Halain, J.-P., Berghmans, D., Seaton, D. B., et al. (2013). "The SWAP EUV Imaging Telescope. Part II: In-flight Performance and Calibration". In: Sol. Phys. 286, pp. 67–91. DOI: 10.1007/s11207-012-0183-6. arXiv: 1210.3551 [astro-ph.IM]. Bibcode: 2013SoPh..286...67H.

24. Heald, G., Bell, M. R., Horneffer, A., et al. (2011). "LOFAR: Recent Imaging Results and Future Prospects". In: *Journal of Astrophysics and Astronomy* 32, pp. 589–598. DOI: 10.1007/s12036-011-9125-1. arXiv: 1106.3195 [astro-ph.CO]. Bibcode: 2011JApA...32..589H.

25. Heyvaerts, J. (1981). *Recent developments in solar flare models*. Tech. rep. Paris VII Univ., France. Bibcode: 1981soac.reptR....H.

26. Kerdraon, A. and Delouis, J.-M. (1997). "The Nançay Radioheliograph". In: *Coronal Physics from Radio and Space Observations*. Ed. by G. Trottet. Vol. 483. Lecture Notes in Physics, Berlin Springer Verlag, p. 192. DOI: 10.1007/BFb0106458. Bibcode: 1997LNP...483..192K.

27. Klein, K.-L., Krucker, S., Lointier, G., et al. (2008). "Open magnetic flux tubes in the corona and the transport of solar energetic particles". In: A&A 486, pp. 589–596. DOI: 10.1051/0004-6361:20079228. Bibcode: 2008A%26A...486..589K.

28. Klose, S. (1995). "Untersuchung der Eigenschaften von an Stoßwellen in der Sonnenkorona beschleunigten hochenergetischen Elektronen mittels radioastronomischer Methoden". German. PhD thesis. Astrophysikalisches Institut Potsdam (AIP), Germany.

29. Kontogeorgos, A., Tsitsipis, P., Caroubalos, C., et al. (2006). "The improved ARTEMIS IV multichannel solar radio spectrograph of the University of Athens". In: *Experimental Astronomy* 21, pp. 41–55. DOI: 10.1007/s10686-006-9066-x. arXiv: 1009.3628 [astro-ph.IM]. Bibcode: 2006ExA....21...41K.

30. Koutchmy, S. (1994). "Coronal physics from eclipse observations". In: *Advances in Space Research* 14, pp. 29–. DOI: 10.1016/0273-1177(94)90156-2. Bibcode: 1994AdSpR..14...29K.

31. Krueger, A. (1979). *Introduction to solar radio astronomy and radio physics*. Dordrecht: Reidel, 1979. Bibcode: 1979itsr.book.....K.

32. Kundu, M. R., Gergely, T. E., Turner, P. J., et al. (1983). "Direct evidence of type III electron streams propagating in coronal streamers". In: ApJ 269, pp. L67–L71. DOI: 10.1086/184057. Bibcode: 1983ApJ...269L..67K.

33. Kundu, M. R. (1965). *Solar radio astronomy*. New York: Interscience Publication, 1965. Bibcode: 1965sra..book.....K.

34. Lang, K. R. (2010). *3. Atomic and Subatomic Particles: Fig3.6 Internal compression of the Sun*. Ed. by USA: Tufts University Medford MA 02155. URL: https://ase.tufts.edu/cosmos/pictures/stars/Fig3_6Internal_compression_of_the_Sun.jpg (visited on 01/13/2016).

35. Lecacheux, A. (2000). "The Nançay Decameter Array: A Useful Step Towards Giant, New Generation Radio Telescopes for Long Wavelength Radio Astronomy". In: *Washington DC American Geophysical Union Geophysical Monograph Series* 119, p. 321. Bibcode: 2000GMS...119..321L.

36. Leighton, R. B. (1964). "Transport of Magnetic Fields on the Sun." In: ApJ 140, p. 1547. DOI: 10.1086/148058. Bibcode: 1964ApJ...140.1547L.

37. Leighton, R. B. (1969). "A Magneto-Kinematic Model of the Solar Cycle". In: ApJ 156, p. 1. DOI: 10.1086/149943. Bibcode: 1969ApJ...156....1L.

38. Lemen, J. R., Title, A. M., Akin, D. J., et al. (2012). "The Atmospheric Imaging Assembly (AIA) on the Solar Dynamics Observatory (SDO)". In: Sol. Phys. 275, pp. 17–40. DOI: 10.1007/s11207-011-9776-8. Bibcode: 2012SoPh..275...17L.

39. Mamajek, E. E., Prsa, A., Torres, G., et al. (2015). "IAU 2015 Resolution B3 on Recommended Nominal Conversion Constants for Selected Solar and Planetary Properties". In: *ArXiv e-prints*. arXiv: 1510.07674 [astro-ph.SR]. Bibcode: http://esoads.eso.org/abs/2015arXiv151007674M.

40. Mann, G., Breitling, F., Vocks, C., et al. (n.d.). "Tracking of an electron beam through the solar corona with LOFAR". Submitted to A&A.

41. Mann, G. and Klassen, A. (2002). "Shock accelerated electron beams in the solar corona". In: *Solar Variability: From Core to Outer Frontiers*. Ed. by A. Wilson. Vol. 506. ESA Special Publication, pp. 245–248. Bibcode: 2002ESASP.506..245M.

42. Mann, G., Vocks, C., and Breitling, F. (2011). "Solar Observations with LOFAR". In: *Planetary, Solar and Heliospheric Radio Emissions (PRE VII)*, pp. 507–512. Bibcode: 2011pre7.conf..507M.

43. Mann, G., Aurass, H., Voigt, W., et al. (1992). "Preliminary observations of solar type 2 bursts with the new radiospectrograph in Tremsdorf (Germany)". In: *Coronal Streamers, Coronal Loops, and Coronal and Solar Wind Composition*. Ed. by C. Mattok. Vol. 348. ESA Special Publication, pp. 129–132. Bibcode: 1992ESASP.348..129M.

44. Mann, G., Jansen, F., MacDowall, R. J., et al. (1999). "A heliospheric density model and type III radio bursts". In: A&A 348, pp. 614–620. Bibcode: 1999A%26A...348..614M.

45. Mann, G. (2010). "2.2 Solar radio telescopes". In: *Landolt Börnstein*, p. 216. DOI: 10.1007/978-3-540-70607-6_10. Bibcode: 2010LanB...4A..216M.

46. McMullin, J. P., Waters, B., Schiebel, D., et al. (2007). "CASA Architecture and Applications". In: *Astronomical Data Analysis Software and Systems XVI*. Ed. by R. A. Shaw, F. Hill, and D. J. Bell. Vol. 376. Astronomical Society of the Pacific Conference Series, p. 127. Bibcode: 2007ASPC..376..127M.

47. Mel'nik, V. N. and Kontar, E. P. (1999). "The spread of the hot electron cloud in the solar corona". In: New Astronomy 4, pp. 41–44. DOI: 10.1016/S1384-1076(98)00044-X. Bibcode: 1999NewA....4...41M.

48. Melrose, D. B. (2009). "Coherent emission". In: *Universal Heliophysical Processes*. Ed. by N. Gopalswamy and D. F. Webb. Vol. 257. IAU Symposium, pp. 305–315. DOI: 10.1017/S1743921309029470. Bibcode: 2009IAUS..257..305M.

49. Melrose, D. B. (1985). "Plasma emission mechanisms". In: *Solar Radiophysics: Studies of Emission from the Sun at Metre Wavelengths*. Ed. by D. J. McLean and N. R. Labrum. Cambridge and New York, Cambridge University Press, pp. 177–210. Bibcode: 1985srph.book..177M.

50. Miteva, R. S. (2007). "Electron acceleration at localized wave structures in the solar corona". PhD thesis. Astrophysical Institute Potsdam, Germany. Bibcode: 2007PhDT.....40M.

51. Morosan, D. E., Zucca, P., Bloomfield, D. S., et al. (2016). "Conditions for electron-cyclotron maser emission in the solar corona". In: A&A 589, L8, p. L8. DOI: 10.1051/0004-6361/201628392. arXiv: 1604.04788 [astro-ph.SR]. Bibcode: 2016A%26A...589L...8M.

52. Nelson, G. J., Sheridan, K. V., and Suzuki, S. (1985). "Measurements of solar flux density and polarization". In: *Solar Radiophysics: Studies of Emission from the Sun at Metre Wavelengths*. Ed. by D. J. McLean and N. R. Labrum. Cambridge and New York, Cambridge University Press, pp. 113–154. Bibcode: 1985srph.book..113N.

53. Newkirk Jr., G. (1961). "The Solar Corona in Active Regions and the Thermal Origin of the Slowly Varying Component of Solar Radio Radiation." In: ApJ 133, p. 983. DOI: 10.1086/147104. Bibcode: 1961ApJ...133..983N.

54. Offringa, A. R., de Bruyn, A. G., Zaroubi, S., et al. (2013). "The LOFAR radio environment". In: A&A 549, A11, A11. DOI: 10.1051/0004-6361/201220293. arXiv: 1210.0393 [astro-ph.IM]. Bibcode: 2013A%26A...549A..11O.

55. Parker, E. N. (1958). "Dynamics of the Interplanetary Gas and Magnetic Fields." In: ApJ 128, p. 664. DOI: 10.1086/146579. Bibcode: 1958ApJ...128..664P.

56. Priest, E. R. (1982). *Solar magneto-hydrodynamics*. Dordrecht, Holland ; Boston : D. Reidel Pub. Co. ; Hingham, Bibcode: 1982soma.book.....P.

57. Reid, H. A. S., Vilmer, N., and Kontar, E. P. (2011). "Characteristics of the flare acceleration region derived from simultaneous hard X-ray and radio observations". In: A&A 529, A66, A66. DOI: 10.1051/0004-6361/201016181. arXiv: 1102.2342 [astro-ph.SR]. Bibcode: 2011A%26A...529A..66R.

58. Reid, H. A. S. and Ratcliffe, H. (2014). "A review of solar type III radio bursts". In: *Research in Astronomy and Astrophysics* 14, pp. 773–804. DOI: 10.1088/1674-4527/14/7/003. arXiv: 1404.6117 [astro-ph.SR]. Bibcode: 2014RAA....14..773R.

59. Saint-Hilaire, P., Vilmer, N., and Kerdraon, A. (2013). "A Decade of Solar Type III Radio Bursts Observed by the Nançay Radioheliograph 1998-2008". In: ApJ 762, 60, p. 60. DOI: 10.1088/0004-637X/762/1/60. arXiv: 1211.3474 [astro-ph.SR]. Bibcode: 2013ApJ...762...60S.

60. Schrijver, C. J. and Title, A. M. (2001). "On the Formation of Polar Spots in Sun-like Stars". In: ApJ 551, pp. 1099–1106. DOI: 10.1086/320237. Bibcode: 2001ApJ...551.1099S.

61. Schrijver, C. J. and De Rosa, M. L. (2003). "Photospheric and heliospheric magnetic fields". In: Sol. Phys. 212, pp. 165–200. DOI: 10.1023/A:1022908504100. Bibcode: 2003SoPh..212..165S.

62. Schatten, K. H., Wilcox, J. M., and Ness, N. F. (1969). "A model of interplanetary and coronal magnetic fields". In: Sol. Phys. 6, pp. 442–455. DOI: 10.1007/BF00146478. Bibcode: 1969SoPh....6..442S.

63. Schrijver, C. J. (2001). "Simulations of the Photospheric Magnetic Activity and Outer Atmospheric Radiative Losses of Cool Stars Based on Characteristics of the Solar Magnetic Field". In: ApJ 547, pp. 475–490. DOI: 10.1086/318333. Bibcode: 2001ApJ...547..475S.

64. Schwenn, R. (1990). "Large-Scale Structure of the Interplanetary Medium". In: *Physics of the Inner Heliosphere I*. Ed. by R. Schwenn and E. Marsch. Berlin, Germany: Springer-Verlag, p. 99. Bibcode: 1990pihl.book...99S.

65. Stappers, B. W., Hessels, J. W. T., Alexov, A., et al. (2011). "Observing pulsars and fast transients with LOFAR". In: A&A 530, A80, A80. DOI: 10.1051/0004-6361/201116681. arXiv: 1104.1577 [astro-ph.IM]. Bibcode: 2011A%26A...530A..80S.

66. Sturrock, P. A. (1964). "Type III Solar Radio Bursts". In: *NASA Special Publication* 50, p. 357. Bibcode: 1964NASSP..50..357S.

67. Svestka, Z. (1981). "Flare observations". In: *Solar Flare Magnetohydrodynamics*. Ed. by E. R. Priest. New York, Gordon and Breach Science Publishers, pp. 47–137. Bibcode: 1981sfmh.book...47S.

68. Tasse, C., van der Tol, S., van Zwieten, J., et al. (2013). "Applying full polarization A-Projection to very wide field of view instruments: An imager for LOFAR". In: A&A 553, A105, A105. DOI: 10.1051/0004-6361/201220882. arXiv: 1212.6178 [astro-ph.IM]. Bibcode: 2013A%26A...553A.105T.

69. The HDF Group (1997–2014). *Hierarchical Data Format, version 5*. http://www.hdfgroup.org/HDF5/.

70. Thompson, J. R. and Cantner, K. (2012). *Here comes the solar maximum: What we know - and don't know - about solar storms and their hazards*. Ed. by American Geosciences Institute. URL: http://www.earthmagazine.org/article/here-comes-solar-maximum-what-we-know-and-dont-know-about-solar-storms-and-their-hazards (visited on 01/11/2016).

71. Treumann, R. A. and Baumjohann, W. (1997). *Advanced space plasma physics*. London: Imperial College Press, |c1997. Bibcode: 1997aspp.book.....T.

72. van Haarlem, M. P., Wise, M. W., Gunst, A. W., et al. (2013). "LOFAR: The LOw-Frequency ARray". In: A&A 556, A2, A2. DOI: 10.1051/0004-6361/201220873. arXiv: 1305.3550 [astro-ph.IM]. Bibcode: 2013A%26A...556A...2V.

73. Vocks, C. and Mann, G. (2003). "Generation of Suprathermal Electrons by Resonant Wave-Particle Interaction in the Solar Corona and Wind". In: ApJ 593, pp. 1134–1145. DOI: 10.1086/376682. Bibcode: 2003ApJ...593.1134V.

74. Vocks, C. and Mann, G. (2004). "Electron cyclotron maser emission from solar coronal funnels?" In: A&A 419, pp. 763–770. DOI: 10.1051/0004-6361:20035911. Bibcode: 2004A%26A...419..763V.

75. Vocks, C., Mann, G., and Breitling, F. (2016). "Self-calibration strategy for a LOFAR solar radio burst observation". In: *Astronomische Nachrichten* 337, pp. 1099–1104. DOI: 10.1002/asna.201612443.

76. Wachter, R., Schou, J., Rabello-Soares, M. C., et al. (2012). "Image Quality of the Helioseismic and Magnetic Imager (HMI) Onboard the Solar Dynamics Observatory (SDO)". In: Sol. Phys. 275, pp. 261–284. DOI: 10.1007/s11207-011-9709-6. Bibcode: 2012SoPh..275..261W.

77. Wang, Y.-M. and Sheeley Jr., N. R. (1992). "On potential field models of the solar corona". In: ApJ 392, pp. 310–319. DOI: 10.1086/171430. Bibcode: 1992ApJ...392..310W.

78. Warmuth, A. and Mann, G. (2005a). "A model of the Alfvén speed in the solar corona". In: A&A 435, pp. 1123–1135. DOI: 10.1051/0004-6361:20042169. Bibcode: 2005A%26A...435.1123W.

79. Warmuth, A. and Mann, G. (2005b). "The Application of Radio Diagnostics to the Study of the Solar Drivers of Space Weather". In: *Lecture Notes in Physics, Berlin Springer Verlag*. Ed. by K. Scherer, H. Fichtner, B. Heber, et al. Vol. 656. Lecture Notes in Physics, Berlin Springer Verlag, p. 49. DOI: 10.1007/978-3-540-31534-6_3. Bibcode: 2005LNP...656...49W.

80. Warmuth, A. and Mann, G. (2016). "Constraints on energy release in solar flares from RHESSI and GOES X-ray observations. II. Energetics and energy partition". In: A&A 588, A116, A116. DOI: 10.1051/0004-6361/201527475. Bibcode: 2016A%26A...588A.116W.

81. Weber, E. J. (1970). "Unique Solutions of Solar Wind Models with Thermal Conductivity". In: Sol. Phys. 14, pp. 480–488. DOI: 10.1007/BF00221332. Bibcode: 1970SoPh...14..480W.

82. Wild, J. P. and McCready, L. L. (1950). "Observations of the Spectrum of High-Intensity Solar Radiation at Metre Wavelengths. I. The Apparatus and Spectral Types of Solar Burst Observed". In: *Australian Journal of Scientific Research A Physical Sciences* 3, p. 387. Bibcode: 1950AuSRA...3..387W.

83. Wild, J. P., Sheridan, K. V., and Trent, G. H. (1959). "The transverse motions of the sources of solar radio bursts". In: *URSI Symp. 1: Paris Symposium on Radio Astronomy*. Ed. by R. N. Bracewell. Vol. 9. IAU Symposium, p. 176. Bibcode: 1959IAUS....9..176W.

84. Wild, J. P. (1970). "Some investigations of the solar corona: the first two years of observation with the Culgoora radioheliograph". In: *Proceedings of the Astronomical Society of Australia* 1, p. 365. Bibcode: 1970PASAu...1..365W.

85. Wolfram Research, Inc. (2010). *Mathematica*. Version 8.0. Wolfram Research, Inc.

86. Wu, C. S. and Lee, L. C. (1979). “A theory of the terrestrial kilometric radiation”. In: ApJ 230, pp. 621–626. DOI: 10.1086/157120. Bibcode: 1979ApJ...230..621W.

87. Zombeck, M. V. (1990). *Handbook of space astronomy and astrophysics*. Bibcode: 1990hsaa.book.....Z.

Acknowledgment

I would like to thank everybody who has supported this work,

first of all my colleagues at the Leibniz-Institut für Astrophysik Potsdam, mostly from the solar radio physics group, for a friendly and supportive working atmosphere, especially

- my advisor apl. Prof. Dr. Gottfried Mann for the scientific guidance of and interest in this work, valuable discussions, ideas and advice and for providing a friendly, supportive and productive working environment,
- the directors Prof. Dr. Matthias Steinmetz and Prof. Dr. Klaus Strassmeier for the opportunity to work on this topic by providing excellent working conditions and the financial support,
- Dr. habil. Christian Vocks for valuable discussions especially regarding solar wind models and differential equations, for teaching Mathematica to solve a differential equation and for carefully reading this thesis,
- Dr. Hakan Önel for many solutions regarding Mathematica issues,
- Dr. Alexander Warmuth for sharing his experience with the Solarsoft packages and valuable comments regarding this work,
- Dr. habil. Henry Auraß for introducing me to the potential-field source-surface method,
- Dr. Harry Enke, Dr. Arman Khalatyan, Dr. Jochen Klar and Steven White from the e-Science group for providing the data storage, computer cluster and web server for the LOFAR Solar Data Center,
- Doris Lehmann for support in general work related issues.

I would also like to thank

- the LOFAR team and software developers in particular Dr. James Anderson, Dr. Ger De Bruyn, Dr. Ger van Diepen, M.Sc. Sven Duscha, Dr. Richard Fallows, Dr. Jean-Mathias Grießmeier, Teun Grit, Dr. George Heald, Menno Norden, Dr. Emanuela Orru, Dr. Roberto Pizzo, Arno Schoenmakers, Dr. Cyril Tasse, Nicolas Vilchey, Dr. Reinoud van Weeren, Dr. Michael Wise, Dr. Olaf Wucknitz, Joris van Zwieten
- as well as the CASA developers

for a good collaboration and their support of the Solar Imaging Pipeline through the development of essential components and tools and helpful communication.

And I thank

- Dr. Laurent Denis and Coffre Andrée from the Naçay Decametric Array,
- Dr. Alexander Hillaris, Dr. Costas Bouratzis from the ARTEMIS-IV group in Athens,
- Prof. Dr. Valentin Melnik from URAN-2 of Ukraine,

for their courtesy in providing dynamic radio spectra of their spectrometers,

- Dr. Mark DeRosa, the developer of the PFSS package of Solarsoft from Lockheed Martin Solar and Astrophysics Laboratory, for his help in extending the magnetic field line calculations to the region of LOFAR observations and helpful discussions,
- My family and friends for moral support.

LOFAR, designed and constructed by ASTRON, has facilities in several countries that are owned by various parties (each with their own funding sources) and are collectively operated by the International LOFAR Telescope (ILT) foundation under a joint scientific policy.

This work was supported through the grant of the German Federal Ministry of Education and Research (BMBF in the framework of the Verbundforschung, D-LOFAR 05A11BAA).